Emulation of Neural Dynamics in Neuromorphic Circuits Based on Memristive Devices

Dissertation

zur Erlangung des akademischen Grades

Doktor der Ingenieurwissenschaften

(Dr.-Ing.)

der Technischen Fakultät

der Christian-Albrechts-Universität zu Kiel

vorgelegt von

M. Sc. Marina Ignatov

aus Alma-Ata in Kasachstan

Kiel

2017

Erster Gutachter:	Prof. Dr. Hermann Kohlstedt
Zweiter Gutachter:	Prof. Dr. Franz Faupel
Datum der mündlichen Prüfung:	29.03.2018

Erklärung

Ich, Marina Ignatov, erkläre an Eides statt, dass die Dissertation zum Thema

Emulation of Neural Dynamics in Neuromorphic Circuits Based on Memristive Devices

abgesehen von der Beratung durch meinen Betreuer nach Inhalt und Form meine eigene Arbeit ist. Außerdem versichere ich hiermit, dass ich die vorliegende Arbeit bisher weder ganz noch zum Teil an einer anderen Stelle im Rahmen eines Prüfungsverfahrens vorgelegt, veröffentlicht oder zur Veröffentlichung eingereicht habe. Weiterhin versichere ich hiermit, dass ich die vorliegende Arbeit unter Einhaltung der Regeln guter wissenschaftlicher Praxis der Deutschen Forschungsgemeinschaft angefertigt habe und alle von anderen Autoren wörtlich übernommenen Stellen wie auch die sich an die Gedankengänge anderer Autoren eng anlehnenden Ausführungen meiner Arbeit besonders gekennzeichnet und die entsprechenden Quellen angegeben sind. Ich versichere außerdem, dass ich keine früheren Promotionsversuche unternommen habe.

Kiel, den

Marina Ignatov

Danksagung

Prof. Hermann Kohlstedt danke ich dafür, dass er seine Aufgabe als Doktorvater und Lehrstuhlleiter hervorragend meistert. Deine Fairness, deine „Offene-Tür-Politik“, dein Humor und deine Klarsicht haben es ermöglicht, eine Atmosphäre am Lehrstuhl zu schaffen, sodass ich mit Spaß forschen und jederzeit auf deine Unterstützung und dein fachliches Wissen zählen konnte.

Dr. Martin Ziegler spreche ich meinen tiefen Dank für die letzten vier Jahre aus, in denen er mir ausgezeichnet zur Seite stand. Deine Gabe, den Punkt zu verstehen und den auf eine inspirierende Weise zu kommunizieren, hat meine Denkweise geprägt. Jederzeit konnte ich zu dir kommen und du hast mir mit viel Engagement weitergeholfen. Du hattest einen großen Einfluss auf den Verlauf der Arbeit. Ich werde unsere gemeinsame Arbeitszeit vermissen.

Mirko Hansen danke ich nicht nur für die Herstellung der memristiven Bauelemente, sondern auch für die zahlreiche Hilfe in fachlichen sowie technischen Problemen. Die Diskussionen mit dir waren sehr hilfreich.

Dr. Adrian Petraru danke ich für die Herstellung der Proben.

Nora Kohlstedt danke ich für das Zeichnen des Flusspferdes.

Meinen Kollegen, die mich in meiner Zeit am Lehrstuhl begleitet haben, möchte ich für die fachlichen Diskussionen und für die vielen schönen Momente danken.

Zu guter Letzt bedanke ich mich von Herzen bei meinen Eltern Ludmilla und Waldemar und meiner Schwester Katharina dafür, dass sie mir in jeder Phase meines Studiums liebevoll zur Seite standen und mich stets unterstützt haben.

Kurzfassung

Zu den beeindruckendsten Eigenschaften des menschlichen Gehirns gehören Wahrnehmung und Bewusstsein. Auch wenn die dafür zugrundeliegenden Mechanismen noch nicht verstanden sind, gilt es als sehr wahrscheinlich, dass zwei Faktoren wichtige Rollen spielen. Zum einem ist dies die Struktur des Netzwerkes, d.h. seine Topologie, und zum anderen die Netzwerkdynamik. Zur technischen Nachbildung und Modellierung dieser Prozesse bieten neuromorphe Schaltungen einen interessanten Ansatz, da sie es erlauben, die Komplexität neuronaler Netzwerke auf energieeffiziente und echtzeitfähige Systeme abzubilden. Hierfür werden analoge elektrische Schaltungen verwendet, die sich möglichst eng an biologischen Netzwerken orientieren. Insbesondere sind hierfür elektronische Komponenten wichtig, die es ermöglichen, die für Lern-und Gedächtnisprozesse wichtigen Mechanismen, die an den Verbindungsstellen zwischen Neuronen in Form von Synapsen auftreten, nachzubilden. In diesem Zusammenhang kann gezeigt werden, dass nano-ionische Mechanismen in memristiven Bauelementen es ermöglichen, synaptische Plastizität auf deskriptiver Ebene innerhalb eines einzelnen Bauelementes zu emulieren. Bei memristiven Bauelementen handelt es sich um passive, nichtflüchtige Bauelemente, deren Widerstandswert von den angelegten elektrischen Potentialen abhängt. In den letzten Jahren konnten wichtige Plastizitätsmechanismen der synaptischen Informationsverarbeitung mittels memristiver Bauelemente nachgebildet werden. Die Bedeutung von memristiven Bauelementen zur Nachbildung dynamischer Prozesse in der Informationsverarbeitung wird weltweit intensiv erforscht und bildet das Thema der vorliegenden Arbeit.

In dieser Arbeit wird eine Brücke geschlagen von zellulären Prozessen, die Informationskodierung und Weiterleitung innerhalb von Neuronenmodellen emulieren, zu Netzwerken, die höhere kognitive Funktionen nachbilden und es ermöglichen, Wahrnehmungsprozesse in elektronische

Schaltungen zu emulieren. Insbesondere wird dafür der Zusammenhang von Dynamik und Plastizität unter topologischen Gesichtspunkten untersucht. Im Einzelnen wird eine elektronische, memristive Schaltung vorgestellt, die die dynamische Informationskodierung eines Neurons in Form von Frequenzkodierung und Frequenzadaption nachbildet. Der Übergang zum Netzwerkverhalten wird über memristive, pulsgekoppelte Oszillatoren erreicht. Es wird gezeigt, dass sich mit einer memristiven Pulskopplung zweier Relaxationsoszillatoren zwei relevante dynamische Aspekte der Biologie auf elektronische Schaltungen übertragen lassen: Gedächtnis und Synchronität. Ferner wird gezeigt, dass der Aufbau pulsgekoppelter memristiver Oszillatornetzwerke die Nachbildung von Wahrnehmungsprozessen erlaubt. Hierfür wird die inhärente Stochastizität des Widerstandsschaltmechanimusses von elektrochemischen, memristiven Bauelementen für ein Plastizitätsmodell verwendet, das die Veränderung der Wahrnehmung unter den Einfluss von Aufmerksamkeit emuliert und den bekanntesten Ansatz zur Lösung des Bindungsproblems innerhalb einer elektronischen Schaltung nachbildet: die Pulskopplung neuronaler Ensembles.

Abstract

The most impressive properties of the human brain are widely acknowledged as being perception and consciousness. While the underlying mechanisms are not yet understood, it is very likely that neural dynamics, in connection with the topology of neural networks, may play a decisive role. Neuromorphic systems offer an interesting approach to emulate and model these processes, as they allow the complexity of neural networks to be mapped onto energy-efficient and real-time capable systems. For this purpose, analogue electrical circuits that are oriented as closely as possible to biological networks are investigated. Electronic devices are particularly important for this purpose, as they make it possible to emulate the mechanisms that are important to the learning and memory processes that occur at the connections of neurons in form of synapses. In this context, it has been shown that nano-ionic mechanisms, in so-called memristive devices, allow the emulation of synaptic plasticity on a descriptive level within a single device. Memristive devices are passive, non-volatile components whose resistance value depends on the applied electrical potentials. In recent years, the important plasticity mechanisms of synaptic information-processing have been emulated using memristive devices. The importance of memristive devices in terms of emulating dynamic processes within novel bio-inspired computing schemes attract worldwide interest and is the subject of this thesis.

In this thesis, a bridge is built between the cellular processes that emulate information coding and transmission within neural models to networks that emulate higher cognitive functions and enable the emulation of perceptual processes in electronic circuits. In particular, the interrelation of dynamics and plasticity in a topology is investigated. More specifically, an electronic memristive circuit that emulates the dynamic information coding that occurs in a neuron in the form of frequency coding and frequency adaptation is presented. The transition to network

behavior is achieved via memristive pulse-coupled oscillators. For this purpose, it is demonstrated that, with the memristive pulse-coupling of two relaxation oscillators, two relevant dynamic aspects of biology can be transferred to electronic circuits, namely memory and synchronization. Furthermore, it is also demonstrated that the construction of pulse-coupled memristive oscillator networks allows for the emulation of perceptual processes. For this purpose, the inherent stochasticity of the resistance-switching mechanism of electrochemical memristive devices is used in a plasticity model that emulates the changes in perception that occur as a result of the influence of attention; in addition, it emulates the best-known approach to solving the binding problem within an electronic circuit, namely the pulse-coupling of neuronal ensembles.

Contents

Publications refered to this Thesis

The majority of the results of this thesis have already been published, which is why the publications are assigned to the sections below. A complete list of the publications to which the author contributed is provided in the scientific vita.

- Sections 3.5.1 and 3.5.2.1:
  Preliminary work took place in the author's master thesis.
  M. Ignatov
  Anwendung von „Metall-Isolator-Übergangs"-Kontakten für memristive Bauelemente,
  Master's thesis, Christian-Albrechts-Universität zu Kiel, Faculty of Engineering, Chair of Nanoelectronics, (2013 October).

- Sections 2.1.4.1, 2.2.1, 3.2, 3.5, 2.1.4.3, and 3.8:
  M. Ignatov, M. Ziegler, M. Hansen, A. Petraru, and H. Kohlstedt,
  A memristive spiking neuron with firing rate coding,
  Frontiers in Neuroscience **9**, 376 (2015 October 20).
  doi: 10.3389/fnins.2015.00376, the use is permitted under CC BY 4.0 license.

- Sections 3.8 and 4.2:
  M. Ignatov, M. Hansen, M. Ziegler, and H. Kohlstedt,
  Synchronization of two memristively coupled van der Pol oscillators,
  Applied Physics Letters **108**(8), 084105 (2016 February 25).
  doi: 10.1063/1.4942832, re-use is permitted by AIP Publishing in this thesis.

- Sections 2.1.4.1, 3.3.1, 4.1.4, 2.1.4.3, 3.8, and 4.3
  M. Ignatov, M. Ziegler, M. Hansen, and H. Kohlstedt,
  Memristive stochastic plasticity enables mimicking of neural synchrony: Memristive circuit emulates an optical illusion,
  Science Advances **3**(10), e1700849 (2017 October 25).
  doi: 10.1126/sciadv.1700849, the use is permitted under CC BY-NC 4.0 license.

Abbreviations

ANN	Artificial Neural Networks
CC	Current Compliance
CMOS	Complementary Metal Oxide Semiconductor
DC	Direct Current
ECM	Electrochemical Metallization Memory
HRS	High Resistance State
LRS	Low Resistance State
LTD	Long-Term Depression
LTP	Long-Term Potentiation
MC	Main Chamber
MIM	Metal-Insulator-Metal
NDR	Negative Differential Resistance
OC	Oxidation Chamber
PLD	Pulsed Laser Deposition
PSP	Postsynaptic Potential
PUT	Programmable Unijunction Transistor
PVD	Physical Vapor Deposition
PVD	Physical Vapor Deposition
RC	Rest Chamber
RRAM	Resistive Random Access Memory
RU	Research Unit
SC	Sputter Chamber
SMU	Source Measurement Unit
STDP	Spike-Timing-Dependent Plasticity
UV	Ultraviolet
VCM	Valence Change Memory
VLSI	Very Large Scale Integration

1 Introduction

The brain is a dynamic and flexible system wherein dynamic processes occur in various manifestations at all levels [1]: starting at the cellular level, in the form of synaptic plasticity [2] to neural dynamics and up to the network level, where ensemble oscillations are associated with dynamic synchronization mechanisms [3]. The neural dynamics in single neurons are responsible for the transmission and coding of information in the form of spike generation and neural activity patterns, including frequency coding and spike-frequency adaptation [4–11]. While, at the cellular level, the mechanisms that lead to plastic coupling strength are largely understood, the complex mutual interaction of local cellular process versus the global network behavior (and vice versa!), is still unknown [3, 12–14]. However, it has been found that cellular plasticity processes are the basis of memory and learning processes in neural system [9, 15]. Thus, the emulation of such dynamical network behavior in dependence on cellular plasticity processes must be possible [16]. This includes local learning rules, such as the Hebbian learning rule, which can be summarized as "neurons that fire together wire together" [15, 17].

At the network level, the dynamic system is divided into specialized subsystems that process the information received from the environment in an efficient manner. For example, visual information is decomposed into individual aspects, such as color, shape, depth, and motion, and is processed by a transient subsystem in each case [3, 16, 18]. This enables a massive parallel processing of information via the use of context-dependent and transient subsystems [3, 16, 19]. For this purpose, the brain always passes through three stages of perception: selective attention, segregation, and integration [16, 20–22]. The mechanism behind the integration of the decomposed aspects of information into a uniform perception is one of the most puzzling questions in neuroscience and is known as the "binding problem" [16, 18, 23–31]. A promising approach to

address this issue is to relate brain oscillation to synchronization mechanisms of even spatial separated neuronal ensembles [16, 18, 23, 24, 32–35]. In this context, pulse-coupled oscillators are suitable for the emulation of neural synchronization, since they take the spike-induced interactions of neurons into account [36–40]. Therefore, numerous theoretical investigations have used pulse-coupled oscillators in their models [41–44].

A considerable number of artificial neural networks (ANNs) in the field of neuromorphic engineering attempt to emulate brain-related neural processes [15,16,45–48]. Based on a mixed-signal, very large scale integration (VLSI) technology [47] and parallel computing schemes, energy-efficient real-time processing systems have been demonstrated [15]. A further facilitate access to neural networks could be achieved through the insertion of memristive devices. Such a device's resistance state changes due to the "reminded" applied voltage (charge flow), and, thus, such a single device is already capable of emulating a synapse's behavior on a descriptive level [15, 49–51]. However, the focus thus far has been on the emulation of plasticity properties [12, 52–65], rather than neural dynamics (upon which the brain's functioning also relies). Mathematical models of the neural dynamics found in self-organized simple networks have been developed [6,66–69], whereas access to electronic self-organized circuits that demonstrate neural dynamics in combination with dynamic synchronization is rarely available [70–72]. Furthermore, rigid static resistors are mostly used for the experimental coupling of such oscillator networks, rather than "synaptic" devices [73]. The synchronization of oscillator dynamics within a complex network has led to a renewed interest in the emulation of neural dynamics [51, 74, 75]. In addition to the synchronization mechanisms, special attention has been paid to network topologies, since they are relevant to the learning mechanism and the functioning of the brain [25, 26, 36, 76, 77].

This thesis intends to investigate the use of memristive devices in a dynamical network. In the first instance, the focus is on the cellular paradigms involved in neural dynamics. More specifically, the characteristics of neural dynamics, in the form of spike generation, information coding, and the transmission of spikes, are realized with the use of electronic

neuromorphic circuits [10]. The transition from a single neuron to the complex network level occurs via the use of pulse-coupled oscillator networks with memristive devices. In addition to the properties of real-time processing, energy efficiency, and parallel computing, the circuit is characterized by dynamic processes, wherein synchronization of neural activity patterns introduces memory states and the association of information for higher brain functionalities [16]. A placement in complex networks is ensured by the fact that singular neural dynamics are linked in a multitude of different states; as a consequence, the network behavior of single dynamics deviates from their independent dynamics [1, 3, 20, 69, 78–81].

This thesis is divided into three sections: The first part provides a basic overview of memristive systems. In the second part, an overview of the important properties of the basic units in a neural system provides an understanding of the spiking neuron models. More specifically, a memristive spiking neuron model with the properties of frequency coding and frequency adaptation is described in Chapter 3. In the third part, memristively coupled oscillator networks are presented: Initial, two memristively pulse-coupled oscillators are shown. Depending on the memristive device used, the transition from the desynchronous to synchronous state occurs in two ways: abruptly or with an intermediate state. Finally, an extension to a dynamic network of memristively pulse-coupled oscillators enables coping with perception processes through the use of a local learning rule. This context-dependent, self-organized, and transient network allows the dynamic temporal binding of the individual attributes of a bistable image as an object by means of selective attention, which is technically realized by means of a synchronous pattern.

2 Memristive Systems

In this chapter, the theoretical foundations of memristive devices and memristive systems are first introduced (Sec. 2.1.1). An overview of the two classes of memristive systems (anion- and cation-based devices) is provided in Sec. 2.1.2, while the memristive systems used in this thesis and their physical foundations are explained in greater detail in Sec. 2.1.4. Finally, memcapacitive devices are described in Sec. 2.2.

2.1 Memristive Devices

Memristive devices belong to the group of dynamical systems, which are nonlinear, passive, and non-volatile, while at the same time, the uncomplicated design of such devices allows a high degree of scalability [15, 56, 82]. The additional properties of such devices, which include fast switching and low levels of power consumption, make them attractive within the field of nanoscale solid-state memory technology. The majority of the research conducted in this field has focused on memristive devices as resistive random access memories (RRAMs) [15,56,83]. But this research on memory technology also found its way towards non-Boolean computing in order to identify a novel solution to the persistent downscaling problem of complementary metal oxide semiconductor (CMOS) technology, which is also known as the problem of Moore's law [15, 56].

Improved techniques and exhaustive investigations have led to continuous expansion in terms of the diversity of memristive devices and their properties over the previous decades. As a result, the range of applications of memristive devices has been widened [15, 83, 84]. The possible applications that have already been investigated include neuromorphic engineering [12, 52], nonlinear information-processing [51], dynamic sensor systems [52], and programmable logic systems [52, 85] [86]. This thesis, however, places particular emphasis on neuromorphic systems.

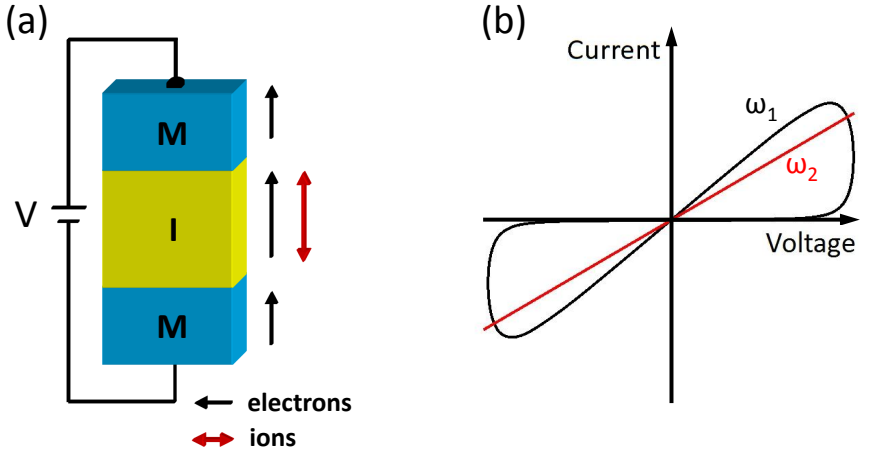

Figure 2.1 Design and functionality of a memristive device: (a) Sketch of a memristive device with an MIM thin layer structure. Possible participations of charge carriers are indicated with black (electrons) and red (ions) arrows. (b) A typical pinched hysteresis in the *I*-*V* curve indicates the memory effect of the memristive device. High angular frequencies ω_2 lead to memory loss [15]. [Adapted from [15].]

2.1.1 Basic Aspects

In 2008, Stanley Williams and his colleagues [50] developed the first bridge between Chua's memristor theory [49] and the hysteresis behavior of resistive switching devices [87, 88]; such behavior had first been experimentally observed at the beginning of the nineteenth century [89]. The memristor postulated by Leon Chua in 1971 completes the square symmetry with the three known basic passive devices: resistors, capacitors, and inductors [49]. The memristor (comprise memory and resistor), which is assumed to be the fourth passive device, store the previously applied electrical potential by a corresponding change of its resistance state; it belongs to the nonlinear devices [56]. The idealized memristor is a specialization of a memristive device, which in turn belongs to the superordinate group of memristive systems [82].

In the simplest case, an experimental realization of a memristive device can be achieved by means of an insulating layer (I) between two metallic electrodes (M) (cf. the metal-insulator-metal (MIM) structure in Fig. 2.1(a)). The non-volatile reversible change of the resistance state of the memristive device primarily occurs in the insulating layer due to the reorganization of that layer as a result of ion movement and redox reactions. Fig. 2.1(b) schematically depicts a current-voltage (I-V) characteristic of an MIM memristive device, with the frequency-dependent pinched hysteresis curve for an applied voltage with a sweep-frequency ω_1 [15]. Extremely high angular frequencies ω_2 force the device to act in a manner similar to that of a linear resistor (cf. Fig. 2.1(b)), which leads to loss of memory hysteresis due to the inertia of the inherent reactions [50, 82, 83].

2.1.1.1 Memristive Systems

A memristive system is defined by particular properties, such as passivity, nonlinear memory storage, and pinched hysteresis [87, 90]. In general, a memory system's performance can be described using the following equations [82, 91]:

$$\dot{x} = f(x, u, t) \tag{2.1}$$

$$y = g(x, u, t)u \tag{2.2}$$

where x is the state variable of the system, which describes both the system's dynamic and memory states. The derivative of x defines the equation of the state. The physical variable y represents the output signal of the memory system, a correlation to the input signal u is given via the scalar function g. The multidimensional function f shows a dependence on the state variable x, the input signal u, and the time t [82,91,92].

An input signal of $u = 0$ produces an output of $y = 0$ according to Eq. (2.2). Consequently, no energy is stored when the system is turned off and it is thus classified as a passive system [82, 90]. Furthermore, phase locking is observed between the input- and output signal. This phenomenon is likewise observed in the Lissajous figures: in particular, the continuous current-voltage (I-V) characteristic of these figures indicates

a frequency-dependent hysteresis through the origin. This hysteresis (cf. Fig. 2.1(b)) represents the dynamic storage of information [82, 92].

The general Eqs. (2.1) and (2.2) used to describe a memory system are adapted to a voltage-controlled memristive system, which leads to the following equations [82, 90]:

$$\dot{x} = f(x, v, t) \tag{2.3}$$
$$i = G(x, v, t)v \tag{2.4}$$

The memductance G is the link between the output current i and the applied voltage v, while, simultaneously, G itself depends on the applied voltage v. The state variable x does not depend on the initial time t_0; therefore, a voltage-controlled memristive system represents a time-invariant system. Thus, the equations can be further simplified by taking into account the time invariance, which leads to the following set of equations [82, 90]:

$$\dot{x} = f(x, v) \tag{2.5}$$
$$i = G(x, v)v \tag{2.6}$$

The precondition of the non-volatility of the state variable x leads to the function $f(x, 0) = 0$, assuming a switched-off voltage $v = 0$. Thus, a fundamental mathematical description of a voltage-controlled memristive system reads [50, 82, 90]:

$$\dot{x} = f(v) \tag{2.7}$$
$$i = G(x)v \tag{2.8}$$

Here, the derivative of the state variable x depends exclusively on the applied voltage v.

In order to further define the state variable x, the memristor model of Strukov *et al.* [50] should be considered. This model, which is based on a real bipolar resistive switch, defines a resistance value R_{LRS} in the low resistance state (LRS) and a resistance value R_{HRS} in the high resistance state (HRS). The resistance states of the physical model in the

boundaries between R_{LRS} and R_{HRS} are described by the state variable x. The state variable is limited to intermediate states in the areas $x \in [0, 1]$, where the borders correspond either to the LRS (1) or HRS (0) of the memristive device. Remaining in the borders results in a time derivative of the state variable x equal to zero (cf. Eq. (2.7)), which takes the extreme values into account [50, 82, 92].

2.1.1.2 Memristor

A memristor is a subclass of the far larger class of the aforementioned memristive systems (cf. Sec. 2.1.1.1) [82]. The functionality of a memristor is based on the relation between the electrical charge q and the magnetic flux φ [93], which was identified by L. Chua [49]. In a first-order memristive system, the state variable x can be replaced in Eqs. (2.7) and (2.8) by the magnetic flux φ [87, 90]:

$$\dot{\varphi} = f(v) \tag{2.9}$$

$$i = G(\varphi)v \tag{2.10}$$

Here, the dependence of the memductance G on the magnetic flux φ leads to nonlinear behavior with a frequency-dependent hysteresis. The same structure as that defined in Ohm's law determines the unit $[G]^{-1} = [M] = \Omega$ for the memristance M [49, 87].

There are individual points of critique concerning the memristor theory of Chua and also of the "found missing memristor" [94–97]. N. Mathur [96] revealed that the functionality of a memristor based on the relation between the electrical charge q and the magnetic flux φ, which was postulated by Chua, is not taken into account in the system described by Strukov *et al.* [50]. Here, magnetic flux is neither electrically recorded on the device nor induced in the system [96]. Another criticism from Vongehr and Meng concerns the fact that a pinched hysteretic I-V curve was previously observed much earlier [94, 95, 98]. In addition, in their publication [97], Meuffels and Soni discuss difficulties encountered in the preparation of a memristor, particularly when doing so on the basis of Strukov's research [50, 97]. This includes the ignoring of basic circumstances of electrochemistry, such as the coupling of the diffusion

currents of ions and electrons. Furthermore, the authors state that a realistic physical device that satisfies the requirements of Eqs. 2.9 and 2.10 does not yet exist and that, in all likelihood, such a type of memristor will remain simply a mathematical concept that is unable to be physically constructed in our world [97].

2.1.1.3 Physical Model

Strukov and colleagues [50] developed a physical 1-D model based on an optimized memristor (cf. Sec. 2.1.1.2). The current-voltage characteristics of the model were compared with experimental investigations of a memristive device with a $Pt/TiO_2/Pt$ layer structure. In a simplified scheme, the memristor model consists of doped and undoped regions that are separated by a boundary. The boundary defines the regions proportionately: A completely doped device would result in a resistance value R_{LRS}, whereas a resistance value of R_{HRS} represents a complete undoped region of the device. The injected dopants are moved by an applied voltage due to their natural charge, which implies a movement of the boundary layer and can be described mathematically using the following equations [50, 90, 92]:

$$\dot{w}(t) = \mu_{\mathrm{V}} \frac{R_{LRS}}{D} i \tag{2.11}$$

$$u = (R_{LRS} \frac{w(t)}{D} + R_{HRS}(1 - \frac{w(t)}{D}))i \tag{2.12}$$

The ion mobility μ_{V} is given for a homogenous area of a semiconductor with device diameter D. The state variable $w \in [0, D]$ defines the state of the system in form of the ratio of R_{LRS} to the total area D of the device. The other part of the area D is determined by R_{HRS}. An increase in the doped region results in a shift of the weighting of R_{LRS} and R_{HRS} towards R_{LRS} [50, 90, 92].

2.1.1.4 Operation Mode

A memristive device varies its resistance state from HRS to LRS and vice versa due to an applied voltage. A switching mode provides information concerning which polarity of the applied voltage is expected to set (LRS)

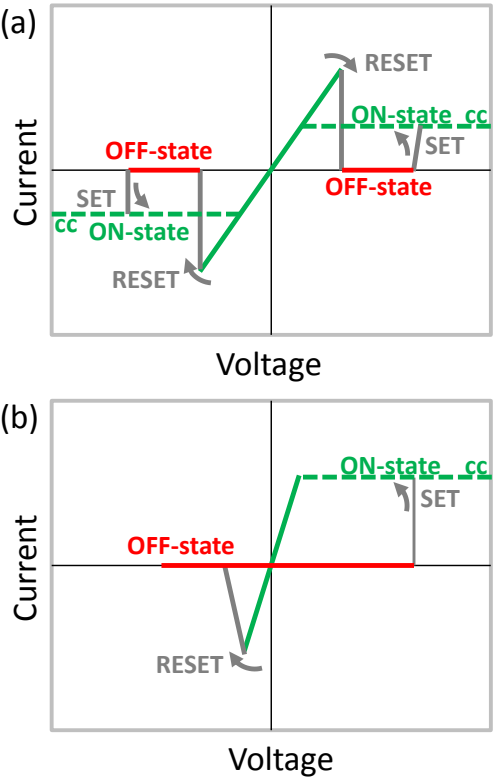

Figure 2.2 *I-V* characteristics of two well-known operation modes. A current compliance (cc) is characterized with a dashed line: (a) Unipolar resistive switching: Both the switching process and the reset process take place in quadrant I and III. The current compliance prevents a reset during the LRS. (b) Opposite polarities for the switch and reset process are characteristic for the bipolar mechanism. The LRS is characterized by a current compliance, which avoids an electrical damage of the device [83]. [Reproduced with permission from [83].]

or reset (HRS) the memristive device. The switching between the states can take place in three different operation modes: unipolar, bipolar, or nonpolar. The *I-V* curves in Fig. 2.2 illustrate the typical characteristics of unipolar and bipolar operation modes, respectively [56, 83, 99].

Unipolar resistive switching is characterized by the fact that the set and reset processes both occur in quadrant I, with a positive polarity, as well as in quadrant III, with a negative polarity, during the same current-voltage sweep (cf. Fig. 2.2(a)). The following requirements apply to the set and reset processes: $V_{set} > V_{reset}$ and $I_{set} < I_{reset}$. However, the set current I_{set} is limited by a current compliance: In the LRS, the reset voltage is already reached ($V_{set} > V_{reset}$); if the current is not limited by a current compliance, an immediate reset would occur. A prerequisite for unipolar switching is fulfilled by using the same electrode material in a symmetrical MIM configuration [56, 83, 99–102].

Bipolar switching is characterized by the fact that, during a current-voltage sweep, the device is set in the LRS in either quadrant I or III. However, an additional necessary criterion is that the reset must occur with an opposite polarity (cf. Fig. 2.2(b)). The current compliance must therefore not protect the device from being reset, but rather prevent it from being damaged by electrical field stress. Bipolar switching is achieved via the use of an asymmetric MIM configuration (diverse metal materials are used for the top and bottom electrodes) [56, 83, 99–102].

Nonpolar is the term used to describe systems that demonstrate both unipolar and bipolar switching [83].

2.1.2 Overview of Various Memristive Systems

After the connection between the memristor theory [49] and the experimental realization of memristive devices was identified in 2008 [50], there was a noticeable increase in interest in the experimental realization of memristive devices [56, 88, 89]. This has led to extensive investigation of the use of a diverse range of materials for the entire MIM device stack, which results in a multitude of resistive switching effects [15]. While there are many possibilities when it comes to classifying these resistive switching effects [99], Waser *et al.* [99] considered it useful to broadly classify the switching effects into three classes: magnetic effects, electro-

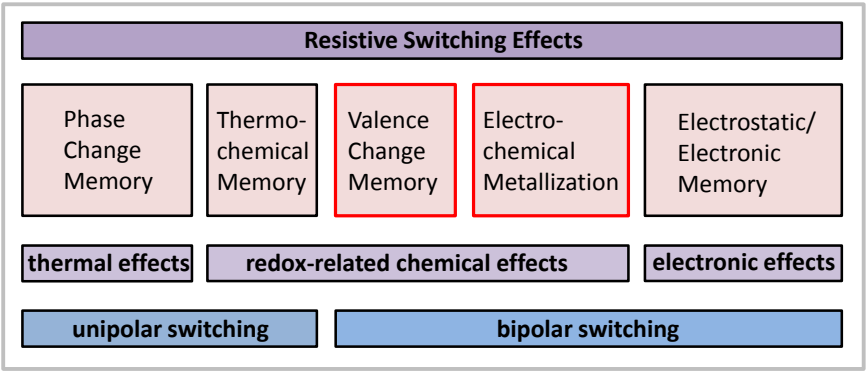

Figure 2.3 A selection of resistive switching effects from the larger classes of electrostatic effects and atomic configuration effects for the application as non-volatile memristive devices with a particular emphasis on electrochemical metallization cells and valence change memories [99]. [Adapted from [15,83].]

static effects, and atomic configuration. It is possible to make further subdivisions within the class of atomic configuration in terms of ions inducing redox effects, in crystallographic phases, in organic molecules, and in mechanical switches. However, any attempt at classification that is harmonized overall is complicated by the various physical processes, which are leading to resistive switching mechanism [99].

A further distinction was made by Waser *et al.* [83] for non-volatile memory utilizations (cf. Fig. 2.3). The memristive devices from this class are also used for the emulation of synaptic properties, as was noted by Ziegler [15]. Their switching mechanisms can be explained to some extent in physical terms. The devices from this group are based on redox-related chemical effects: thermochemical memory effects, valence change memory effects, and electrochemical metallization effects (cf. Fig. 2.3) [15, 83]. A further effect of the use of a memristive device in neuromorphic engineering arises from electronic memory effects [15]. However, within the scope of this thesis, the focus lies on the class of memristive devices, which can essentially be divided into anion- and cation-based devices [56, 83, 99].

2.1.2.1 Anion-based Devices

Anion-based resistive switching, which was first observed in the early years of the 1960s [98], is based on the movement of oxygen ions or of cation interstitials within the insulator layer in an MIM configuration [56, 83]. The preference for the motion of anions, rather than that of highly mobile cations injected by an active electrode, is justified by the selection of the materials used for the electrodes [83]. In the case of anion-based devices, the material properties of the anode electrode (e.g. Au, Pt, etc.) demonstrate a slight tendency to oxidize. Even in the case of oxidation of the metal material used for the anode electrode (e.g. Nb, Ti, etc.), there is no reduction or crystallization of the metal cations to the origin metal at the counter electrode [83]. The reason for this is that the ohmic counter electrode does not demonstrate any willingness to make an ion exchange with the oxidized metal cations [103].

Anion-based devices are also referred to as valence change memories (VCM) because anions contribute to a change in the valence level [56, 99]. The switching of anion-based devices can take place either over a single conducting filament formed in an electroforming step or over the whole surface of a junction of two thin layers. The latter mechanism is referred to as interfacial VCM [99]. The defining property of analogue resistive switching can be achieved in interfacial VCM devices using two approaches: either via a Schottky-like contact or a combination of a memristive layer and a tunnel barrier [99, 104].

There are two well-known models that are intended to explain the homogeneous switching effects of interfacial VCM devices. One model is based on the assumption that there are so-called interface trap states within the memristive layer (cf. Fig. 2.4(a)). These traps can be filled with electrons via tunneling or they can be emptied by jumping out of electrons. Due to the variable number of electrons within the memristive layer, a constant charge shift takes place, which results in an analogue change of the resistance state. It should be noted that the electrons within the memristive layer can only be located in the trap state [99, 104]. The other model (cf. Fig. 2.4(b)), however, assumes that oxygen vacancies are located in the memristive layer and can move freely. The freely moving anions can attach to the junctions of the adjacent layers, which causes an analogue change in the resistance value [99, 104].

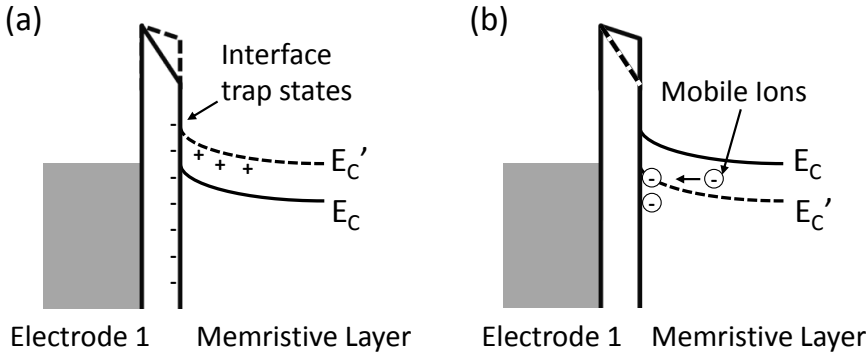

Figure 2.4 Schematic band diagram of interface-based resistance change: (a) Electrons fill traps in the memristive layer or electrons jump out of filled traps, depending on the applied electrical field. However, electrons cannot be in the memristive layer without the traps. (b) The memristive layer can be occupied by negative ions. Sticking to the interface causes a change in the resistance state [99, 104]. [Adapted with permission from [99].]

In general, the ability of selected anion-based memristive devices to make homogeneous gradual changes in resistance is beneficial with regard to the emulation of synapses, as biological synapses experience continuous changes of the synaptic weight. The mechanisms behind anion-based memristive systems are still not completely understood, in contrast to the almost fully understood switching effect found in cation-based devices, which is summarized in the following Sec. 2.1.2.2 [15, 99, 103, 104].

2.1.2.2 Cation-based Devices

A brief overview of electrochemical metallization memory (ECM) cells is provided. Interested readers are referred to the relevant publications of Waser *et al.* [83], Yang *et al.* [56], and Strukov and Kohlstedt [84].

The first investigations into cation-based memristive devices were conducted in the mid-1970s, roughly ten years after the first investigations of anion-based devices [56, 105]. As the name implies, metallic cations of

the active electrode are assumed to be the moving species in cation-based devices. To produce cation migration, either one of the electrodes of the MIM configuration must consist of an electrochemically active material or an enrichment with such a material must already exist in the insulator layer, which can be produced as the result of a preparation process [56]. Therefore, electrochemical metallization memory cell is the common denotation for cation-based devices [106]. Typical electrochemically active materials include the transition metals (e.g. Cu, Ag, Ni) and compounds of this transition metal group (e.g. CuTe) [56]. This transition metals have the property of oxidizing rapidly [102]. Whereas the counter electrode is fabricated of a metal without a tendency to react, such as the noble metals Au, Pt or Ir [56, 102]. The insulating layer between the electrodes consists of materials from the group of the solid electrolytes, nitrides, or insulating oxides [56, 83].

An overview of the switching process of a cation-based device is depicted in Fig. 2.5. The switching is essentially caused by electrochemical effects in the insulating layer of the MIM configuration. In the initial configuration, the memristive device is in its high resistance state R_{HRS} (cf. Fig. 2.5(a)). This phase is characterized by the presence of a solid electrolyte layer without metal atoms M, which are still firmly in the metallic bond of the active layer. A positive switch voltage V_{set} applied to the memristive device leads to dissolution of the metal atoms M from the active electrode in the solid electrolyte (cf. Fig. 2.5(b)(I)) [83]. The resulting negative electrons e^-, as a part of the chemical reaction, disappear in the active layer due to the application of a positive switch voltage V_{set} [107]. The overall reaction can be described using the following equation [83]:

$$M \rightarrow M^{z+} + ze^- \tag{2.13}$$

Here, M^{z+} indicates the separated metal atoms in the insulating layer [83]. The high electric field ensures that the metal cations move through the solid electrolyte to the electrode on the opposite side, the electrochemically inert electrode (cf. Fig. 2.5(b)(II)). At the surface of the counter inert electrode, the metal ions react with the electrons e^- delivered by the cathode. This reduction can be described as follows (cf. Fig. 2.5(b)(III)) [83]:

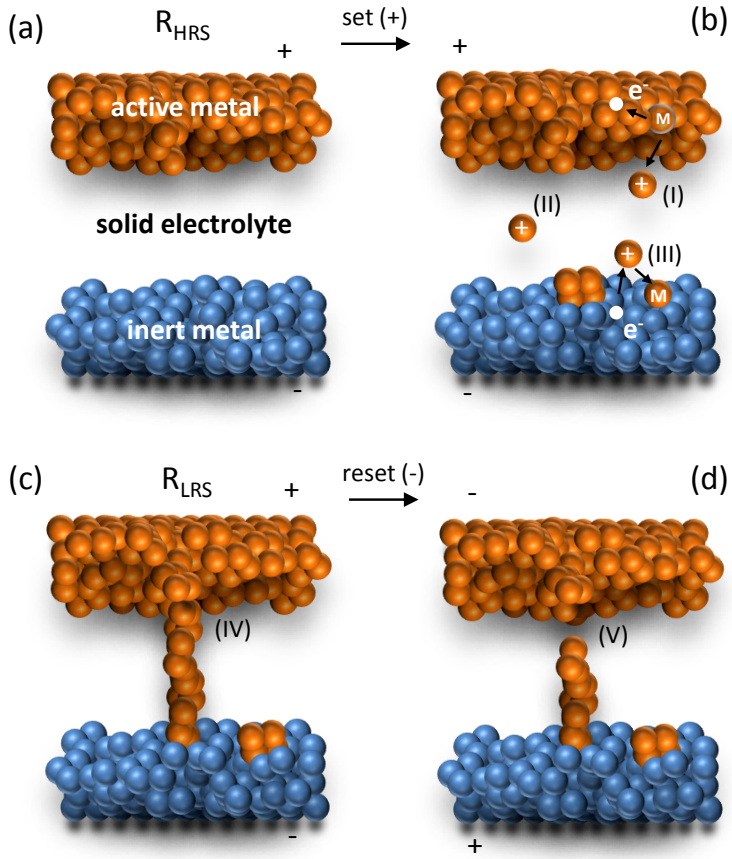

Figure 2.5 Procedure of metallic filament creation in a cation-based device: (a) Sketch of an electrochemical metallization memory (ECM) cell in the initial high resistance state (R_{HRS}). (b) Redox processes at the metal/insulator interfaces lead to a dissolution of cations at the active electrode and to a reduction at the ohmic counter electrode. (c) Closing the metal filament with the active electrode leads to a switching in the low resistance state (R_{LRS}). The current is usually limited by a current compliance. (d) A negative reset voltage leads to an electrochemical dissolution of the conductive metal bridge [108]. [Derivative of [107, 108].]

$$M^{z+} + ze^{-} \rightarrow M \tag{2.14}$$

Hence, the surface of the inert electrode is deposited with metal atoms M from the electrochemically active electrode, which leads a metal filament growing within the insulating layer [83]. Closing the metal filament with the active electrode (see Fig. 2.5(c)(IV)) leads a shortcut (which is usually weakened by a current compliance), which results in a switching from the high resistance state (R_{HRS}) to the low resistance state (R_{LRS}) [83, 102].

A positive voltage applied at the inert electrode effects an electrochemical dissolution of the metal filament, beginning at the surface of the active electrode (cf. Fig. 2.5(d)(V)). Once, the metallic connection between the filament and the active electrode is terminated, the device resistance switches in the HRS. In general, the switching rate results from the steps I-III [83].

2.1.3 Fabrication of Memristive Devices

The development of appropriate memristive devices with layer thicknesses in the nm-regime is a task with many obstacles. Furthermore, there is a need to optimize the device fabrication procedure with respect to the desired functionality in a circuit environment. The devices used in this thesis are based on inhouse developments. Thin technological methods, such as sputtering, evaporation, etching, and lithography, have been applied to fabricate memristive devices with appropriate electrical characteristics [109].

2.1.3.1 Thin-Film Deposition Techniques

Within this thesis, the layer sequences of memristive devices were deposited by thermal evaporation and sputtering. Both belong to the category of physical vapor deposition (PVD) and are widely used in industry and research institutes for numerous applications, such as anti-reflective coatings, tool tribology, or the fabrication of optical and electronic devices. An overview of today's deposition techniques can be found in Ref. [110]. In the following two sections, the basic concept of evaporation and sputtering is described.

2.1.3.2 Thermal Evaporation

Thermal evaporation is one of the oldest techniques for depositing thin films in high vacuum [111]. First, the coating material is placed as pellets in an evaporation boat (crucible), which is typically made of transition metals, such as tungsten or tantalum. These materials are particularly suitable because of their high melting temperature, which must exceed the melting temperature of the coating material [112]. For example, silver (Ag), which is used as a coating material, has a melting point of 962 °C at a pressure of 1 bar (cf. Sec. 2.1.4.1) [113].

The evaporation process begins with a high current flowing through the evaporation boat, which leads to a heating process that achieves the approximate melting point of the coating material. The temperature of the boat can be roughly adjusted by the power defined by the DC current and DC voltage across the evaporation boat. Reaching the melting point, the coating material evaporates in the direction of the substrate, which is located directly above the boat. During this process, only a limited number of collisions occur between the coating material and undesirable particles in the chamber as a result of the high vacuum pressure of typically 10^{-5} - 10^{-6} mbar [112].

For the purposes of this thesis, the Univex 300 system manufactured by the company Oerlikon Leybold Vacuum GmbH was used to grow films at room temperature. The thin film deposition is constantly monitored by a crystal oscillator (Quartz) to ensure a desired thickness of the deposited material [112].

2.1.3.3 Sputter Deposition

The sputtering process is defined by accelerated particles, which knock coating material out of a target, which then disperse everywhere, including on the substrate. The sputtering processes for the memristive devices used were accomplish with a high vacuum experimentation system manufactured by the company Leybold Univex (the 450 B Sputtering System). A sketch of the sputtering system is provided in Fig. 2.6(b). The system consists of three chambers (the main- and separate sputter chambers, and an oxidation chamber), as well as a load lock chamber for loading the samples on a 4-inch holder. The main chamber accommodates up

to eight 4-inch targets, which are the metallic coating materials. All chambers function under high vacuum, which is created by a two pump system. The first step toward obtaining a high vacuum relies on the assistance of a roughing pump. The end pressure of 4 x 10^{-7} is generated by a turbo molecular pump in the second step [109].

The targets in the main chamber are attached to a cathode electrode, as shown in Fig. 2.6(a). The substrate is placed on a sample holder that is positioned on the lower positive electrode. The noble chemical gas Argon (Ar) is utilized as a sputtering gas; it is released in the chamber before sputtering. There are already isolated radioactively ionized argon ions Ar^+ in the gas. The argon ions Ar^+ are accelerated in the direction of the cathode due to the electric field. In this manner, they encounter the target, which is located at the cathode. Through impulse transmission, the target atoms are knocked out of the solid bonds. It should be noted that the impulse transfer from the collision must be higher than the surface barrier represented by the atomic binding. The knocked-out target atoms are spread in all directions, and also towards the substrate. In addition, electrons are also knocked out. Due to the collision of argon atoms with accelerated electrons an increased ionization of argon takes place (cf. Fig. 2.6(a)) [109, 114].

Direct current (DC) sputtering can be used for the metal aluminum (Al), whereas the insulating layer TiO_2 is realized using the reactive sputter deposition method with a gas mixture of argon and oxygen (cf. Sec. 2.1.4.1) [109, 114].

2.1.3.4 Optical Lithography

With the help of lithography, a prestructuring of a wafer surface can be achieved in order to determine the permitted areas for the process steps described in Secs. 2.1.3.2 and 2.1.3.3. There are many modern lithographic processes: Electron-beam lithography, for example, employs an electron beam and can achieve thereby widths of a few nm in the patterning of a wafer [109, 118]. The memristive devices used have area's in the μm^2 range; optical lithography is therefore acceptable for the preparation of these devices.

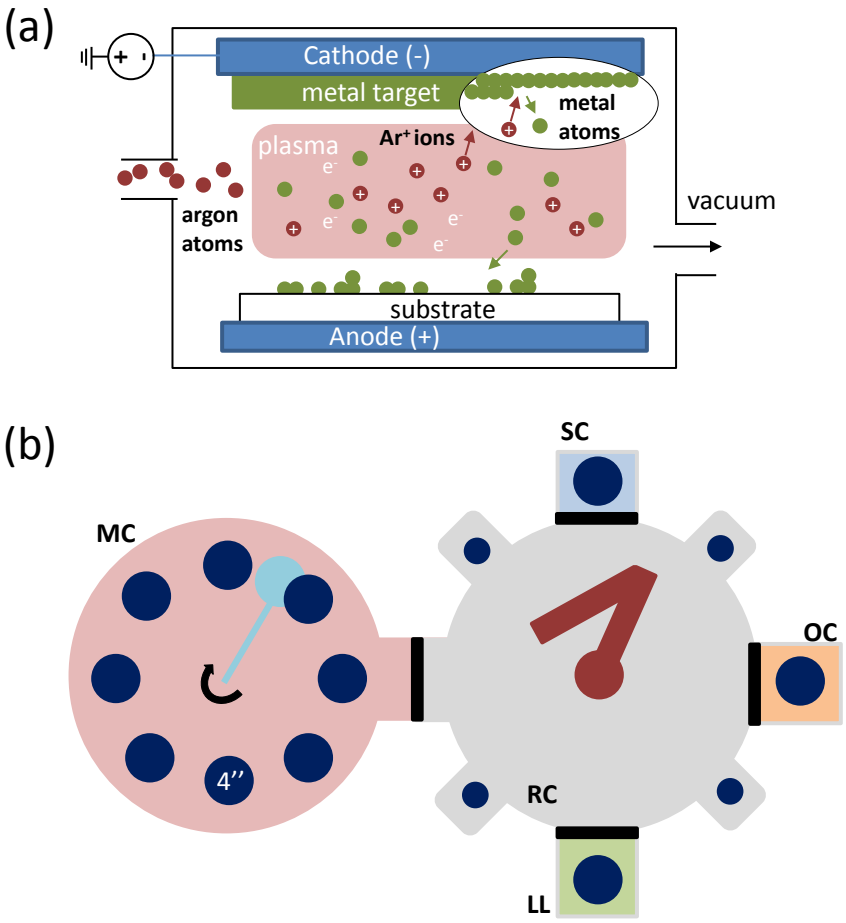

Figure 2.6 Sputter deposition: (a) Schematical cross-section view graph of a sputter chamber, including the Ar plasma and sputtering process. In addition, the lower cartoon in (a) shows the substrate and the thin film formation process [115]. [Derivative of [115, 116].]. (b) Sketch of the chambers of a Univex 450B sputtering unit: the main chamber (MC) with eight 4-inch targets and a holder positioning arm, rest chamber (RC) with a robot arm, separate sputter chamber (SC), and an oxidation chamber (OC) [109]. [Adapted from [109].]

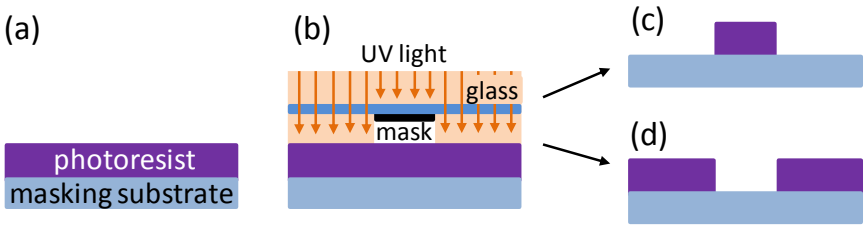

Figure 2.7 Schematics showing a typical lithography procedure: (a) Sample with spin-coated photoresist. (b) Structuring of the photoresist by exposure UV light. (c) Dissolving structure of a positive optical lithography process. (d) A negative resist leads to an inverse structure [117]. [Derivative of [117] / CC BY 4.0.]

In general, optical lithography is a process in which the wafer's surface is patterned by means of ultraviolet (UV) light [109,118]. The individual process steps are depicted, in simplified form, in Fig. 2.7. In the first step, the device surface to be patterned is coated with a liquid light-sensitive photoresist, which is evenly spread by the centrifugal forces generated by a spin coater (a VTC-100A) at high speed (4000 rpm for 30 s). Subsequently, the photoresist, which is partially protected by the mask, is exposed to UV light (cf. Fig. 2.7(b)). Exact positioning of the prefabricated photomask is achieved using a mask aligner (a Karl Suess MA8 Mask Aligner) [109]. The light-sensitive photoresist can be modified in two ways, depending on whether a positive (Fig. 2.7(c)) or a negative (Fig. 2.7(d)) resist is used. A positive resist results in the structure dissolving, as the light disrupts the molecular bonds. The energy of the exposure is used to amplify the molecular bonds of the negative resist and thus, the resist is therefore no longer soluble for developer solution [109,118].

2.1.4 The Memristive Systems Used

Two memristive systems are used for the biologically inspired circuits described in the following chapters. More specifically, ECM cells and a double barrier memristive device were implemented in the neuromorphic

circuits. The ECM cells have the basic Ag/$TiO_{x\text{-}2}$/Al (MIM) structure, but were produced either with a one-step photolithography process (cf. Fig. 2.8(a)) or with a three-step photolithography process (cf. Fig. 2.8(b)). The electrical circuit described in the Sec. 3.5 was equipped with an ECM cell, which was fabricated with a one-step photolithography process in a planar capacitor structure by M. Hansen and M. Ignatov. The circuits discussed in the Secs. 3.8.3, 4.2.1, 4.3, and the circuit in Sec. 4.2.2 were measured with an Ag-doped $TiO_{2\text{-}x}$-based memristive device, using a three-step photolithography process and a double barrier memristive device [104], respectively, which were fabricated by M. Hansen. The memristive devices used are described in the following sections.

2.1.4.1 Ag-doped $TiO_{2\text{-}x}$-based Memristive Devices

The ECM cells were fabricated in a lateral stack using the well-known metal/insulator/metal (Ag/$TiO_{x\text{-}2}$/Al) design, as shown in Fig. 2.8(a,b). The active electrode was implemented with the transition metal silver (Ag). The electrochemically inert metallic material aluminum (Al) was used for the counter electrode of the ECM cell. The solid-state electrolyte of the insulating layer sandwiched between the electrodes consists of $TiO_{x\text{-}2}$. The thickness of the $TiO_{x\text{-}2}$ insulator layer is in the nanometer range; this is in order to ensure a connecting filament between the electrodes within a reasonable electrical field. In this thin insulating layer, a filament composed of Ag atoms grows under the applied electric bias field from the counter electrode to the active electrode due to chemical redox reactions. The titanium (Ti) and niobium (Nb) layers at the bottom are used for a better adhesion of the silver (Ag) electrode. The niobium layer on the top electrode (cf. 2.8(b)) serves as contact pad for the device [10, 15, 16, 73, 83].

The ECM device, which was fabricated in a planar capacitor structure (cf. Fig. 2.8(a)), was prepared using a one-step photolithography process. Owing to the relatively simple structure of a MIM configuration, the memristive device was fabricated layer by layer. The basis of the Ag-doped $TiO_{2\text{-}x}$-based memristive device forms a thermally oxidized Si wafer, where the Ti adherent layer was sputtered with a thickness of 9 nm. Subsequently, the Ag bottom electrode was evaporated thermally

with a thickness of 45 nm. Utilizing a negative photolithography process, windows of 50 x 50 µm were defined by optical lithography in order to deposit a 17.6 nm thin-layer of TiO_{2-x} with the use of reactive sputtering. The lithography process took place in a cleanroom environment. Finally, the top layer consisted of a 140 nm thick Al layer, which was also evaporated thermally [10, 16, 73].

The ECM devices fabricated with a three-step photolithography process (cf. Fig. 2.8(b)) by M. Hansen were fabricated on a crystalline silicon wafer, using thermally grown 400 nm thick oxide film. The device stack consisted of Nb(5 nm)/Ag(40 nm)/TiO_{2-x}(10 nm)/Al(40 nm)/Nb(500 nm). The top layer consists of 500 nm thick Nb, which was deposited with the sputtering system shown in Fig. 2.6 [16].

A typical current-voltage curve of the Ag-doped TiO_{2-x}-based memristive devices is depicted in Fig. 2.8(b). The voltage was swept from 0 to 1.1 V and vice versa in the positive area, whereas the negative range was defined by a voltage sweep from 0 to -0.6 V and back. The sweep rates for the positive and negative voltages were 0.55 V/s and 0.71 V/s, respectively. As a result, the memristive device switched from the initial high resistance state of $R_M = 1$ MΩ to $R_M = 1$ kΩ in the low resistance state at a set voltage of $V_{set} = 0.9$ V. An electrical breakdown in the LRS is avoided by a current compliance of $I_{CC} = 0.2$ mA. The process of resetting to 1 MΩ occurs at a reset voltage of V_{reset} = -0.2 V [10, 16, 73].

The set and reset voltages of the same devices may fluctuate statistically. This is due to the intrinsic processes of Ag-doped TiO_{2-x}-based memristive devices, which are inherently stochastic in nature [10,16,52,73]. More specifically, the voltage pulses effect a migration of the Ag cations, which change the resistance state by establishing a metallic filament between the electrodes [10, 16, 73, 83]. To study this phenomenon in greater detail, 1700 voltage sweeps were performed in order to obtain a distribution of the set voltage (cf. Fig. 2.9). A voltage sweep from 0 to 2 V was applied to an Ag/TiO_{2-x}/Al memristive device, which was protected by a current compliance of $I_{CC} = 0.1$ mA. As a result, the distribution of the set voltage can be described by a Gaussian function with an average set voltage of 0.7 V. The stochastic nature of the memristive devices leads to an unpredictable influence on the transient dynamics [10, 16, 52, 73].

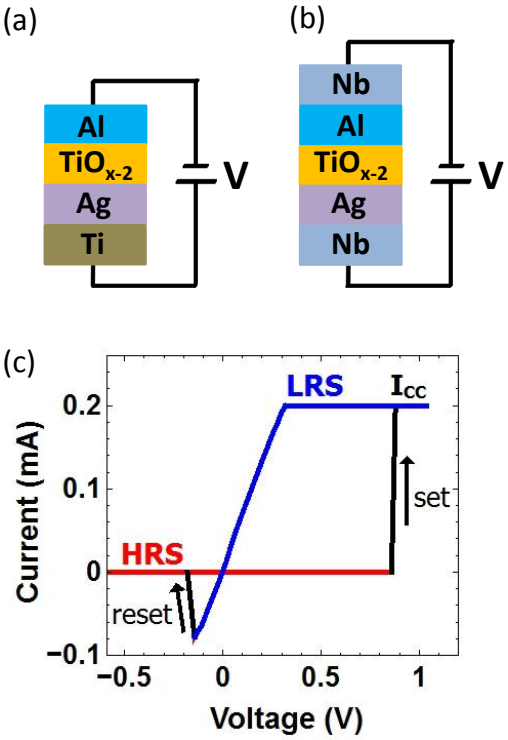

Figure 2.8 Electrical characteristic of ECM cells: (a) Schematic of an ECM cell with the layer sequence Ti/Ag/TiO_{x-2}/Al fabricated in a planar capacitor structure with a one-step photolithography process. (b) A three-step photolithography process was used to fabricate an ECM cell with the layer sequence Nb/Ag/TiO_{x-2}/Al/Nb. (c) A typical *I-V* characteristic of an ECM cell, which represents the functionality of both memristive devices of (a) and (b). A current compliance I_{CC} was set in the positive set cycle. The sweep rates for positive and negative voltages are 0.55 V/s and 0.71 V/s, respectively [10, 16]. [Adapted from [10] / CC BY 4.0.]

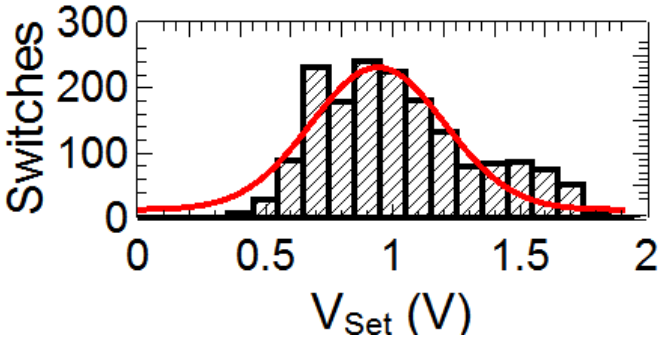

Figure 2.9 Distribution of the switching behavior of an Ag-doped TiO_{2-x}-based memristive device. The sweep speeds are 0.74 V/s and 0.49 V/s, applying a positive and negative voltage sweep, respectively. The set voltage is extracted after 1700 voltage sweeps with a current compliance of I_{CC} = 0.1 mA. The distribution is averaged like a Gaussian distribution (red curve) [16]. [Reproduced from [16] / CC BY-NC 4.0.]

2.1.4.2 Double Barrier Memristive Device

The double barrier memristive device used for the circuit discussed in Sec. 4.2.2 was investigated and prepared by M. Hansen *et al.* [104] of the research unit (RU 2093) [119]. A brief overview of the double barrier memristive device is provided. Interested readers are referred to the relevant publication of Hansen *et al.* [104] or to general publications regarding interfacial switching devices [99, 120–123].

A double barrier memristive device with the thin layer sequence $Nb/Al/Al_2O_3/Nb_xO_y/Au$ [104], as shown in Fig. 2.10(a), is used in this thesis. Oxygen ions are assumed to be responsible for the resistance change of the device. The negative charged oxygen ions are confined between the Al_2O_3 tunnel barrier and the inert gold electrode. By applying an electric field, oxygen ions move either to the Al_2O_3/Nb_xO_y interface or to the top Nb_xO_y/Au interface, in accordance to the field direction. In this way, the tunnel barrier/Nb_xO_y interface and the Nb_xO_y/Au interface are modified by oxidation and reduction, leading to a memristive swit-

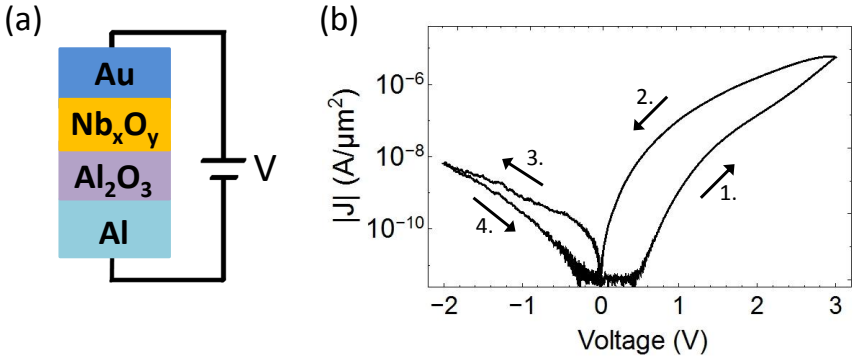

Figure 2.10 Double barrier memristive device: (a) Schematic of a double barrier device stack with the layer sequence $Al/Al_2O_3/Nb_xO_y/Au$. (b) Measured $|J|$-V characteristic of the corresponding memristive device. The sweep speeds are 27 mV/s and 20.4 mV/s, applying a positive and negative voltage sweep, respectively. [Based on [104] / CC BY 4.0.]

ching characteristic. Interesting features of the double barrier devices are the analogue type of switching and that no initial forming step is needed. Further experiments indicated a homogenous interfacial switching effect. Even after hundreds of current-voltage cycles no filamentary kind of $I - V$ curves were obtained [104].

A typical current density $|J|$ versus an applied bias voltage ($|J|$-V) curve with a characteristic homogeneous switching behavior from HRS to LRS, and vice versa, is depicted in Fig. 2.10(b). Generally, the device demonstrated reproducible $J - V$ characteristics due its more controllable non-filamentary resistive switching behavior. In addition to the aforementioned property of continuous switching, the device was also implemented in the circuit (cf. Sec. 4.2.2) due to an intrinsic current compliance. Besides, the retention of the device, which was pronounced when compared to the ECM resistive switches (see Sec. 2.1.4.1), could be biologically motivated within a neuromorphic circuit [15, 104].

2.1.4.3 Electrical Characterization

The prepared memristive devices were electrically characterized. Both the current-voltage (I-V) characteristics and the time measurements were taken using an Agilent E5260 source measurement unit (SMU). The I-V measurements were recorded by sweeping the applied voltage while the current was simultaneously measured. Some of the measurements of the memristive devices were performed with the aid of the partly automatic SUESS Microtec probe station, using two probe holders. The measurements were recorded using a TDS2002B oscilloscope and a TDS7104 oscilloscope [10, 16, 73].

2.2 Memcapacitive Devices

Di Ventra and his colleagues [91] expanded the class of memory based devices, which also involves a memristor, to include memcapacitors and meminductors. Such memelements are characterized by a physical intrinsic state variable that reflects the memory functionality of the device. In particular, changes to the device-specific intrinsic state variable are memory induced [106]. The memory effect of a memristor is demonstrated by a frequency-dependent pinched hysteresis in the corresponding current-voltage characteristic (cf. Fig. 2.1(b)). A comparative hysteresis is observed in the charge-voltage curve and in the current-flux characteristic of a memcapacitor and of a meminductor, respectively [91].

In the context of this thesis, the memcapacitor is of particular interest, as it allows for the storage of information with a capacitance and thus makes it possible to integrate a memory effect in neuromorphic circuits, which commonly rely on commercial capacitors (cf. Sec. 3.4.1). Like the memristor, the memcapacitor is among the series of non-volatile devices, which can also be used in the field of non-volatile storage technology [91,124–127]. In 2010, Pershin and Di Ventra [126] used a memristor emulator embedded in an active circuit in order to demonstrate memcapacitive functionality.

The equations used to describe the concept of a memory system (see Sec. 2.1.1.1), in particular the Eqs. (2.1) and (2.2), are adjusted to suit

a memcapacitor. This results in a system of charge-controlled memcapacitors, which can be described using the following set of equations [91]:

$$\dot{x} = f(x, q, t) \tag{2.15}$$

$$V_C(t) = C^{-1}(x, q, t)q(t) \tag{2.16}$$

The charge $q(t)$ on the capacitor is defined at each time t. The appropriate voltage is given with $V_C(t)$. The inverse memcapacitance C^{-1} is subject to the state variable x of the system, which defines the memory effect [91].

The memory effect of the memcapacitor is demonstrated by the temporal dependence on the charge flow. Therefore, Eqs. 2.16 and 2.15 are adapted to a charge-controlled memcapacitive system [91]:

$$V_C(t) = C^{-1}\left[\int_{t_0}^{t} q(\tau)d(\tau)\right]q(t) \tag{2.17}$$

With respect to the following assumption, the initial time t_0 can be defined as $t_0 = 0$ [91]:

$$\int_{-\infty}^{t_0} q(\tau)d(\tau) = 0 \tag{2.18}$$

Since the memcapacitor, as a memristor, is a passive device, the charge-voltage $(q - V)$ curve goes through the origin. As a result, a property of the described memcapacitor implies that a charge q equal to zero means that, at any time, the voltage V is zero as well, which is also recognizable by the Eq. 2.16 [91].

2.2.1 Experimental Implementation: Memcapacitor Realized with a Memristive Device

For the purposes of this thesis, a memcapacitor is realized experimentally, as shown in Fig 2.11. Therefore, an Ag-doped TiO_{2-x}-based memristive device in a planar capacitor structure (cf. Sec. 2.1.4.1) is used. In particular, the subcircuit is composed of the memristive device in parallel to the capacitor C_2 of a capacitive divider, which consists of C_1 and C_2.

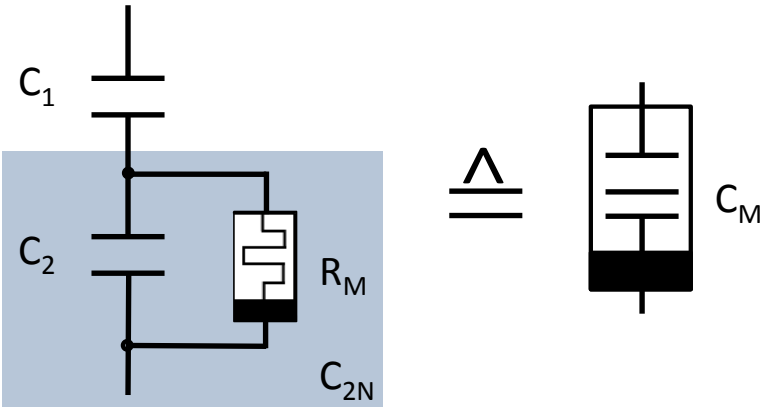

Figure 2.11 A sketch of the experimental implementation of a memcapacitor exploiting an Ag-doped TiO_{2-x}-based memristive device [10]. [Adapted from [10] / CC BY 4.0.]

The memristive device R_M and the capacitor C_2 are combined to form an RC element, referred to as C_{2N}, as shown in Fig. 2.11 [10].

The resistance state of the memristive device R_M in this subcircuit is influenced by the progress of the charge flow through it, resulting in the following dependency: $R_M = R_M(q,t)$. The resistance state of the memristive device R_M influences the overall capacitive state of the capacitive divider C_M. This can be seen more clearly in the following equation [10]:

$$C_M = \frac{C_1 C_{2N}}{C_1 + C_{2N}} \; with \; C_{2N}(u_M, R_M, t) \tag{2.19}$$

$$= \frac{1}{u_M}(q(t) - q_M(u_M, R_M, t)) \tag{2.20}$$

where u_M is the voltage across the parallel connection C_{2N}. The variable q represents the charge through the capacitive branch, whereas the stored charge between C_1 and C_{2N} is referred to as q_M. Thus, there is a dependence of C_{2N} on $R_M(q,t)$, which agrees with the theoretical definition of a memcapacitor offered by Di Ventra *et al.* [91] [10].

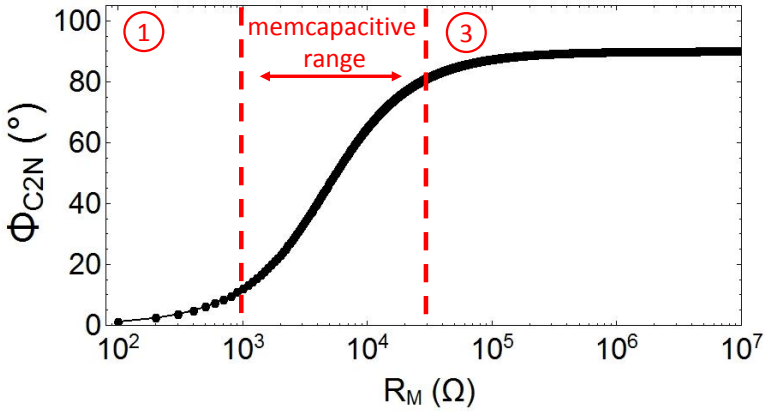

Figure 2.12 Calculation of the phase $\phi_{C_{2N}}$ of the network C_{2N} depending on the resistance of the memristive device R_M. The numbers 1 and 3 refer to the regions [10]. (cf. Ch. A) [Adapted from [10] / CC BY 4.0.]

The functionality of such a memcapacitor can be further analyzed by considering the parallel connection C_{2N}. Therefore, the total impedance of C_{2N} can be determined using the following equation [10]:

$$Z_{C_{2N}}(R_M) = \frac{1}{\frac{1}{R_M} + j\omega C_2} \tag{2.21}$$

Here, ω is the angular frequency. To better understand the influence of the memristive device R_M on the memcapacitive system C_M, the impedance phase $\phi_{C_{2N}}(R_M)$ of the total impedance $Z_{C_{2N}}(R_M)$ is considered. Therefore, the impedance phase $\phi_{C_{2N}}(R_M)$ was plotted against the resistance of the memristive device R_M by applying Eq. 2.21 (cf. Fig. 2.12). As a result, the impedance $Z_{C_{2N}}(R_M)$ acts in a manner similar to that of a linear resistor for an impedance phase of $\phi_{C_{2N}}(R_M) \approx 0°$ (region 1 in Fig. 2.12). However, the subcircuit behaves almost like a capacitor with a constant capacity providing an impedance phase of $\phi_{C_{2N}}(R_M) \approx 90°$ (region 3 in Fig. 2.12). The region in between demonstrates typical memcapacitive characteristics, with a change in the effective capacitance. In particular, a deviation from the purely capacitive behavior of C_{2N} is

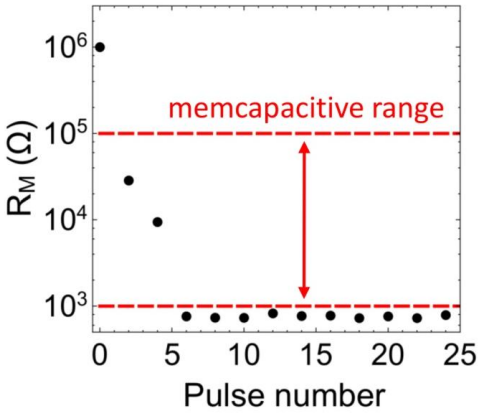

Figure 2.13 Resistance change of the memristive device R_M depending on the number of applied pulses with a voltage amplitude of 10 V and pulse width of 2 ms including the memcapacitive range from Fig. 2.12 [10]. [Reproduced from [10] / CC BY 4.0.]

achieved whenever the phase $\phi_{C_{2N}}$ between R_M and C_2 is less than 90°. Thus, R_M must be chosen in dependency of the capacitor C_2 [10].

The Ag-doped TiO_{2-x}-based memristive device (cf. Sec. 2.1.4.1) satisfies the requirement of being able to switch between purely capacitive and resistive behaviors since the measured resistance varied within the memcapacitive area (cf. Fig. 2.13). To be more precise, single constant voltage pulses of 2 ms and an amplitude of 10 V were applied to the memristive devices while the resistance was measured. As a result, the subsequently applied voltage pulses decreased the resistance of R_M from $R_M = 1$ MΩ to $R_M = 1$ kΩ within the first four pulses. In particular, there was a transition of the impedance C_{2N} from region 3 to region 1, as shown in Fig. 2.12. In the HRS of the memristive device, the impedance C_{2N} behaved almost like a capacitor $Z_{C_{2N}} \approx C_2$, while, in the LRS, the impedance acts in a manner similar to that of a linear resistor $Z_{C_{2N}} \approx R_M = 1$ kΩ [10].

3 Emulation of Neural Activity and Plasticity with Memristive Systems

The human brain encodes environmental sensory information into sequences of spikes. The decisive foundation for this coding scheme is the correlation between the intensity of a stimulus and the spiking activity of neurons. This led to the emergence of spiking neuron models, which resulted in significant progress in the emulation of neural dynamics [10]. Very large scale integration (VLSI) technology [47] is the leading technical approach, when it comes to the physical realization of bio-inspired neuronal circuits owing to the variety of advantages it offers: highly parallel computing, analogue operation, and real-time processing [15]. In 1991, Mahowald and Douglas [128] have impressively demonstrated underlying mechanisms of neurons with such an energy-efficient circuit [15]. In general, further promising improvements for neuromorphic circuits were achieved using non-volatile memristive devices. In this regard, the focus was on the ability of memristive devices to emulate dynamic synaptic properties with a single device [15]. In addition to the use as single synaptic device, Pickett *et al.* [129] used a memristive neuristor circuit to emulate the all-or-nothing spiking of neurons by exploiting the negative differential resistance of nanoscale MIT memristors. However, dynamical neural activity pattern cannot be demonstrated by a memristive neuristor circuit. For the first time, a memristive spiking neuron model that demonstrates dynamic spiking patterns, including adaptation, is experimentally implemented in the research conducted for this thesis [10].

The objective of this chapter is to introduce spiking neuron models (cf. Sec. 3.4) and to demonstrate the advantages that memristive devices offer

for these circuits. First, an overview of the electrophysiological properties of neurons is provided (Sec. 3.1). State-of-the-art spiking neuron models are described in Sec. 3.4. Thereafter, a detailed description of an experimentally implemented memristive spiking neuron model is provided that demonstrates frequency coding and frequency adaptation (see Sec. 3.5). Finally, a PUT-based van der Pol oscillator circuit is presented (Sec. 3.8).

3.1 Electrophysiological Properties

Neurons and synapses represent the fundamental information-processing units in the neuronal system [15]. The human brain network is composed of approximately 10^{11} neurons, which are linked to each other via 10^{14} possible synaptic connections [130]. A unidirectional interaction between neurons takes place via approximately 3.5 ms long voltage pulses (called spikes) with a peak to peak amplitude of roughly 100 mV [131]. This neural activity takes the form of all-or-nothing behavior [132]. A single synapse is altered by the all-or-nothing firing of adjacent neurons because synapses are not rigid. Therefore, the corresponding mechanism of synaptic plasticity is essential to learning and memory processes [15].

A comprehensive overview of the electrophysiological properties of the basic units is provided by Born *et al.* [132] in the book "*Biologie Oberstufe Allgemeine Ausgabe Gesamtband Oberstufe*". The overview of the terms that are important to this thesis provided in this section is based on translations of some aspects of this publication.

3.1.1 Structural Properties of Neurons

The neurons in the neural network have a basic structure, which is specialized in the transmission of action potentials, in common. The structure of an archetypical neuron can be considered in terms of the input (dendrites), the processing (soma), and the output (axon) of neuronal activity, as sketched in Fig. 3.1 [10, 132]. To elaborate, the soma is the cell body of a single neuron; it is characterized by the cell nucleus, which contains genetic information. The functionality corresponds to a processing unit [10, 132].

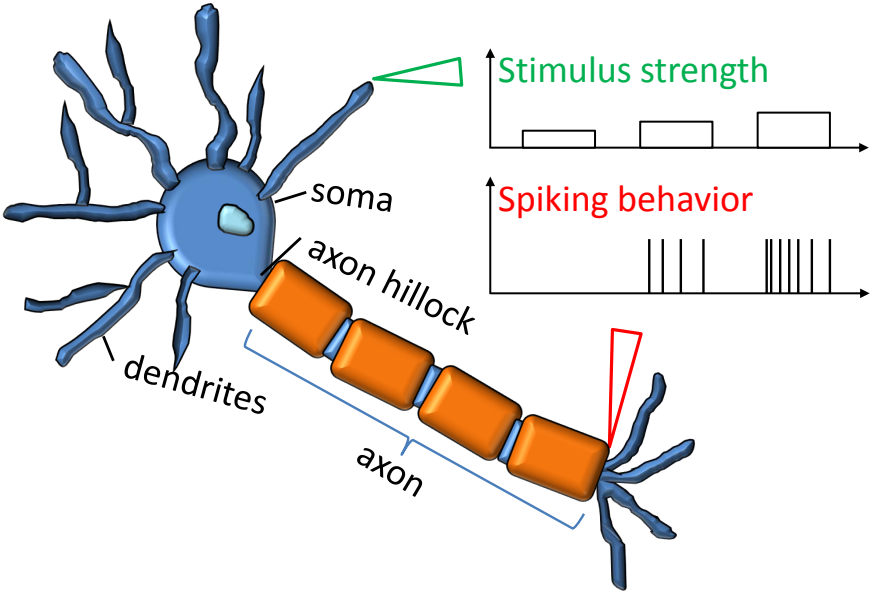

Figure 3.1 Simplified depiction of responses to stimuli. The sketch of a neuron illustrates the dendrites, the soma, and the axon. The stimulus strength secured at the dendrites, which are referred to as input, arises in three different intensities, as shown in the inset. The soma acts as a processing unit. The spiking behavior caught at the axon (output) indicates the frequency in dependence to the stimulus strength [10]. [Adapted from [10] / CC BY 4.0.]

Dendrites are long, thin branches that spread from the cell body in all directions. As a result, they provide as much contact surface as possible in order to connect to different neurons simultaneously and to receive input stimuli from them. The input stimuli are received via synaptic connections [132] and are transmitted by the dendrites to the soma to be processed [10, 132].

The axon is a kind of transmission line and extends as a long branch from the cell body. The axon carries the electrical nerve signals received from the dendrites, even over long distances, away from the soma as action potentials towards other, subsequent postsynaptic neurons. The axon is surrounded by myelin sheaths, which accelerate the transmission speed of the spikes. The end of the axon is linked to up to 1,000 dendrites of other neurons via synapses [132]. An important unit of the cell body is the axon hillock (cf. Fig. 3.1). The generation of action potentials in the axon hillock is triggered when a certain threshold value is reached [132, 133].

3.1.2 Generation of an Action Potential

An action potential represents a characteristic deviation of the membrane potential from the resting potential (the black curve in Fig. 3.2(a)). The process of generating an action potential can be divided into individual phases [132].

In the initial state, the membrane potential is approximately -70 mV. This resting potential arises from the differing ratio of ion concentrations inside the cell when compared to the extracellular medium [132]. The ions that are primarily responsible for the concentration gradient are the positively charged sodium (Na^+), potassium (K^+), calcium (Ca^{2+}), and negatively charged chloride (Cl^-) [134]. The ion concentration in the resting state is determined by the ion (Na^+-K^+) pumps and ion (K^+) channels that are embedded in the otherwise electrically insulating membrane. The open K^+ channels enable a leakage of current flow. However, the resting potential remains almost constant since an equilibrium state between chemical and electrical gradient consistently occurs with the aid of the ion pumps [132].

The sum of the incoming stimuli received by the dendrites emerges from the chemical conversion of the spikes generated by the pre-neurons. At the

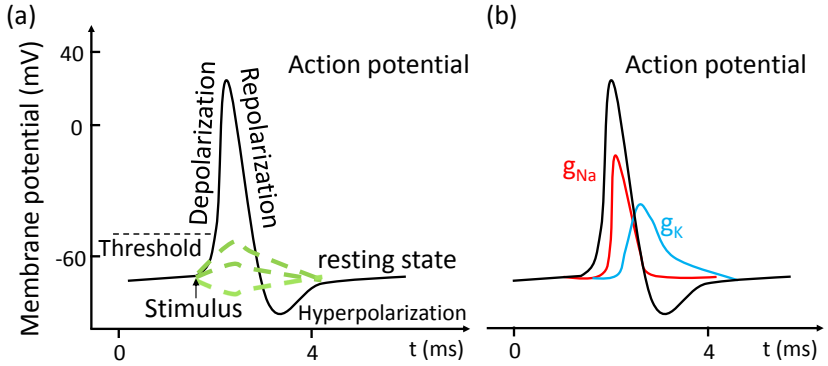

Figure 3.2 Detailed description of an action potential: (a) The membrane potential of a neuron can react passively (green line) or actively to input stimuli. [Derivative from [132].] (b) The corresponding sodium and potassium ions in red and blue, respectively [132]. [A similar figure is published in [135].]

axon hillock, the postsynaptic (membrane) potential (PSP) influenced by the input stimuli is compared with the constant threshold of -35 mV [132]. The intensity of the input stimuli determines the reaction of the neuron: Subthreshold stimuli lead to a passive reaction of the neuron due to the postsynaptic membrane potential being lower than the threshold (the dashed green lines in Fig. 3.2(a)). In this case, the membrane potential will temporarily differ slightly from the resting potential, in the manner of a capacitor, which is charged and then discharged. However, stimuli that raise the postsynaptic membrane potential above the threshold of -35 mV induce an action potential by depolarizing the membrane potential (cf. Fig. 3.2(a)). This leads to an opening of the voltage-gated Na^+ channels, leading to a Na^+ flow into the cell (cf. Fig. 3.2(b)), which causes a sharp increase of the membrane potential during the depolarization phase [132].

The explosive increase that occurs during the depolarization phase can be explained by the positive feedback: The membrane potential increases due to the entering of Na^+ ions, which leads to an increased opening of voltage-gated Na^+ channels due to an increased positive concentration inside the cell. A steady-state Na^+ gradient is reached at a membrane

potential of +30 mV, which closes the Na^+ channels [132].

The positive concentration achieved within the cell in turn causes an opening of the K^+ channels after a time delay. The positively charged K^+ ions flow from the interior of the cell to the extracellular medium. This causes the voltage to drop further, which corresponds to a repolarization of the cell membrane. The K^+ channels are deactivated at a membrane potential of -70 mV. Due to the inertia of the K^+ channels, the membrane potential drops below the resting potential, which is referred to as hyperpolarization phase. The time between the beginning of the hyperpolarization phase and the recovery of the resting potential is referred to as the refractory period. The refractory period is characterized by the suppression of further action potentials within this period [132].

3.1.3 Excitation Transfer between Neurons

The synapse is used for excitation transmission from the presynaptic neuron to the postsynaptic neuron. The action potential generation (cf. Sec. 3.1.2) within a neuron is electrical in nature. The exchange of signals between two neurons via the synapse only occurs in an electric manner in some cases, via the so-called electrical synapses [132]. However, for a formation and learning mechanism, chemical synapses, where the electrical signal is converted to a chemical, are of particular importance [15, 132]. The chemical synapse can be divided into three segments: the axon terminal of the presynaptic cell, with synaptic vesicles that contain the neurotransmitter; the membrane of the dendrites of the postsynaptic cell, with transmitter-gated ion channels; and the synaptic cleft between them [132].

Excitation transmission via the synapse begins with an action potential transmitted by the axon to the axon terminal of the presynaptic cell. This results in an opening of the voltage-gated Ca^{2+} channels, leading to a Ca^{2+} flow within the axon terminal of the presynaptic cell. The increased calcium concentration in the axon terminal triggers the vesicle to release the neurotransmitter in the synaptic cleft by means of exocytosis [132]. The neurotransmitter released in the synaptic cleft sticks to the receptors of transmitter-gated ion channels at the postsynaptic membrane, which causes an opening of the ion channels, producing an ionic current. Thus, the postsynaptic membrane is electrically excited as a function of the

distributed transmitter of the presynaptic neuron [132].

3.2 Neural Coding

Neural coding describes the interrelation between input information and the neuronal response. The information always represents the duration and the intensity of the input stimulus. Information is translated, in neurons, into a deviation of the membrane potential [132]. There are many theories concerning the coding mechanisms of a neuron [136]: One theory speculates that information is encoded in the number of generated spikes within a certain time interval [10]. This so-called frequency coding was followed by further hypotheses, such as temporal coding, population coding, and sparse coding [136]. In the following section, temporal and frequency coding, including frequency adaptation, are explained in greater detail.

3.2.1 Temporal Coding

Temporal coding is based on the hypothesis that information is coded according to the temporal duration of the input stimulus. The time at which an input stimulus is received is inevitably linked to the time at which a neuron responds. Thus, the timing of the input stimulus is of particular interest. Temporal coding can be implemented, for example, through a frequency coding scheme [137].

3.2.2 Frequency Coding

The input stimulus received by a neuron is translated into an action potential firing rate (cf. Fig. 3.1) [10]. This so-called frequency coding in sensory neurons was first investigated by E.D. Adrian [4, 5] in 1926 [10]. The duration and intensity of the input stimulus is not encoded in the amplitude or the width of a single spike, as every action potential generated within an individual neuron has the same structure. Therefore, the approach used to continuously generate action potentials is chosen based on the temporal process of excitation [132]. The spike timing is therefore not important; however, the number of spikes received within a

period of time is relevant. Thus, the intensity of the stimulus determines the frequency of the spike train [10, 132, 137]. The following correlation can be observed between the intensity of the input stimulus and the number of pulses generated within a specific time interval: A weak input signal results in a limited number of pulses being generated within a time interval, whereas a comparatively stronger input stimulus results in a greater number of spikes being generated. Thus, the number of spikes generated depends on the strength of the input stimulus; in this manner, a comprehensive digital coding, in the form of a firing rate, is gained at the output. The temporal appearance of the spikes does not necessarily occur at regular intervals; however, it predominantly occurs in irregular temporal patterns (see Fig. 3.1) [10, 132].

Today, the frequency code hypothesis is no longer exclusively applied to receptor neurons, as it has been applied to large sections of the brain, such as the primary visual cortex, the somatosensory cortex, the auditory cortex, and the place cells in the hippocampus. Furthermore, a higher processing mode than sensory transduction, in which a sensory input stimulus is transferred in another form, such as an action potential, is represented by this hypothesis [6–11, 132].

3.2.2.1 Neuron Models of Type I and Type II

Neuron models are classified into two categories: type I and type II. In order to further determine the two models, the frequency of the oscillation is examined in dependence on the applied current i, as shown in Fig. 3.3(a). The type I neuron model shows no oscillation up to a threshold current I_θ. If this threshold current is reached, the frequency increases continuously with an increased current i (the upper graph in Fig. 3.3(a)). The neuron of the type II, on the other hand, jumps to a frequency $f_\theta > 0$, when reaching the threshold current I_θ, although no oscillation has taken place for currents smaller than the threshold. However, after reaching the threshold current, the oscillation frequency of the type II neuron model increases continuously, starting with the frequency f_θ, with an increased current (the lower graph in Fig. 3.3(a)) [138].

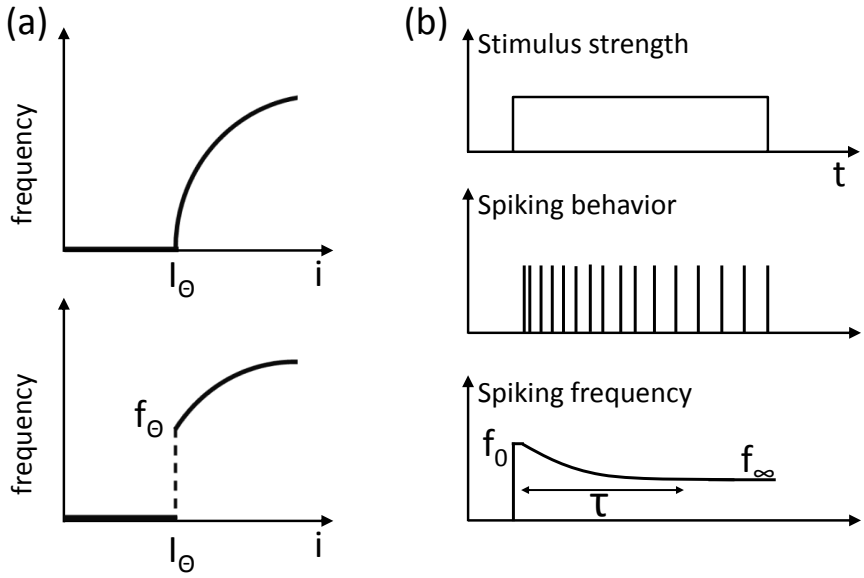

Figure 3.3 Characteristic properties of a neuron: (a) Upper graph: Fire frequency of a type I neuron as a function of the input current i with a continuous increase in the fire rate starting at the threshold I_θ. Lower graph: Fire frequency of a type II neuron as a function of the input current i with a jump in the fire rate at the threshold I_θ. From that threshold, the fire rate increases continuously [138]. [Adapted with permission from [138].] (b) Relationship between the strength of an input stimulus and the spiking behavior of a neuron including frequency adaptation, as proposed by E. D. Adrian in 1926 [4, 5]. The initial frequency f_0 decreases after the time τ to the frequency f_∞ [139, 140]. [Adapted from [139].]

3.2.3 Frequency Adaptation

Frequency adaptation refers to the adjustment of a neuron to a constant stimulus in the form of a transiently reduced firing rate (cf. Fig. 3.3(b)) [10], as first observed by E. D. Adrian in 1926 [4, 5]. The requirements for adaptation are the habituation of the receptor and organisms to a constant stimulus. Adrian assumed a direct link between the degree of decrease in the firing rate and the extent of habituation to a stimulus [5,10]. Adaptive behavior in the neuronal system was first recognized in sensory systems, which are known to adapt to changing environmental conditions [8, 10]. However, research has indicated that nearly every spike-generating neuron in the neuronal system demonstrates frequency adaptation [10, 139]. According to E. D. Adrian [4, 5], this adaptation phenomenon can be found in all living creatures. From a biological point of view, the assumption has been put forward that there adaptation to the environment occurs on nearly any level of a biological system [6, 10, 141] in order to be better adapt to environmental changes [10]. Frequency adaptation within the spike train of a spiking neuron is presumed to represent the basis for the synchronization of neuronal assemblies and selective attention [6, 10, 142].

The concept of frequency adaptation in a spiking neuron is depicted in Fig. 3.3(b): A constant stimulus strength is applied to a spiking neuron. Initially, the neuron has the firing frequency f_0 [139, 140]. Rather than remaining constant, the firing frequency decreases continuously due to adaptation until the steady-state frequency f_∞ is reached. In a biological neuron, the adaptation time constant τ varies from the range of milliseconds [143] to several seconds [144] [139, 140].

3.3 Synaptic Plasticity

Synaptic plasticity forms the basis for learning and memory processes in a neural system, as it allows for changes in the coupling strengths between neurons as a result of their neural activity [15]. The functional connection is either potentiated or depressed as a result of neural activity patterns [12].

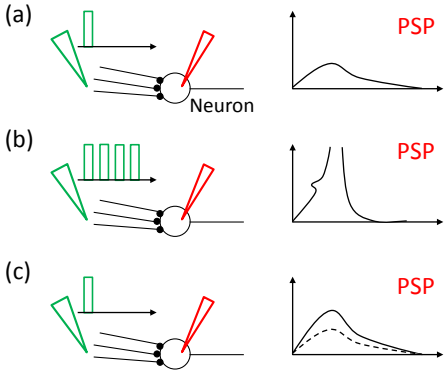

Figure 3.4 Long-term potentiation based on pulses, which leads to diverse postsynaptic potentials (PSP): (a) A single pulse causes a slight change of the postsynaptic reaction. (b) A high-frequency pulse train induces a postsynaptic action potential. (c) A single pulse causes a larger PSP compared to (a) after the high-frequency pulse train [9]. [Adapted with permission from [9].]

3.3.1 Long-Term Potentiation

Synapses in the nervous system have the ability to respond to sustained characteristic neural activity patterns by increasing or decreasing their synaptic efficacy, which is also referred to as long-term potentiation (LTP), or its opposite, long-term depression (LTD), respectively [14, 16, 19]. Long-term potentiation is widely assumed to be the basic requirement for learning and memory processes since memory is believed to be encoded in synaptic strength changes. For the LTP process, the rate of arrival of spikes at the corresponding synapse within a time frame ΔT is crucial; this is schematically represented in Fig. 3.4 [9,16]. To clarify, pulse trains were applied to the dendrites of a neuron while the activity in the cell body was measured. In Fig. 3.4(a), a single pulse is applied to the dendrites, which leads to a change in the postsynaptic membrane potential (PSP), but it is insufficiently strong to trigger an action potential. Subsequently, the application of a voltage pulse train with a sufficiently high frequency led to the generation of an action potential (cf. Fig. 3.4(b)). Finally,

the single pulse was found to be the same as at the beginning, as shown in Fig. 3.4(c). However, there was a clear increase in the PSP when compared to the initial pulse. As a result, a high-frequency pulse train led to long-lasting enhancement of the synaptic strength [9].

Long-term potentiation demonstrates the properties expected of physiological memory processes, such as input specificity, cooperativeness, persistency, and associativity [9, 15]. Input specificity leads to an exclusive strengthening of a particular synaptic weight, defined by the neural activity of adjacent neurons, rather than concluding the neural activity of all of the neurons in a nervous system [15]. The property cooperation refers to a raised likelihood of the LTP process occurring as the result of rising presynaptic neural activity being triggered by one or more neurons [15]. A period of high synaptic activity leads to a persistent synaptic change [9]; this association indicates that a strengthening of one synapse results in a weakening of other synapses, leading to slight changes throughout the entire network [15].

3.3.2 Hebbian Learning Rule

In 1949, the Hebbian learning rule was published by the psychologist Donald Hebb, who described learning as a process that involves modification of synaptic weight. In particular, the activities of both the pre- and postsynaptic neuron influence synaptic change in the following manner [17, 145]:

"*When an axon of cell A is near enough to excite a cell B and repeatedly or persistently takes part in firing it, some growth process or metabolic change takes place in one or both cells such that A's efficiency, as one of the cells firing B, is increased.*" [17], p.62

This learning rule both made it possible to explain biological processes and provided the mathematical basis for the learning mechanism at the cellular level [15]. A cellular learning rule can be mathematically described as follows [15]:

$$\frac{d\omega}{dt} = F(\omega(t), v_{pre}, v_{post}) \tag{3.1}$$

$$with \quad v = \frac{\#Spikes}{\Delta T} \tag{3.2}$$

where $d\omega/dt$ describes the rate of change of the synaptic weight, which is based on the synaptic weight $\omega(t)$ and the activity of the pre- (v_{pre}) and post- (v_{post}) synaptic neuron. The activity of each neuron can be defined with reference to the number of spikes generated ($\#Spikes$) within a certain time interval (ΔT) (cf. Eq. 3.2) [15]. According to the Hebbian learning rule, there is no influence on the synaptic strength whenever only one of the two neurons shows neural activity. Thus, the Hebbian learning rule reads as follows [15]:

$$F(v_{pre}, v_{post}) = \beta v_{pre} v_{post} \tag{3.3}$$

Here, the constant β is the learning rate [15].

While many models focus on individual biological processes (e.g. level of calcium concentration) when describing the function F [15], input specificity, cooperativeness, persistency, and associativity form the basis of learning and memory processes (cf. Sec. 3.3.1) [9, 15].

3.3.3 Spike-Timing-Dependent Plasticity

Spike-timing-dependent plasticity (STDP) concerns the synaptic strength change $\Delta\omega$ that occurs due to a causal link between the presynaptic spike at t_{pre} and the postsynaptic spike at t_{post} (cf. Fig. 3.5). The change of the synaptic strength between two interconnected neurons is determined by the time intervals at which the neurons were active, which can be more precisely expressed by the difference: $\Delta t = t_{post} - t_{pre}$ [12]. Thus, the change in the synaptic weight depends on the individual spikes generated with the time difference Δt and leads to the following dependency function: $\Delta\omega = \xi(\Delta T)$. Here, ξ is a STDP learning function. The generation of a spike in the presynaptic neuron before the

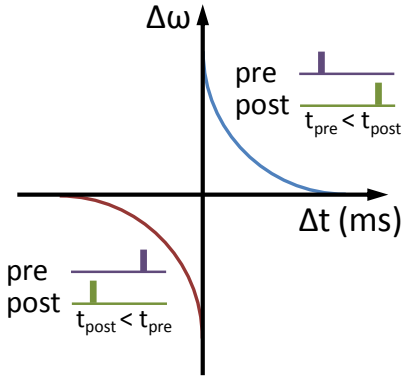

Figure 3.5 Spike-timing-dependent plasticity: A spike generated in the presynaptic neuron before the postsynaptic neuron fires ($\Delta t > 0$) leads to a strengthening of the synaptic weight ($\Delta\omega > 0$), whereas neural activity of the postsynaptic neuron before the presynaptic neuron ($\Delta t > 0$) results in a weakening of the synaptic weight ($\Delta\omega < 0$) [12]. [Adapted from [146] / CC BY 4.0.]

postsynaptic neuron leads to a strengthening of the synaptic strength $\Delta\omega > 0$, whereas neural activity that occurs in the postsynaptic cell before the presynaptic cell leads to a weakening of the synapse $\Delta\omega < 0$. The time difference between the respective spikes may not exceed ±40-80 ms when attempting to achieve a change in the synaptic weight [12].

3.3.4 Memristive Devices as Artificial Synapses

Memristive devices are suitable for the replication of synaptic plasticity due to their resistance malleability, which is achieved by applying a voltage (current) (cf. Sec. 2.1) [15]. This memristive plasticity for the emulation of biological synaptic behavior has already been demonstrated in a number of publications [12, 15, 53–55]. In particular, the voltage-controlled memristor model discussed in Sec. 2.1.1.1, which is described by Eqs. 2.3 and 2.4, was used in the work of Zamarreno-Ramos *et al.* [12] to establish a direct link to the synaptic weight growth of a biological synapse [15]:

$$\frac{d\omega}{dt} = \frac{dx}{dt} = F(x(t), \Delta t, \Delta V) \tag{3.4}$$

Here, the rate of change of the synaptic weight $d\omega/dt$ regulates the potency of the biological synapse, while the rate of change dx/dt controls the efficacy of the memristive device. The synaptic weight ω, as well as the state variable x, are conceived to be non-volatile, but both can be influenced by spikes, namely action potentials or current/voltage pulses, respectively. In this regard, the spike parameters, such as pulse duration Δt and pulse amplitude ΔV, are important. In particular, the amplitude is defined by the pre- and postsynaptic membrane potential as $\Delta V = V_{post} - V_{pre}$. In addition, the pulse frequency f_p plays an important part in the modification of the growth of the synaptic weight [15].

Jo *et al.* [53] used an Ag/Si-based memristive device as an artificial synapse to demonstrate STDP. The application of potentiation or depression voltage pulse trains to a device with the same pulse width Δt but with different polarities caused a decrease or increase in the resistance state of the device. In order to further emphasize the influence of pulse width, further pulse trains were applied to the same device, this time with different pulse widths Δt. It was found that a longer pulse width leads to a greater change in the resistance value; this applies to both negative and positive pulses [53].

Ohno *et al.* [147] were able to demonstrate both short-term memory and long-term memory using an Ag/Ag_2S/nanogap/Pt synaptic device. They applied voltage pulse trains with different frequencies f_p to their device. The authors found that a pulse train of a low frequency causes little or no change in the resistance value of the device; however, applying pulses of a high frequency was found to lead to a decrease in the resistance state of the device [148].

Zamarreno-Ramos *et al.* [12] demonstrated an implementation of a memristor-based STDP learning rule using suitable voltage pulse schemes. Voltage pulse trains were applied to the electrodes of a synaptic device; it was found that different spike shapes and widths resulted in the memristor STDP weight function demonstrating significant variance in its course $\xi(\Delta T)$ (cf. Sec. 3.3.3) [12, 61].

3.4 Spiking Neuron Models

In 1939, Hodgkin and Huxley succeeded in measuring an action potential in the giant axon of a squid [149]. Years later, they used electronic equivalent circuit models to emulate the dynamics of action potential generation [10, 135]. In general, detailed conductance-based neuron models emulate the electrophysiological characteristics that are necessary when shaping an action potential [10]. However, these models are more difficult to analyze than phenomenological spiking neuron models because they are more intrinsically complex. Thus, phenomenological spiking neuron models are of particular interest in the study of memory, neural coding, and the dynamics of networks, because they allow for the analysis of these properties in a plain electrical circuit [9, 10, 150–153].

An excellent overview of spiking neuron models is given by Gerstner and Kistler [9] and Gerstner *et al.* [138] in the books "*Spiking Neuron Models: Single Neurons, Populations, Plasticity*" and "*Neuronal Dynamics: From Single Neurons to Networks and Models of Cognition*", respectively. The overviews of spiking neuron models provided in this section and in Sec. 3.6 are based on these publications [9, 138].

3.4.1 Leaky Integrate-and-Fire Model

The leaky integrate-and-fire neuron model is a simplified phenomenological spiking neuron model that describes the generation of an action potential by a threshold criterion: the sum of the input signals reaches a certain threshold θ [9]. The circuit set-up of a leaky integrate-and-fire model consists of a parallel connection between a capacitor C and a resistor R with a constant voltage source u_{rest}, in series, as shown in Fig. 3.6. A constant input current I is applied to the circuit, which leads to the following equation [9]:

$$\tau_m \frac{du(t)}{dt} = -(u(t) - u_{rest}) + RI(t) \tag{3.5}$$

Here, the membrane potential is determined by *u(t)*, the reset potential by u_{rest}, and the time constant of the circuit by $\tau_m = RC$ [9].

The integrate-and-fire model emulates spikes as particular incidents,

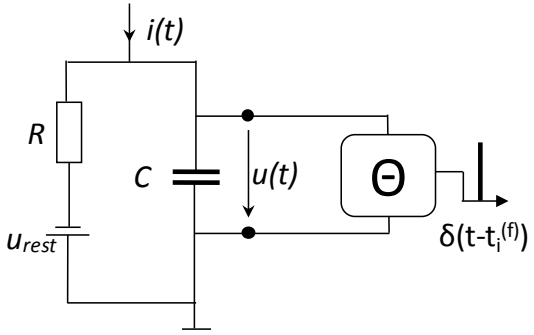

Figure 3.6 Sketch of a leaky integrate-and-fire neuron model. The circuit consists of a parallel connection between a capacitor C and a resistor R with a constant voltage source u_{rest}, in series. If the voltage u of the parallel connection reaches the threshold θ at $t_i^{(f)}$, a fire pulse is induced [9]. [Adapted with permission from [9].]

rather than as a pronounced conductance-based voltage course similar to that of an action potential shape. Therefore, the relevant parameter for the emulated spikes is the firing time $t^{(f)}$, which is determined by the following threshold criterion [9]:

$$t^{(f)} : u(t^{(f)}) = \theta \tag{3.6}$$

An electronic threshold subcircuit enables the firing by constantly comparing the membrane potential $u(t)$ with the threshold θ. After reaching the threshold θ at the fire time $t^{(f)}$, the membrane potential is reversed to the reset potential $u_{rest} < \theta$ [9].

A constant input stimulus I_0 is applied to the RC network of the leaky integrate-and-fire neuron, assuming a reset potential of $u_{rest} = 0$. In order to eliminate membrane potential *u(t)*, Eq. 3.5 must be integrated. This leads to the description of *u(t)* as a function of the input current I_0, with a preceding spike at $t^{(1)}$ [9]:

$$u(t) = RI_0 \left[1 - \exp\left(-\frac{t - t^{(1)}}{\tau_m} \right) \right] \tag{3.7}$$

Using the threshold criterion from Eq. 3.6 at the firing time $t^{(2)}$, the threshold can be described as follows [9]:

$$\theta = RI_0 \left[1 - \exp\left(-\frac{t^{(2)} - t^{(1)}}{\tau_m}) \right) \right] \tag{3.8}$$

This results in a regular firing rate, with the period $T = t^{(2)} - t^{(1)}$ depending on a constant input stimulus I_0 [9]:

$$T = \tau_m \ln \left(\frac{R\ I_0}{R\ I_0 - \theta} \right) \tag{3.9}$$

The one-dimensional leaky integrate-and-fire model offers many advantages, such as a straightforward implementation and compactness. However, the simplicity of this model means that it is unsuitable for reproducing the diversity of the firing patterns of real neurons [138].

3.4.2 Adaptive Exponential Integrate-and-Fire Model

A two-dimensional spiking neuron model is necessary to emulate all of the measured firing patterns of real neurons on a descriptive level. Thus, the general nonlinear integrate-and-fire model (cf. Sec. 3.4.1) that describes the dynamics of membrane potential is linked to the abstract adaptation current variables ω_k. The dynamics of each adaptation current ω_k are characterized by a first-order differential equation [138]:

$$\tau_m \frac{du}{dt} = f(u) - R \sum_k \omega_k + R\ I(t) \tag{3.10}$$

$$\tau_k \frac{d\omega_k}{dt} = a_k(u - u_{rest}) - \omega_k + b_k \tau_k \sum_{t^{(f)}} \delta(t - t^{(f)}) \tag{3.11}$$

Here, the parameter a_k constitutes the link between the membrane voltage u and the adaptation currents ω_k. The coupling develops with the adaptation time constant τ_k [138]. The δ-function is implemented in order to give the firing of the model an additional weighting. This causes the rate of change of the adaptation currents $d\omega_k/dt$ to rise by the constant b_k after each reaches the threshold value θ. Thus, the value

b_k indicates a leap for the adaptation, which depends on the number of spikes generated. The resistor R establishes the connection between the abstract adaptation currents ω_k and the temporally varying membrane potential u [138].

Depending on the desired result, the nonlinearity $f(u)$ in Eq. 3.10 can be selected in a variety of ways. A desired result with emphasis on the best fit performance to the experimental values can be achieved using the exponential integrate-and-fire model [138]. Thus, the adaptive exponential integrate-and-fire model, also called AdEx, can be described using the following set of equations [138]:

$$\tau_m \frac{du}{dt} = -(u - u_{rest}) + \Delta_T \ \exp\left(\frac{u-\theta}{\Delta_T}\right) - R\omega + R\ I(t) \tag{3.12}$$

$$\tau_\omega \frac{d\omega}{dt} = a(u - u_{rest}) - \omega + b\tau_\omega \sum_{t^{(f)}} \delta(t - t^{(f)}) \tag{3.13}$$

Here, the parameter Δ_T specifies the intensity of the influence of the exponential function, also referred to as the sharpness variable [138]. The fulfillment of the threshold criterion (cf. Eq. 3.6) leads a resetting of the membrane potential $u = u_{rest}$. In general, the intensity of adaptation and thus the firing patterns are determined by the variables a and b [138].

The adaptive exponential integrate-and-fire model can emulate all of the previously measured firing patterns of biological neurons on a phenomenological level [138].

3.4.2.1 Izhikevich Neuron Model

The Izhikevich model exploits the quadratic integrate-and-fire model to account for the nonlinearity $f(u)$ in Eq. 3.10, which leads to the following first-order differential equations [138]:

$$\tau_m \frac{du}{dt} = -(u - u_{rest})(u - \theta) - R\omega + R\ I(t) \tag{3.14}$$

$$\tau_\omega \frac{d\omega_k}{dt} = a(u - u_{rest}) - \omega + b\tau_\omega \sum_{t^{(f)}} \delta(t - t^{(f)}) \tag{3.15}$$

The Izhikevich model has many properties that are consistent with the AdEx model, such as the quality of spike generation and the variety of possible spike patterns. However, the Izhikevich model offers a less accurate representation of real spiking patterns [154].

3.4.2.2 Leaky Integrate-and-Fire Model with Adaptation

The leaky integrate-and-fire model (cf. Sec. 3.4.1) is extended by adaptation currents ω_k, which leads to the following set of first-order differential equation [138]:

$$\tau_m \frac{du}{dt} = -(u - u_{rest}) - R \sum_k \omega_k + R\ I(t) \tag{3.16}$$

$$\tau_k \frac{d\omega_k}{dt} = a\ (u - u_{rest}) - \omega_k + b_k \tau_k \sum_{t^{(f)}} \delta(t - t^{(f)}) \tag{3.17}$$

This model causes a further quantitative decrease in the description of spike patterns of real neurons due to a missing exponential activation term (AdEx) or a quadratic function (Izhikevich). However, the simplified term enables a straightforward experimental realization [138, 154].

3.5 Memristive Spiking Neuron Model

A memristive spiking neuron model was developed and experimentally implemented. The set-up of the implemented circuit is illustrated in Fig. 3.8(a). The integrator part of the circuit is highlighted with a blue square, in which a memcapacitor C_M (cf. Sec. 2.2.1) is in parallel with a negative differential resistor R_{NDR} and a constant voltage source V_B. In order to better understand the function of the memcapacitor, the circuit from Fig. 3.7 should first be considered, which apart from the memcapacitor represents an equivalent to the leaky integrate-and-fire model from Fig. 3.6. Thus, according to Eq. 3.5, the integrator can be described as follows [9, 10]:

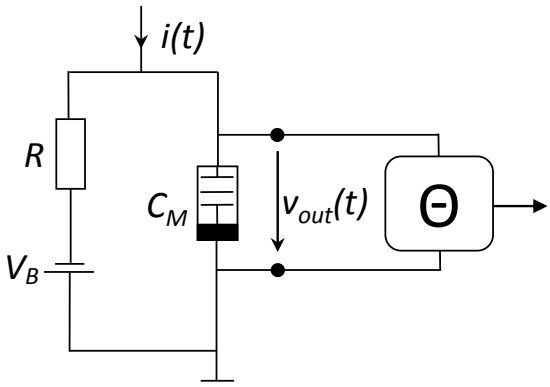

Figure 3.7 An adaptation of the leaky integrate-and-fire model from Fig. 3.6 is provided by replacing the constant capacitance C with a memcapacitor C_M (cf. Sec. 2.2.1) [10]. [Adapted from [10] / CC BY 4.0.]

$$\tau_m \frac{dv_{out}(t)}{dt} = -f(v) + RI(t) \tag{3.18}$$

$$with \quad f(v) = v_{out}(t) - V_B \tag{3.19}$$

However, the time constant $\tau_m = RC_M(\omega)$ is not constant; rather, it depends on the latest state $\omega(t)$ of the memristive device within the memcapacitor subcircuit (cf. Sec. 2.2.1). This results in a change of the voltage growth depending on the state of the memristive device [10, 155]:

$$\frac{dv_{out}(t)}{dt} = \frac{1}{RC_M(\omega)} f(v) + \frac{1}{C_M(\omega)} I(t) \tag{3.20}$$

$$with \quad \frac{d\omega(t)}{dt} = \beta\omega(t)I(t) \tag{3.21}$$

Here, the device-specific constant is defined as β. The rate of change of the state $d\omega(t)/dt$ depends on the number of preceding generated spikes quantified in the state $\omega(t)$ and current $I(t)$ as a function of time t. Thus, the state of the memcapacitor directly influences the time constant τ_m, which in turn adapts the firing rate of the circuit. The frequency change occurs as a result to the modifications of the integration time [10, 155].

The threshold value θ realized in the LIF model through the use of an external circuit was achieved in the memristive spiking neuron model (cf. Fig. 3.8(a)) using a negative differential resistor R_{NDR}. This changes Eq. (3.20) as follows [10, 155]:

$$\frac{dv_{out}(t)}{dt} = \frac{1}{R_{NDR}C_M(\omega)}f(v) + \frac{1}{C_M(\omega)}I(t) \tag{3.22}$$

The input stimulus I initially charges the memcapacitor C_M with the time constant $\tau = C_M(\omega)R_{NDR}$, while the resistance state of the NDR is defined by the high ohmic branch (cf. Fig. 3.9). When the internal threshold value θ of the NDR is reached by the constant input current I, there is a transition from the high ohmic branch (R_{VO2} = 55 kΩ) to the low ohmic branch (R_{VO2} = 2-14 kΩ). This leads to a voltage breakdown of the output voltage v_{out} and to a discharge of the memcapacitor. Thus, a constant current input I leads to an oscillation at the output due to the back-and-forth transfer of energy between the integrator branches. It is worth mentioning that the input current must be greater than the threshold current I_θ of the NDR, which becomes apparent later in the evaluation of fire frequency coding (cf. Sec. 3.5.2.1) [10].

An output branch modifies a desired line shape, represented by v_{spike} from the output voltage v_{out} (the orange box in Fig. 3.8(a)). The branch consists of a voltage divider R_1 and R_2 in series with a commercial diode D. The spike course v_{spike} is detected across R_2, and it is shown with the output voltage v_{out} for a constant current $i(t) = I_0$ in Fig. 3.8(b). The diode D with R_1 and R_2 forms a voltage divider. Thus, the resistance R_2 ($R_2 << R_D$) carries no weight whenever the build-in voltage of 0.7 V of the diode is not reached. Hence, the negative shift of v_{out}, including a positive voltage up to 0.7 V, is kept constant at the spike output v_{spike}. The duration of this holding is referred to as t_{rest}, which includes a refractory period (cf. Fig. 3.8(b)). A refractory period ensures the independent spiking of successive spikes. A spike is generated with a width of approximately 2 ms, whenever the output voltage v_{out} reaches the threshold of ~0.7 V. Furthermore, the voltage divider R_1 and R_2 reduces the spike output v_{spike} to a peak-to-peak amplitude in the

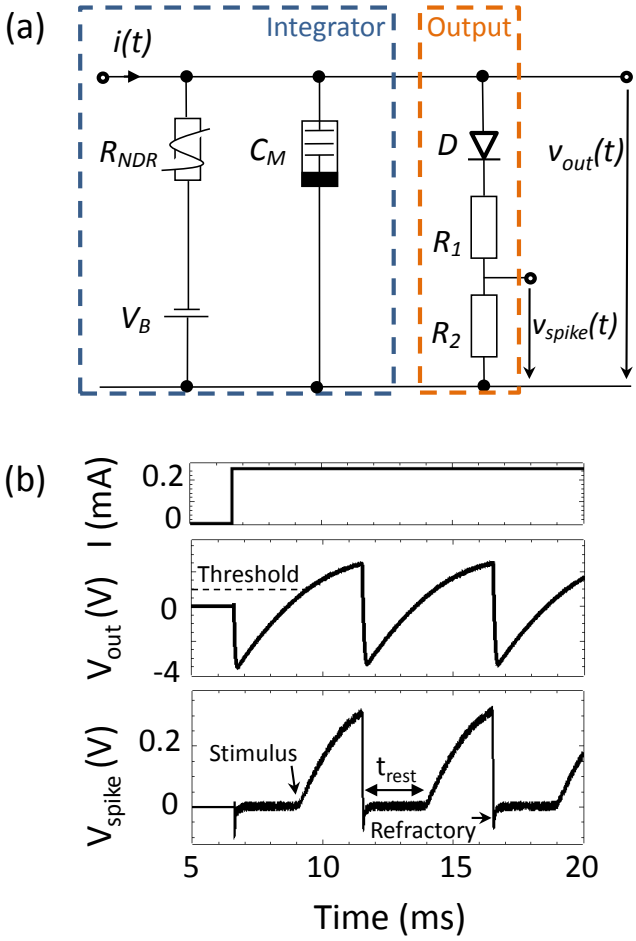

Figure 3.8 Memristive spiking neuron model to emulate neuronal functionality: (a) The integrator part consists of a memcapacitor C_M in parallel to an NDR and a constant source V_B. A biological spike line shape is achieved by an output branch with a diode D and a voltage divider. (b) A constant input current I_0 of 0.25 mA results in an oscillation at the output v_{out}. This oscillation is modified to a desired line shape represented by v_{spike} [10]. (cf. Ch. A) [Adapted from [10] / CC BY 4.0.]

low range of millivolts, which is comparable to biological spikes. In Fig. 3.8(b), spikes with an amplitude of 0.3 V and a resting potential of u_r= 3.5 mV, including a resting period of t_{rest} = 0.18 ms, were generated with the memristive spiking neuron circuit. It is worth mentioning that, on a descriptive level, the memristive spiking neuron circuit emulates voltage courses that are similar to those of biological spikes, rather than emulating spikes as particular events [10].

The key devices in the spiking circuit are the memcapacitor (cf. Sec. 2.2.1) and an NDR. For the NDR, the strongly correlated electron material VO_2 was used, which is discussed in more detail in the following section.

3.5.1 VO_2-based NDR

The memristive spiking neuron circuit (cf. Fig. 3.8) exploits a negative differential resistance from a current-controlled vanadium dioxide (VO_2) device [10]. The strongly correlated electron material vanadium dioxide can alternate between two different forms; changes between the forms occur as a result of external influences, such as pressure or temperature, and show a sharp metal-insulator phase transition (MIT) at the material-specific temperature of 60°C (cf. Fig. 3.9(a)): A temperature higher than 60°C leads to a conductive phase of the device, whereas temperatures below the material-specific 60°C results in an insulating character of VO_2 device [10, 11, 156–158].

A schematic of a lateral VO_2 device stack used for the memristive spiking neuron circuit (cf. Fig. 3.8) is depicted in the inset of Fig. 3.9(a) and was fabricated by A. Petraru from the chair of Nanoelectronics. The structure consists of the layer sequence TiO_2/VO_2/Au, wherein the two single Au contacts on top are separated by a material-specific distance of 2 - 4 µm and have a thickness of 40 nm. A pulsed laser deposition (PLD) technique was employed to deposit the strongly correlated electron material VO_2 on a TiO_2 crystalline substrate [10, 159]. The PLD process was accomplished utilizing a ceramic V_2O_5 target, maintaining a constant O_2 pressure of 10^{-2} mbar, while a constant temperature of 380°C was ensured. An energy density of the laser of 2.5 J/cm^2 was set at the target [10, 159].

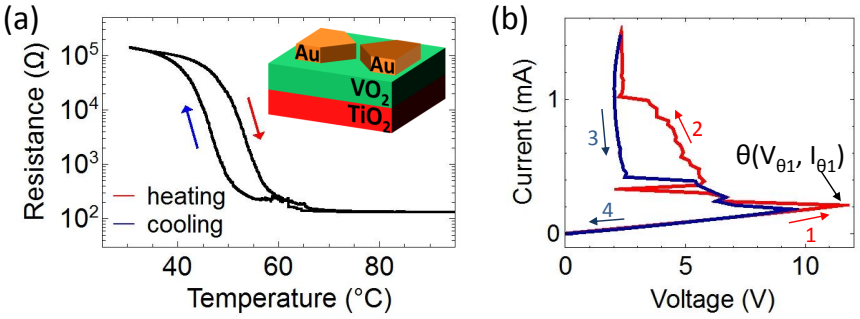

Figure 3.9 MIT transition of the VO_2 device used: (a) Resistance versus temperature characteristic. The inset shows the lateral VO_2 device stack. (b) Typical current voltage curve of the VO_2 device with the corresponding heating (red) and cooling (blue) phase. Arrows and numbers indicate the current sweep steps. A current source has been used for this measurement [10]. [Adapted from [10] / CC BY 4.0.]

A temperature-dependent resistance characteristic of the VO_2 device was measured. For this purpose, a constant voltage of 1 V was applied to the device, while the current changes were simultaneously recorded with rising (red arrow) or falling (blue arrow) temperature courses. The substrate temperature was linearly ramped up from 30°C to 95°C and back down to 30°C. The resistance change was determined from the abovementioned data. A representative resistance that depends on the temperature characteristic of the VO_2 is illustrated in Fig. 3.9(a). The heating phase, which is marked by a red arrow in Fig. 3.9(a), shows that a material-specific MIT transition was clearly observable at a temperature of 58°C, whereas the cooling phase showed a transition from metal to insulator at a temperature of 48°C, which resulted in an overall hysteresis of the heating and cooling curves. This hysteresis resulted from the inertia of the cooling system. The observed temperature was consistent with the values known for VO_2 devices. A change of the resistance state that exceeds four orders of magnitude is also an indicator of a good transition from metal to insulator and back to metal [10].

An alternative to the external heating of the device substrate is provided by electrical stress. Electrical stress causes Joule heating of the local filamentary grain structures within the VO_2 device, which leads to a change in resistance [10, 160, 161]. Pickett *et al.* [129] refer to a device that demonstrates MIT transitions as a result of electrical stress as a memristive device [10].

A typical measured current-voltage characteristic, where electrical stress was applied, is depicted in Fig. 3.9(b). The *I-V* characteristic was recorded at a substrate temperature below the material-critical temperature, i.e. at room temperature, at which the phase transition occurred. This ensured a phase transition within the current sweep, which was ramped from 0 to 1.5 mA and vice versa. Thus, an *I-V* characteristic with a negative differential region that depends on local, current-driven changes in the filament can be seen. More specifically, the NDR region is defined by an increase of the current, while the voltage decreases. The heating and cooling phases are marked by red and blue arrows, respectively [10].

The threshold of this particular device is defined by $\theta(V_{\theta 1}|I_{\theta 1}) = \theta(11.56\text{ V}|\ 0.21\text{ mA})$. Up to the threshold θ, the resistance of the device reads $R^H_{VO2} = 55k\Omega$. Exceeding the threshold resulted in a voltage breakdown, while the current was still increased by the current-sweep. The lower resistance was located between 2 kΩ and 27 kΩ depending on the input current ($R^L_{VO2} = 2\ k\Omega - 27\ k\Omega$) [10].

It is worth noting that a thermic formation step of the VO_2 device is necessary in order to achieve an NDR region via electrical stress. In the forming step, the device substrate is heated to a temperature that is sufficiently high that MIT transition should be observed, as mentioned previously. Thus, formation of a filament is ensured, thus providing conduction channels for the charge transport [10].

3.5.2 Results of the Memristive Spiking Neuron Circuit

The results of the memristive spiking neuron model are discussed in the following section. The discussion is divided into two sections: First, the behavior of the memristive circuit is determined on the basis of the spiking behavior as a function of the input signal; this is followed by an

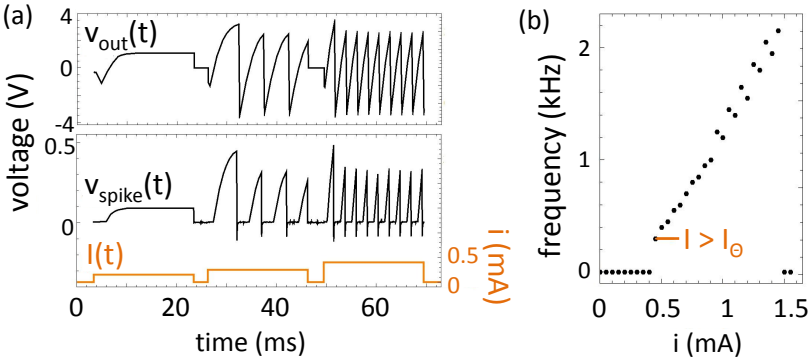

Figure 3.10 Fire frequency coding: (a) Intensity and duration of a stimulus are encoded in the number and frequency of spikes. (b) Fire frequency as a function of the input current. A stimulus above the threshold I_θ results in an oscillation. Frequency increases with an increased current. A jump of the frequency indicates a type II neuron model [10]. (cf. Ch. A) [Adapted from [10] / CC BY 4.0.]

explanation of frequency adaptation, which is demonstrated using the circuit [10].

3.5.2.1 Frequency Coding

The memristive spiking neuron circuit emulates frequency coding. For this purpose, the memcapacitor was kept constant in order to exclusively demonstrate the properties of frequency coding. Therefore, the memcapacitor shown in Fig. 3.8 was replaced by a commercial constant capacitor C_0. Input stimuli I with different intensities were applied to the spiking neuron circuit while the output voltage v_{out} and the spike output v_{spike} were measured (cf. Fig. 3.10(a)). As a result, the circuit emulated a spiking neuronal coding scheme, in which the number and frequency of the generated spikes were dependent on the intensity and duration of the input current [10].

To elaborate, an input current of 0.15 mA resulted in no oscillation at the output within the observed time frame because the threshold

current I_θ of the NDR was not exceeded (cf. Fig. 3.9(a)). However, the spiking circuit demonstrated a reaction in the form of an increased voltage, measured at v_{out} and v_{spike}. From a biological perspective, this reaction is comparable with the passive reaction of a neuron. A slightly deviation of the membrane potential from the resting potential occurs in a biological neuron due to a stimulus raising the membrane potential under the threshold (cf. Sec. 3.1.2) [10].

A constant current strength of 0.25 mA triggered the spiking circuit to generate spikes with a constant frequency of 200 Hz. The applied input current reached the NDR branch of the VO_2 device. Similarly, an output voltage was observed with an input current of 0.4 mA; the increase in the input current resulted in an increase of the frequency to 1 kHz [10].

This can be seen more clearly in the measured oscillation frequency as a function of the input current (cf. Fig. 3.10(b)). Therefore, single constant input current pulses with a fixed length of 20 ms and varying amplitudes were applied exclusively to the integrator circuit with a constant capacitance C_0 (cf. Fig. 3.8(a)). The current amplitude was increased in steps of 0.05 mA, ranging from 0 to 1.55 mA. As a result, the spiking circuit generated a diverse number of spikes per second, e.g. fire frequencies, depending on the input current applied. An input current lower than the threshold current $I < I_\theta$ (cf. Fig. 3.9) results in no oscillation at the output, while an input current above the threshold generates spikes of a certain frequency. When the threshold current is reached, the oscillator frequency jumps from 0 Hz to 250 Hz immediately, which corresponds to the behavior of a type II neuron. In particular, the frequency increases approximately linearly up to 1 mA with an increased current, at which point a direct assignment of the frequency to the intensity of the input stimulus is possible. This represents the results shown in Fig. 3.10(a). Starting with an input current of 1 mA, minor discrepancies from the linear frequency course could be observed. This can be explained by the partially jagged course of the *I-V* characteristic (cf. Fig. 3.9); as a consequence, the resistance value is jumping slightly. This is due to the Joule heating processes within the VO_2 device, which are not completely controllable [10].

An input stimulus starting with 1.5 mA no longer showed spike generation since the negative differential range was exceeded. Thus, the

interval of frequency coding depends on the length of the NDR region of the VO_2 device (Fig. 3.9), which, in this case, ranges from input currents between 0.45 mA to 1.45 mA [10]. The link between the frequency of the circuit-induced oscillation and the input current strength can be mathematically deduced using Eq. 3.9. Here, the frequency is linked to the input current by the resistance of the VO_2 device for the case $R = R_{VO2}(i,t)$. An increase in the current I lead to a decrease in the period T, which was electrically the result of a more rapid charging of the capacitor C_0 [10]. It is worth noting that the number of spikes generated also depends on the duration of the input pulse, as the number of additional spikes increases proportionally with the duration. However, this does not provide additional information with regard to the frequency [10].

3.5.2.2 Adaptation

The memristive spiking neuron circuit (cf. Fig. 3.8(a)) with the memcapacitor $C_M = C_M(t)$ (cf. Sec. 2.2.1) was used to emulate firing frequency adaptation, as first observed by E. D. Adrian in 1926 [4]. Applying a constant input current of $I = 0.5$ mA to the memristive spiking neuron circuit led to the measured voltage courses of $v_{out}(t)$ and $v_{spike}(t)$, as shown in Fig. 3.11. As a result, the frequency of the generated spikes noticeably decreased after the first eight spikes while a constant input current was applied. A decrease of the frequency from an initial high frequency of $f_0 \approx 400$ Hz to the final frequency $f_\infty \approx 140$ Hz occurred abruptly, whereas the spike amplitudes remained nearly constant. The transition from the initial frequency f_0 to the low frequency f_∞ can be seen more clearly in the enlargement of the two individual spikes v_{spike} with either a spike generated before the frequency transition (the black curve) or a spike generated after the transition (the red curve) (cf. Fig. 3.12(a)). Despite the spike width being reduced by approximately 50 percent, the amplitude of the spikes remained roughly constant at 0.36 V. Furthermore, the resting potential of both spikes remained constant at u_{rest} = -15 mV. The spike widths (3 ms $\rightarrow$ 6.1 ms) and the refractory periods (0.8 ms $\rightarrow$ 1.2 ms) changed significantly [10].

The changes in terms of the spike widths and the refractory periods can be explained with reference to the time constant τ_m. Here, according to Eq. 2.19, the time constant can be defined as τ_m =

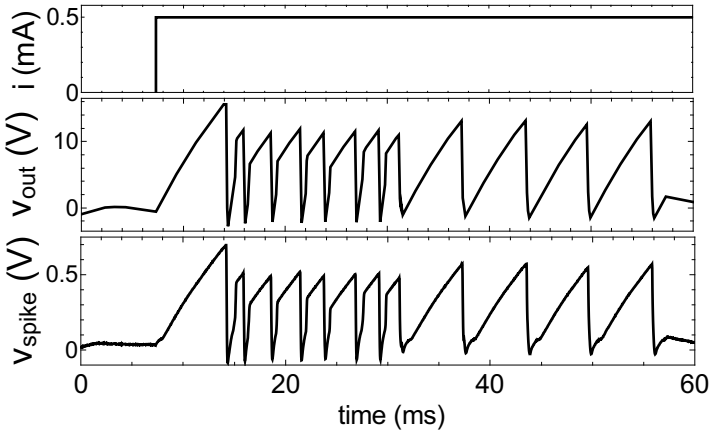

Figure 3.11 The memristive spiking neuron circuit from Fig. 3.8 was used to emulate frequency adaptation with a memcapacitor C_M. Spiking patterns of v_{spike} and v_{out} for a constant input current of $I = 0.5$ mA are recorded [10]. (cf. Ch. A) [Adapted from [10] / CC BY 4.0.]

$R_{VO2}(i,t)C_M(R_M,u_M,t)$ with the memconductance C_M. Whenever the resistance state R_M of the Ag/TiO_{2-x}/Al memristive device in the memcapacitor subcircuit (cf. Fig. 2.11) changed from HRS to LRS due to preceding spikes, the time constant $\tau_m = R_{VO2}(i,t)C_M(R_M,u_M,t)$ also increased. This was due to an overall increased capacitance of $C_M \approx C_1$. This can be seen in greater detail when considering the phase plots (Fig. 3.12(b)) of the two single spikes. The phase plots demonstrate the rate of voltage change of v_{spike} (Δv_{spike}) as a function of the spike voltage v_{spike} [10]. The phase plots of the two spikes differ slightly: however, a significant difference exists in the initial phases of the depolarization of the spikes. The enlargements of the initial phase of spike generation clarify that the first spikes with the frequency f_0 (the black curve in Fig. 3.12(a)), clearly rose more rapidly than the spikes after the frequency transition with f_∞ (the red curve) [10]. Naundorf *et al.* [162] identified this initial spike phenomenon in cortical neurons and described it as a significant property, which improves neuronal coding [10].

It is worth to mentioning that the abrupt change of the frequency

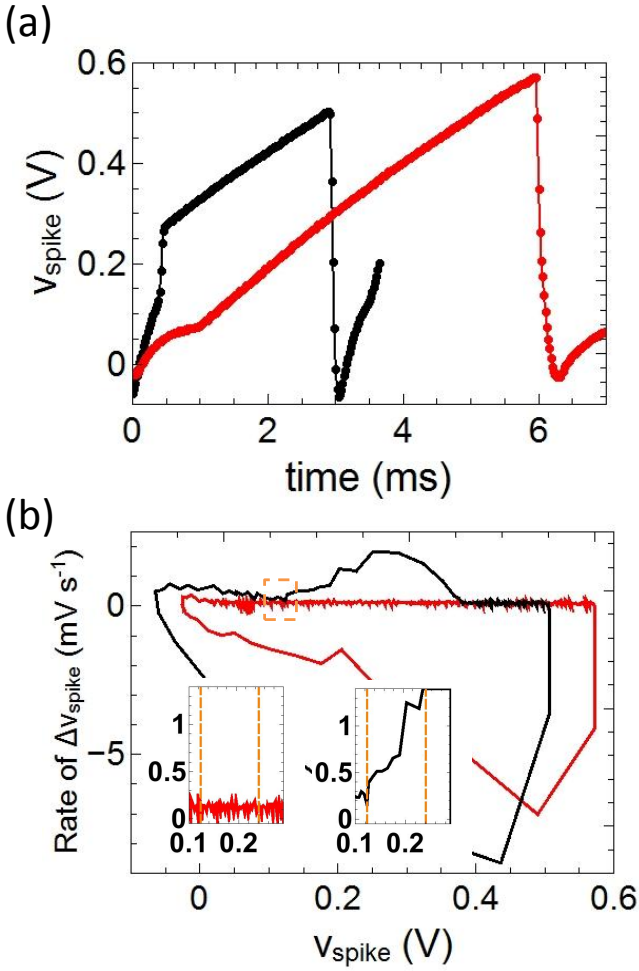

Figure 3.12 Characteristic of the spikes from Fig. 3.11: (a) Spikes before and after the frequency transition from high to low frequency and (b) the corresponding phase plot of the two spikes with initial phases highlighted in orange [10]. (cf. Ch. A) [Adapted from [10] / CC BY 4.0.]

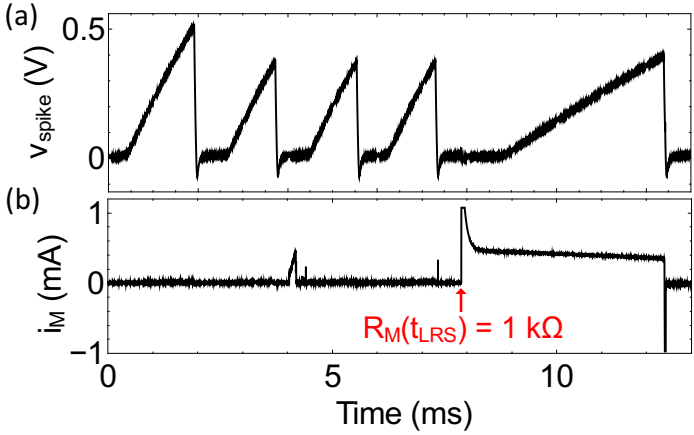

Figure 3.13 Characterization of the switching behavior: (a) The spike voltage v_{spike} of the neuron circuit. (b) Current flow through a Ag/TiO_{2-x}/Al memristive device during voltage oscillation. (cf. Ch. A)

change is inconsistent with the biology, where an adaptation process is observed as a continuous decrease of the frequency [10, 163]. The reason for the abrupt change is the switching mechanism of the used Ag-doped TiO_{2-x}-based memristive device since it changes the resistance state sudden. The use of a memristive device with a gradual resistance change would improve the emulation of biological properties. However, the used Ag/TiO_{2-x}/Al memristive device has an inherent stochastic nature, which is in agreement with biological neurons [10, 164]. The stochastic of the device is noticeable in the switching process, which results in a variation of the number of generated spikes before a frequency transition occurs. Furthermore, the pulse width of individual spikes (e.g. the third and fourth pulse in Fig. 3.11) is influenced by the memristive noise [10].

The behavior of the memristive device should be further analyzed. The current i_M through the Ag/TiO_{2-x}/Al memristive device is shown in Fig. 3.13, while frequency adaptation was recorded at the spike output v_{spike}. The current was measured with a shunt resistor $R_S = 1$ kΩ connected in

series to the memristive device R_M. A current of 6 µA was measured during the first four voltage spikes, which indicates a high resistance state of the memristive device. In the HRS, the memristive device has no influence on C_M and, according to Eq. 3.22, the frequency thus remains constant. However, an abrupt switching of the memristive device from the HRS to the LRS leads to an adaptation of the frequency and an increase of the current i_M at the time $t_{LRS} = 8$ ms [10].

3.6 FitzHugh-Nagumo Neuron Model

The transition from the experimentally realized memristive spiking neuron model to a more general experimental form of an oscillator is motivated by the theory of the FitzHugh-Nagumo neuron model and the van der Pol oscillator.

The FitzHugh-Nagumo model is a two-dimensional neuron model that represents an adaptation of the Hodgkin-Huxley model, which uses four variables in order to demonstrate sequences of spikes in pulse form [9]. The nonlinear integrate-and-fire model (cf. Sec. 3.4.1) represents the mathematical basis, with a general function F that depends on an effective variable ω and the rate of change of ω [9]:

$$\frac{du}{dt} = \frac{1}{\tau}\left[F(u,\omega) + R\ I\right] \tag{3.23}$$

$$\frac{d\omega}{dt} = \frac{1}{\tau_\omega} G(u,\omega) \tag{3.24}$$

Here, τ_ω is a time-constant parameter. The FitzHugh-Nagumo model determines the functions $F(u,\omega)$ and $G(u,\omega)$ using the following set of equations [9]:

$$F(u,\omega) = u - \frac{1}{3}u^3 - \omega \tag{3.25}$$

$$G(u,\omega) = b_0 + b_1 u - c\omega \tag{3.26}$$

Here, u and ω constitute the membrane potential and the limiting variable, respectively [9, 165, 166]. The functions F and G depend on ω in

the first order. Thus, the nonlinear behavior of the generated pulses is defined exclusively by u^3. Further adjustments are made by the variables b_0, c, and b_1. This model describes a relaxation oscillator [9,165,166].

Given the precondition that $b_0 = c = 0$, what follows is a particular application of the FitzHugh-Nagumo neuron model, which is also called the Bonhoeffer van der Pol model [9, 167]:

$$\frac{du}{dt} = \frac{1}{\tau}(u - \frac{1}{3}u^3 - \omega + R\ I) \tag{3.27}$$

$$\frac{d\omega}{dt} = \frac{b_1}{\tau_\omega}u \tag{3.28}$$

3.7 Van der Pol Oscillator

The term van der Pol oscillator originates from the first recorded observations of a nonlinear oscillation by the famous scientist Balthazar van der Pol [168, 169]. Van der Pol identified the sawtooth oscillations of a self-sustained triode oscillator [168, 169]. In general, a van der Pol oscillator is described by a second order homogeneous equation [169, 170]:

$$\ddot{x} + \mu\ (x^2 - 1)\ \dot{x} + x = 0, \qquad \mu\ \geq\ 0 \tag{3.29}$$

Here, the time-dependent dynamical variable is represented by x. In comparison to damped oscillators, the friction coefficient is not constant but depends on the amplitude. The parameter μ characterizes the nonlinearity of the system. Low values for μ lead to quasilinear oscillation behavior, whereas an increase in the value of μ leads to increased nonlinearity [155, 170].

A van der Pol oscillator with driving forces can be achieved by adding the function $A\cos(\omega t)$ to Eq. 3.29 [170]:

$$\ddot{x} + \mu\ (x^2 - 1)\ \dot{x} + x - A\cos(\omega t) = 0 \tag{3.30}$$

Here, the amplitude is referred to as A. In addition to the self-oscillation frequency μ, the periodic forcing angular frequency ω also appears

[155, 170].

The relationship between the FitzHugh-Nagumo model (cf. Sec. 3.6) and the van der Pol oscillator can be seen more clearly by applying the Liénard's transformation [155, 170]:

$$y = x - \frac{1}{3}x^3 - \frac{1}{\mu}\dot{x} \tag{3.31}$$

Applying Liénard's transformation to the van der Pol Eq. 3.29 produces a modified van der Pol equation, which allows direct links to Eqs. 3.27 and 3.28 of the FitzHugh-Nagumo system [155, 170]:

$$\frac{dx}{dt} = \mu(x - \frac{1}{3}x^3 - y) \tag{3.32}$$

$$\frac{dy}{dt} = \frac{1}{\mu}x \tag{3.33}$$

The term RI in Eq. 3.27 can be covered by the forced function $Acos(\omega t)$ of the forced van der Pol oscillator (cf. Eq. 3.30) [155, 170].

A self-sustained van der Pol oscillator based on a programmable unijunction transistor (PUT) was experimentally realized (Sec. 3.8).

3.8 PUT-based Van der Pol Oscillator Circuit

A self-sustained van der Pol oscillator circuit based on a commercial programmable unijunction transistor (PUT [171–173]) was experimentally realized, as depicted in Fig. 3.14. A PUT resembles a four-layered thyristor device and thus belongs to the family of silicon-controlled rectifiers that have an NDR regime.The self-sustained oscillator circuit consists of a resistor-capacitor (RC) network at the anode side of the PUT, which constitutes the integrator part of the circuit, highlighted by a blue square. A voltage divider consisting of two linear resistors R_B and R_G comprises the gate side of the PUT [16, 73, 171–173]. The threshold θ of the circuit is comprised of the intrinsic constant threshold of the PUT of $V_{P\theta} \approx 0.6V$ and the potential at the gate terminal V_G, which is defined by the voltage divider. A constant voltage V_{BB} applied to the

oscillator circuit results in a charging of the capacitor C_{R1} with the time constant $\tau = R_1 C_{R1}$ [73]. The charging of the integrator subcircuit can be expressed using the following characteristic capacitor equation:

$$v_{C_{R1}}(t) = V_{BB}(1 - \exp\left(-\frac{t}{\tau}\right)) \tag{3.34}$$

If the capacitor voltage $V_C = V_A$ reaches the threshold V_θ of the PUT modified by the threshold circuit ($V_A = V_\theta \geq V_{P\theta} + V_G$), the PUT switches from the initial HRS to the LRS. This leads to a sudden capacitor discharge via the PUT to ground, which can be observed as an oscillation at the anode V_A and a voltage breakdown of the gate voltage V_G in the shape of a rectangular pulse at the gate side (cf. Fig. 3.14(b)). The oscillation at the anode V_A takes the form of sawtooth relaxation oscillation, while, at the gate voltage V_G, modifiable peaks are generated, representing the discharging of the capacitor C_{R1}. Both voltages V_A and V_G exhibit the same frequency and phase in a single oscillator.

In general, the adjusted threshold voltage V_θ must be attainable by the capacitor voltage V_A in order to demonstrate oscillation [73]. The design of the self-sustained van der Pol oscillator circuit used to demonstrate frequency coding (cf. Sec. 3.8.2) is depicted in Fig. 3.14(c). The functionality corresponds to the circuit shown in Fig. 3.14(a), but nodes 1 and 2 were placed separately. Furthermore, the integrator circuit was driven by an input current $i(t)$, while a constant voltage V_K was applied to the voltage divider in order to define the circuit threshold V_θ [73].

It is worth mentioning that the circuit design represented in Fig. 3.14(a) cannot demonstrate frequency coding, since the anode V_A and the gate V_G voltage increase proportionally to each other with an increased input voltage V_{BB}. Nonetheless, the oscillator circuit of Fig. 3.14(a) was implemented in Ch. 4, as the circuit required fewer power sources and the focus in the following chapter lies on pulse coupling, rather than on frequency coding [73].

The following sections discuss the PUT-based van der Pol oscillator circuit extensively. First, the PUT is discussed in detail; thereafter, the circuit performance is considered. The van Pol oscillator circuit emulates frequency coding and frequency adaptation.

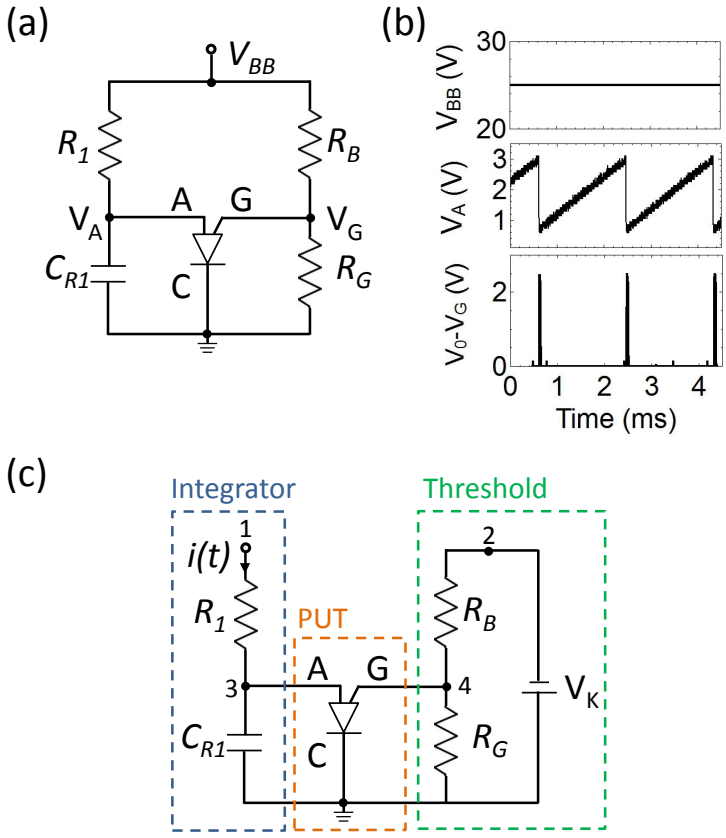

Figure 3.14 Relaxation Oscillator: (a) Basic circuit set-up of a relaxation oscillator to emulate spike generation based on a PUT. The anode (A), the gate (G), and the cathode (C) of the PUT are connected to the peripheral circuit environment. (b) A constant input voltage V_{BB} of 25 V results in a relaxation oscillation at the anode V_A and modifiable peaks at the gate potential V_G. (c) Circuit design used to emulate frequency coding. (cf. Ch. A) [Based on [16, 173].]

3.8.1 PUT-based NDR

A programmable unijunction transistor (PUT 2N6027 [171–173]) is classified as a silicon rectifier, which consists of several pn-junctions. To elaborate, PUTs consists of a pnpn configuration with three external terminals, namely the anode (A), the cathode (C), and the gate (G), as depicted in Fig. 3.15(a). The four-layer structure can be divided into pnp and npn regions. The operating principle of a PUT is best demonstrated by a simplified circuit, as depicted in Fig. 3.15(b) [171–173]. Therefore, the current I_A was swept from 0 to 1 mA and back, while the voltage at the anode V_{AC} was measured simultaneously. As a result, current-voltage curves (cf. Fig. 3.15(c)) with negative differential resistance (NDR) areas were measured for different constant voltages: $V_B = 2$ V, 4 V, 6 V. Thus, programming is possible via the adjustment of the NDR threshold voltage V_θ by varying the potential V_G at the gate terminal. The interleaving of the middle np-region significantly contributes to the NDR character of the device, which is controlled by the gate terminal (cf. Fig. 3.15(a)). The length of the NDR region increases with an increased voltage V_B, which is of particular interest for fire-rate coding, as the interval of frequency coding depends on the NDR region (cf. Sec. 3.8.2) [16, 73, 171–173].

3.8.2 PUT-based Frequency Coding

The relaxation oscillator circuit (cf. Fig. 3.16(a)) emulates frequency coding, as shown in Fig. 3.16(b). Therefore, three different input current intensities $I = 0.01$ mA, 0.3 mA, and 0.7 mA were applied to the circuit, while an oscillation was measured at the output with frequencies of 0 Hz, 1244 Hz, and 2834 Hz, respectively. Hence, the induced oscillation frequency varied as a function of the input intensity owing to the integrator RC-network. The threshold circuit (see the green frame in Fig. 3.16(a)) defines a constant threshold voltage V_G of the voltage divider; thus, the threshold of the circuit $V_\theta = V_{P\theta} + V_G$ is also constant. According to the following equation, the threshold criterion

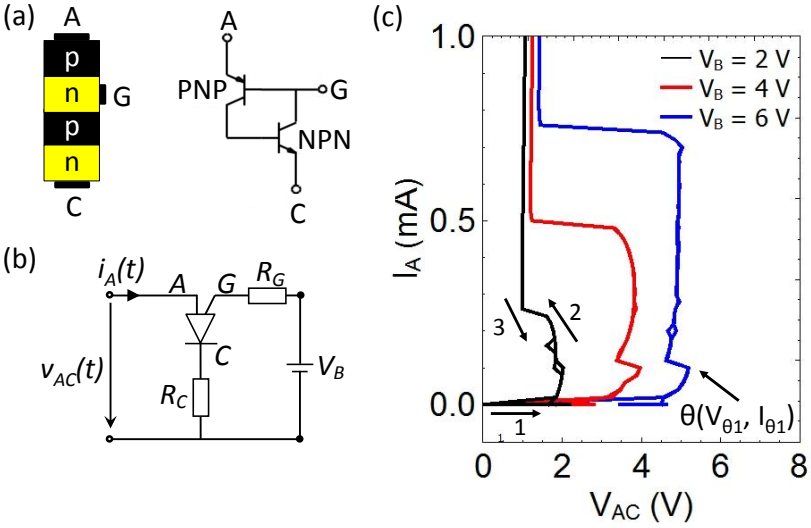

Figure 3.15 Programmable unijunction transistor: (a) Schematic of the internal pnpn-construction of the PUT and the corresponding electronic equivalent circuit. (b) Reduced circuit to demonstrate the influence of the gate voltage V_B on the negative differential area. (c) Current-voltage measurements for different voltages V_B. An increased gate voltage V_B results in an increased negative differential area. The $I-V$ curve was measured using a current source. (cf. Ch. A) [Based on [171, 173].]

$V_\theta = V_A$ is achieved more rapidly with an increased input current I:

$$V_A(t) = v_{C_{R1}}(t) = (R_1 I)(1 - \exp\left(-\frac{t}{\tau}\right)) \tag{3.35}$$

As a result, the frequency of the oscillation depends on the current intensity.

In order to study this point in greater detail, single constant current pulses with a width of 20 ms and with amplitudes ranging from 0 to 1.5 mA were applied to the relaxation oscillator. As a result, oscillations were generated after reaching the threshold $I > I_\theta = 0.01$ mA with different frequencies depending on the intensity of the input current (cf. Fig. 3.16(c)). These findings indicate a type II neuron model. The frequency increased linearly with an increased applied current, which established a direct dependency between the output frequency and the stimulus intensity within the meaning of frequency coding. Input currents below the threshold current I_θ and great than 1.4 mA generated no oscillation at the output because the working point was no longer within the NDR regime of the PUT.

The VO_2 device from Sec. 3.5.2.1 was replaced here by a PUT, because a more stable and reproducible behavior of the circuit performance and, consequently, of the emulation of frequency coding was achieved.

3.8.3 Memristive Van der Pol Oscillator Circuit

A memristive van der Pol oscillator circuit was investigated in the bachelor's thesis of S. Siegmund [174]. A memristive circuit exploiting an Ag/TiO_{2-x}/Al memristive device (cf. Sec. 2.1.4.1) is able to demonstrate frequency adaptation, as first observed by E. D. Adrian in 1926 [4, 10]. The circuit design of the memristive oscillator circuit is depicted in Fig. 3.17(a). The basis of the circuit forms the relaxation oscillator shown in Fig. 3.14(c). A high ohmic resistor R_P in parallel with the capacitor C_{R1} avoids charging of the capacitor at low currents. The subcircuit that is considerable relevance for the adaptation process is marked by a blue frame in Fig. 3.17(a). The subcircuit consists of a voltage divider with a linear resistor R_J and an Ag-doped TiO_{2-x}-based memristive device

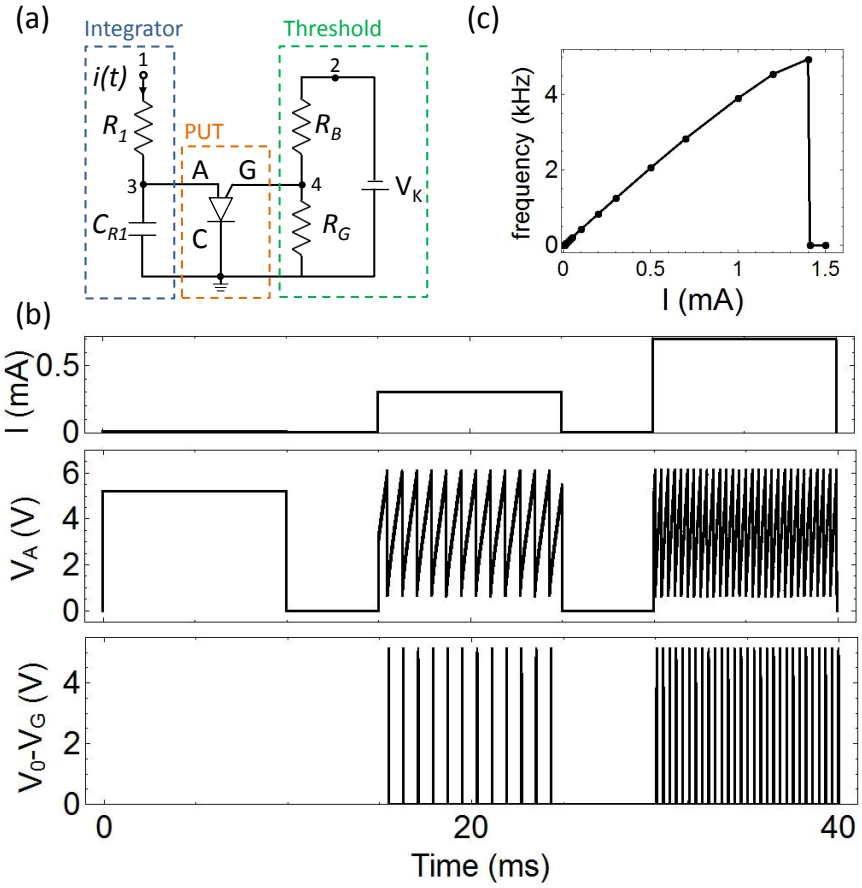

Figure 3.16 Fire frequency coding: (a) Circuit schematic to demonstrate frequency coding. (b) Generated spikes of the circuit as a result of different input intensities. Intensity and duration of an external stimulus is encoded in the number and frequency of spikes. (c) Oscillation frequency as a function of the input current I. An input stimulus above the threshold $I > I_\theta$ results in an oscillation. (cf. Ch. A) [Based on [10].]

R_M, and a linear resistor R_B connected in parallel to the voltage divider. The overall resistance R_T of the subcircuit and the gate resistance R_G influence the frequency of the oscillator circuit in such a manner that adaptation can be emulated. This can be seen more clearly in Fig. 3.17(b), where the voltage courses of the anode voltage V_A and the gate voltage V_G are shown for a constant input current of 15 μA. As a result, the frequency decreased from an initial frequency of $f_0 = 280$ Hz to a final frequency of $f_\infty = 170$ Hz after 60 ms. The adjustment in terms of frequency can be directly related to the resistance state of the memristive device [174].

In the beginning, the memristive device is in its HRS; thus, the overall resistance is defined by $R_B \approx R_T$ with $R_M = 1$ MΩ. This leads to the initial frequency f_0 due to the threshold voltage of $V_\theta = V_G + 0.6$ V $= 1.8$ V. A switch of the memristive device to the LRS occurs due to applied voltage pulses with an amplitude of $V_{R_B} \approx V_{R_M} = V_K - V_G = 1.2\ V$, assuming that $R_J \ll R_M$. The resistance of the memristive device in the LRS is $R_M \approx 1$ kΩ. This leads to a decrease from $R_T = 33$ kΩ in the HRS of the memristive device to $R_T = 13.55$ kΩ, corresponding to the LRS of the device. The corresponding shift of the oscillator threshold V_θ results in a decreased frequency, which is the basis of frequency adaptation. The switch occurs abruptly due to the digital switching characteristic of the memristive device [174].

In addition to the change in the frequency, the switching of the memristive device caused changes in the amplitude of the anode voltage and in the amplitude of the gate pulses, which are clearly visible in Fig. 3.17(b). However, this stands in conflict with the measured values of a biological neuron, the amplitude of which remains the same after frequency adaptation. The memristive spiking neuron model (cf. Sec. 3.5) demonstrates an almost constant amplitude of the spike output voltage v_{spike}, even after frequency adaptation as shown in Fig. 3.11, which is in good agreement with biology.

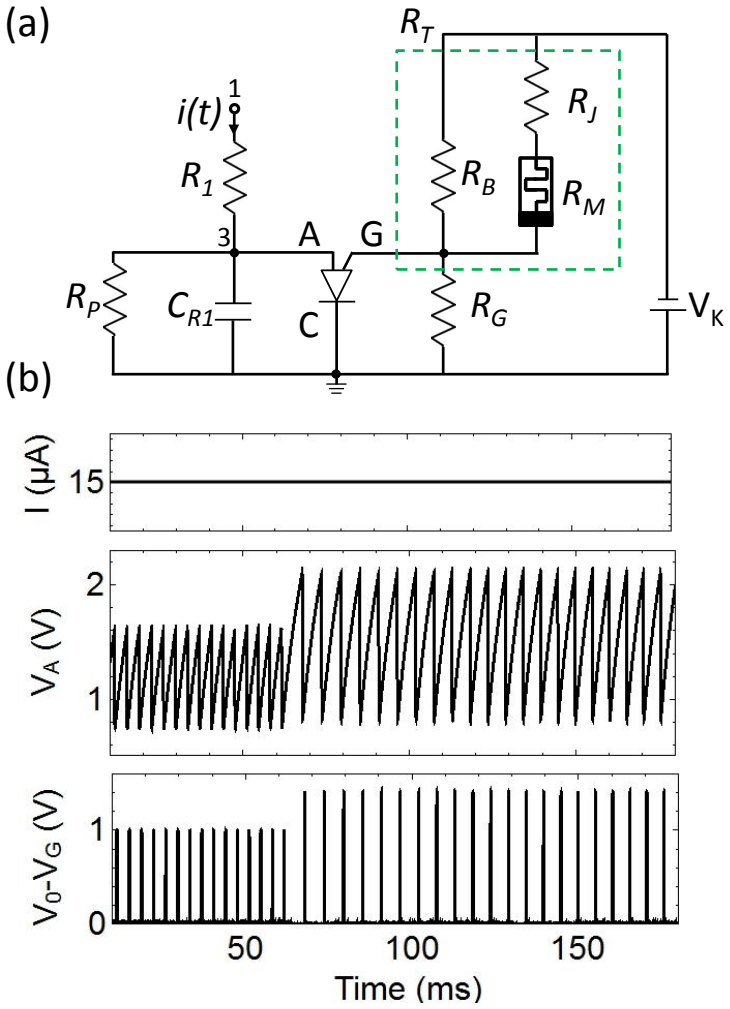

Figure 3.17 Experimental implementation of a memristive neuronal oscillator circuit: (a) Schematic of the investigated circuit. (b) Measured spike pattern with adaptation for a constant input current based on a memristive device. (cf. Ch. A) [Adapted from [10, 174].]

4 Dynamics and Topology

Thousands of fireflies flash in perfect harmony, a consistent applause sounds after a concert, two pendulum clocks on a wooden beam run evenly, and unified light pulses are generated by a laser: These phenomena have one thing in common, namely the mathematical description [175,176]. To elaborate, these events demonstrate the synchronization of self-sustained oscillators, as first observed by chance by Christiaan Huygens, when he contemplated weakly coupled pendulum clocks in 1665 [16, 73, 176, 177]. Synchronization is classically defined by a weak coupling, which adapts the frequencies of self-sustained oscillators. A self-sustained oscillator is characterized by a periodic motion that results from a non-rhythmic internal power source [176]. Its oscillation converts against a limited cycle according to a compensation between dissipation and energy flow [176].

The brain is the most interesting environment in which synchronization has been observed. Here, synchronization is attributed to various higher cognitive functionalities, such as information-processing within the whole brain [3, 16]. These brain areas are context-dependent, self-organized, and transient subsystems that are defined in the case of the visual system by the diverse but associated attributes of a visual object. This leads to the essential question concerned with binding these attributes to a homogeneous perception, which is also known as the "binding problem" [16]. It is assumed that neuronal synchronization is the most likely solution to the binding problem, as it may function to encode various features, such as color, shape, and motion, to a coherent transient state by means of neuronal dynamics in connection with the topology of neuronal networks [16].

Artificial neural networks (ANN) are used in the field of neuromorphic engineering to emulate brain activities. Electrical neuromorphic circuits should include important phenomena associated with biological computation, such as neuronal synchronization, natural oscillation, and memory [16, 73]. Synchronization and self-sustained oscillators are

classified in the field of nonlinear dynamics and enable the modeling of complex dynamic procedures, rather than simple static condition [176]. The memory process can be handled by memristive devices due to the ability of such devices to emulate the plasticity of functionalities such as STDP including Hebb's learning rule [16, 56, 58, 73, 178, 179].

In this chapter, coupled oscillator networks are introduced. First, the relevant terminology is explained (Sec. 4.1); this is followed by a detailed discussion of memristively coupled van der Pol oscillators in Sec. 4.2. Device-specific digital (Sec. 4.2.1) and analogue (Sec. 4.2.2) coupling is also discussed. Finally, a memristive network, which is capable of addressing the binding problem, is presented (cf. Sec. 4.3). Therefore, the intermediate between dynamics and plasticity is examined in a network topology.

4.1 Coupled Oscillator Networks

In order to better understand and investigate synchronization processes, coupled oscillators are used; this is due to their dynamic properties [175, 176]. Therefore, the phase-locking and frequency synchronization properties of pulse-coupled self-sustained oscillators mean that they enjoy widespread popularity in various scientific fields [180].

An excellent overview of synchronization is provided by Pikovsky *et al.* [176] in the book "*Synchronization: A Universal Concept in Nonlinear Sciences*"; the overview of terms that are important to this thesis presented in this section is based on this publication [176].

4.1.1 Periodic Self-sustained Oscillator

A self-sustained oscillator uses energy from an internal source to provide a steady oscillation, which classifies such an oscillator as an active system. The internal energy source works against the internal energy dissipation to keep the periodic motion constant. The self-sustained oscillator produces an oscillation with a consistent rhythm provided that the internal power source persists and assuming that there is no external influence. Such a system's autonomy is demonstrated by the fact that there is no external

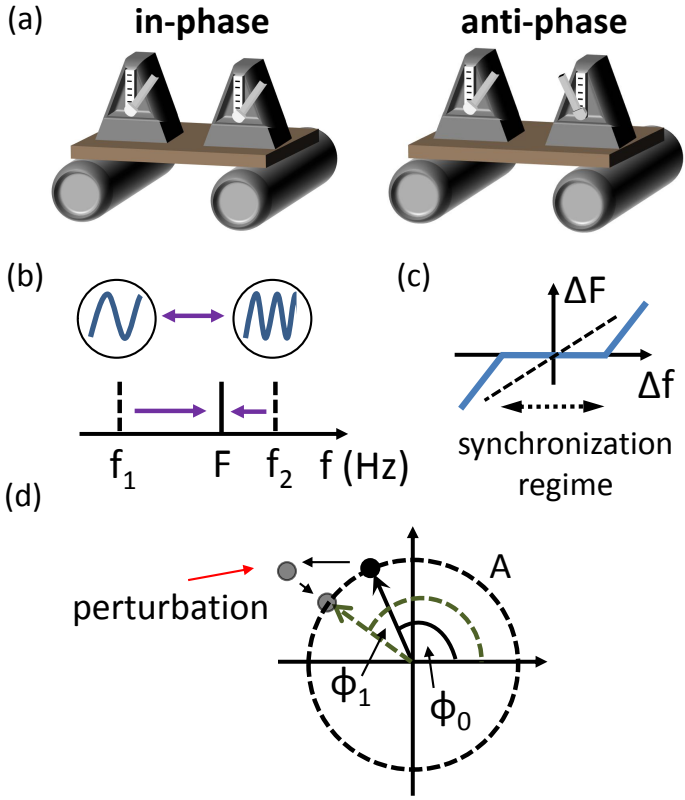

Figure 4.1 Coupled oscillators: (a) Two metronomes sitting on a light board lying on two cans, which demonstrate two phase synchronization regimes: in-phase and anti-phase synchronization. [Based on [176, 181].] (b) Mutual coupling of two oscillators with the natural frequencies f_1 and f_2 results in a common frequency F due to synchronization [176]. (c) The discrepancy between the frequencies ΔF of coupled self-sustained oscillators as a function of the corresponding difference of the natural frequencies Δf with a synchronization region. The dashed line indicates two coupled oscillators, which have no synchronization region due to a too high frequency detuning [176]. (d) Limit cycle of a self-sustained oscillator. Perturbation leads to a persistent jump of the phase from ϕ_0 to ϕ_1 on the limit cycle with a re-emerging amplitude A [176]. [Adapted with permission from [176].]

influence; for example, the external parameter time t, including the initial time t_0, has no influence on the dynamical oscillator system [176].

The intrinsic parameters of a self-sustained oscillator exclusively define the oscillation behavior, thus ensuring independence from a transient initial behavior. The circuit-induced oscillation of a self-sustained oscillator remains regular even after small perturbation [176].

The rhythm of a self-sustained periodic oscillator is defined by intrinsic parameters; thus, the majority of different oscillation behaviors can be observed, such as waveforms (which are quasilinear), sawtooths, or pulses (which are strongly nonlinear). The rhythm of a self-sustained periodic oscillation is determined by a temporal repetition of the oscillation form after a period T. The inverse of the period constitutes the number of generated spikes within a certain time interval and is referred to as the oscillation frequency [176]:

$$f = \frac{1}{T} \tag{4.1}$$

The angular frequency is commonly used to describe oscillation [176]:

$$\omega = 2\pi f = \frac{2\pi}{T} \tag{4.2}$$

The natural frequency of a self-sustained oscillator occurs when it is free of external influences in its autonomous system. The frequency of a self-sustained oscillator is usually described with a capital letter F when the oscillator is in a coupled system [176].

Beyond the frequency, the phase of an oscillator is of particular interest in the theoretical investigation of self-sustained oscillators since it defines where exactly the oscillation movement is in the periodic cycle and because the phase is not rigid. In general, the phase can be determined using the following equation [176]:

$$\phi(t) = \omega_0 t + \phi_0 \tag{4.3}$$

with the angular frequency $\omega_0 = 2\pi/T$. The initial phase ϕ_0 is defined

once on the switch-on of the oscillator system, but it can change during oscillation if, for example, interference occurs. Equation 4.3 indicates that the phase grows indefinitely with time t, but, simultaneously, the phase defines the exact state of an oscillator system. This can be explained by the fact that the increase of the phase after a cycle is exactly defined, namely with 2π within the period T. Thus, two phases that deviate from each other within one oscillatory cycle by a multiple of 2π are classified as the same physical state [176].

The phase describes the state of an oscillation as an additional variable to the oscillation amplitude y. The amplitude alone cannot exclusively determine the state of a periodic oscillation, because, for example, in the case of a harmonic oscillation that occurs during an oscillation cycle, the same amplitude value is taken twice, but during different phases of the cycle. However, these two parameters are usually sufficient to identify all of the necessary states of an oscillator system. Therefore, they are plotted as a function of each other in a so-called phase portrait (cf. Fig. 4.1(d)). A resulting closed curve (limit cycle) in the phase portrait is the typical pattern of a repetitive periodic oscillation movement after a period T for each [176]. An external disturbance to the oscillator system can lead to a shift from the limit cycle in the corresponding phase portrait. However, if the external disturbance disappears, the self-sustained dynamical oscillator system will return to the limit cycle as long as there have been no changes in the intrinsic parameters of the oscillator. Thus, the limit cycle can be referred to as an attractor of the self-sustained oscillator since deviating progressions in the phase portrait always move back to the attractor cycle [176].

The disturbance causes a shift in the initial phase from ϕ_0 to ϕ_1, while the amplitude returns to its original amplitude value A after a deviation during the perturbation (cf. Fig. 4.1(d)). As a result, the free-running phase can be modified by the initial phase ϕ_0 without influencing the following oscillation. Thus it is possible to synchronize a self-sustained oscillator with a limit cycle, for example with another oscillator, by adjusting their phases to a common one, which is the basis of phase synchronization [176].

A self-sustained oscillator that exhibits a limit cycle is essentially a nonlinear autonomous system, rather than a linear harmonic oscillator system, in which oscillation dies out or is infinitely amplified. Thus, a self-sustained oscillator can be defined as a van der Pol oscillator (cf. Sec. 3.7) [176].

4.1.2 Mutual Synchronization

Two self-sustained oscillators with differing natural frequencies can reciprocally influence each other's rhythm assuming that a weak interaction originates from a mutual coupling [176]. A weak interaction occurs whenever extreme forms, such as a rigid or no coupling, are excluded. A weak interaction is quantified by the coupling strength, which determines to what extent the interaction occurs [176]. A sufficiently high coupling strength can lead to a complex dynamic process of synchronization with frequency locking and/or phase-locking of the two self-sustained oscillators. However, synchronization can only occur if both systems are not changed qualitatively in their most basic behaviors [176].

A frequency synchronization of two self-sustained oscillators is characterized by the fact that the natural frequencies f_1 and f_2 differ from each other in the uncoupled state, while the periodic oscillators have a common frequency $F_1 = F_2 = F$ in a coupled system due to the weak interaction. The common frequency F can be further determined with reference to the natural frequencies: $f_1 < F < f_2$, assuming $f_1 < f_2$ (cf. Fig. 4.1(b)). Thus, the common frequency F of mutual synchronized oscillators depends on the initial detuning of the uncoupled oscillators and is located near the natural frequency f_2 of the faster self-sustained oscillator [176].

Frequency synchronization can be further determined with reference to the detuning of the frequency. For this purpose, the frequency difference $\Delta f = f_1 - f_2$ between the natural frequencies of the self-sustained oscillators (in an uncoupled system) is locked, which is an indicator of the equality of the oscillators. The frequencies of the same two oscillators in a coupled system lead to the following frequency difference $\Delta F = F_1 - F_2$ for a defined coupling strength. A plot of the frequency ΔF as a function

of the corresponding detuning frequency Δf demonstrates a characteristic behavior, including a synchronization regime for a defined coupling strength (cf. Fig. 4.1(c)). As a result, a small frequency mismatch in an uncoupled system leads to a frequency synchronization of the same oscillators within a coupled system. However, an excessively high frequency detuning results in a desynchronization of the interacting self-sustained oscillators [176].

The phase differences between two coupled self-sustained oscillators offer additional information concerning their interaction state, as phase-locking indicates an interconnection between the phases of two coupled self-sustained oscillators. The phase difference, like frequency synchronization, depends on different presettings of the coupled oscillator system, such as frequency detuning, coupling strength, and interaction. The phase difference will diverge for coupled oscillators in the desynchronous state, whereas phase synchronization shows a constant phase difference, as indicated by the following equation [176]:

$$n\phi_1(t) - m\phi_2(t) = constant. \tag{4.4}$$

Here, the constant can be specified as $\phi^0 + \Delta\phi$ with the phase shift $\Delta\phi$ resulting from an initial detuning. The variables n and m define the possibility of phase synchronization with a certain phase shift. There is always a slight, usually invisible phase shift between coupled oscillators due to the presence of natural detuning. The degree of the difference between the phases, which indicates the phase shift, is used when classifying the synchronization type. The best-known type is in-phase synchronization, which is based, according to Eq. (4.4), on a small phase difference (Fig. 4.1(a)). A phase shift of π between two phase locked self-sustained oscillators is called an anti-phase synchronization and demonstrates an offset of half an oscillation, which is illustrated using metronomes on a common board in Fig. 4.1(a) [176].

It is worth noting that a frequency synchronization implies a certain phase relation, whereas phase-locking does not imply frequency synchronization [176].

A phase portrait of two coupled oscillators is obtained by plotting their two respective amplitudes as a function of each other. The resulting pattern provides information concerning the degree of interaction between the self-sustained oscillators. The phase portrait of synchronized oscillators with the same frequency and a fixed phase shift corresponds to a rounded form, which refers to the limited cycle discussed in Sec. 4.1.1, whereas strong interaction corresponds to a straight line in the phase portrait. An absence of phase and frequency relations between two coupled oscillators will be reflected in the form of chaotic trajectory in the corresponding phase portrait [176].

4.1.3 Synchronization in a Network

Synchronization can also be observed in a network of oscillators. The properties discussed in Sec. 4.1.2 are also valid for synchronization in a population. The fastest oscillator triggers all of the other oscillators to synchronize, provided that the initial detuning is not excessively high [3, 176, 182]. If more than two oscillators are coupled in an even, regular spatial structure, there are many parameters that must be taken into account, such as the number of oscillators, their respective coupling strength, and the type of interaction. A low coupling strength or excessively diverse natural frequencies can lead to clusters of synchronized oscillators within a network. A clustering is defined as existing when some oscillators are synchronized with their neighbors, whereas other oscillators in the network process oscillate at their natural frequencies. The structure of a network coupling can take different shapes, such as a chain or global coupling, with the latter implying an all-to-all coupling [3, 176, 182].

4.1.4 Synchronization in the Brain

Synchronization also plays a central role in the field of neuroscience. For instance, synchronization behavior is observed in neural ensembles in the brain. A neural ensemble, known as a cell assembly, is a temporary coalition of nervous cells that perform a certain neural computation [3, 16, 73, 176, 182, 183]. A single neuron can be involved in various assemblies [3, 176, 182]. The transient synchronization of clusters of

neurons is suspected to be responsible for essential processes in the brain, such as communication between diverse brain areas [16, 184]. It is widely believed that even the neural computation of consciousness and perception can be interpreted with the theory of transient neural synchrony with reference to dynamic network behavior [16]. Transient interrelated neural pattern activity is used to encode information; hence, neural synchrony has been proposed as a solution for the binding problem (cf. Sec. 4.1.5) associated with the dynamic temporal links between the diverse descriptive attributes that are necessary to finally form a uniform object [16]. Numerous studies concerning experimental investigations into the neural synchrony observed in the entire brain have been published subsequently, while the beginnings of research in this field were based on sensorimotor networks. Controversially, neural synchronization has been discussed in association with the binding problem; however, the extensive experimental and theoretical data indicate that it plays an important role in higher cognitive brain functionality [16].

4.1.5 Binding Problem

In everyday life, humans are exposed to many visual information. Normally, the perception and processing of these large quantities of information takes place automatically [185]: One is not aware of the fact that complex objects are divided into individual areas, such as motion, depth, form, and color, and are then reassembled into complete objects in the brain [16, 185]. The question of how the brain reassembles these individual areas is referred to as the "binding problem" [185].

4.2 Memristively Coupled Van der Pol Oscillators

The mutual coupling of two self-sustained relaxation oscillators that feature a memristive device has been realized experimentally [73, 176, 186]. Two memristive devices with different resistive switching behaviors were used for the memristive coupling, as shown in Fig. 4.2. An Ag-doped TiO_{2-x} memristive device with digital switching behavior (cf. Fig. 4.2(a)) was used; in addition, a double barrier memristive device capable

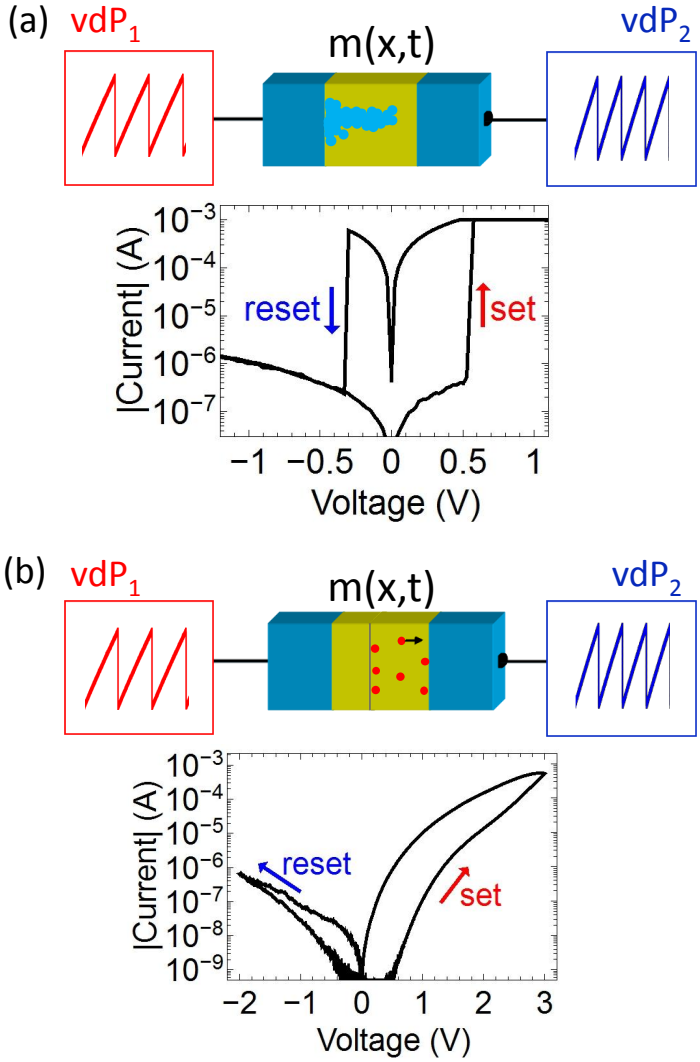

Figure 4.2 Mutually coupled van der Pol oscillators: The coupling was realized either by (a) an Ag-doped TiO_{2-x} memristive device with digital switching behavior or (b) a double barrier memristive device with a gradual, analogue switching behavior. [Adapted from [73, 104].]

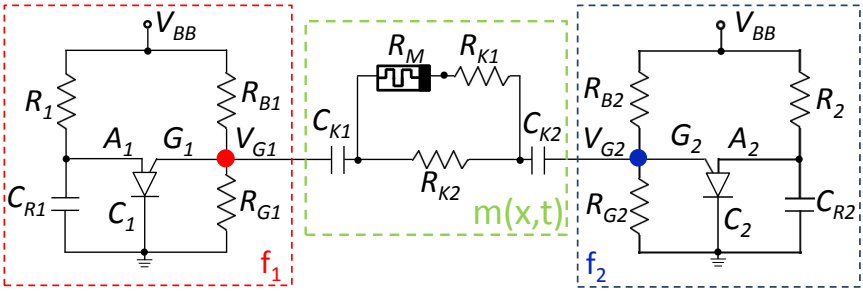

Figure 4.3 Experimental implementation of two mutually coupled relaxation van der Pol oscillators via a memristive device. The key device of the two self-sustained oscillators (highlighted by the dashed red and blue frame) is a programmable unijunction transistor (PUT) with anode ($A_{1,2}$), cathode ($C_{1,2}$), and gate ($G_{1,2}$) terminals. The oscillators are pulse-coupled via a memristive resistor subnetwork m(x,t) (marked by a green frame). (cf. Ch. A) [Adapted from [16] / CC BY-NC 4.0.]

of incremental resistance change (cf. Fig. 4.2(b)) was implemented in the oscillator circuit. The memristively coupled oscillator circuits demonstrated autonomous phase-locking and frequency synchronization due to changes in the memristive device's resistance [73, 176, 186].

The basic structure of the experimentally realized electronic circuits is depicted in Fig. 4.3. Both circuits consisted of two PUT-based oscillators, as described in Sec. 3.8, with different natural frequencies f_1 and f_2 (indicated by red and blue frames, respectively), which were connected by a resistor-capacitor (RC) coupling subnetwork with a single memory device m(x,t) (indicated by an orange frame). The memory behavior is introduced by the time t and the state variable x describes the condition of the memristive device [49, 51, 73].

The implementation of memristively coupled self-sustained oscillators is feasible due to the fact that the frequency of each oscillator can be adjusted via the gate potential V_G. As such, the two PUT-based oscillators with different frequencies f_1 and f_2 were pulse-coupled through modifiable pulses at the gate terminals V_{G1} and V_{G2} (see Fig. 4.3), rather than by sawtooth oscillation at the anode terminals. Thus, the

threshold voltages $V_{G1,2}$ of oscillators 1 and 2 are influenced by the gate potentials $V_{G2,1}$, respectively. This mutual influence is classified as threshold coupling network, which was previously described by van der Pol *et al.* [176,187]. The coupling subnetwork $\mathrm{m}(x,t)$ that binds the gate terminals consists of a memristive device R_M in a series connection with a commercial resistor R_{K1} and a parallel resistor R_{K2} (the dashed green frame in Fig. 4.3). The general task of the resistor R_{K1} is to avoid a rigid coupling of the two oscillators, whreas the parallel resistor R_{K2}, together with the capacitors C_{K1} and C_{K2}, ensures a small time constant of the resistor network. The two resistors fulfill further functions, which depend on the selection of the memristive device in the circuit; each circuit is therefore individually described in the following sections. In addition, two capacitors $C_{K1} = C_{K2}$ within the coupling network form the DC potential decoupled connection between the oscillators at the gate terminals. The coupling network $\mathrm{m}(x,t)$ is a passive high-pass filter that only allows frequencies above a circuit-specific cut-off frequency f_C to be passed. The cut-off frequency f_C of the complete RC network is determined using the following equation [73]:

$$f_C = \frac{1}{2\pi m(x,t) C_K} \tag{4.5}$$

The cut-off frequency is thus a function of the resistance state R_M of the memristive device, which changes from HRS to LRS due to pulse-coupling [73]. Both the HRS and the LRS differ significantly between the binary and analogue memristive devices; hence, the exact cut-off frequency f_C is determined separately in the following sections.

4.2.1 Digital Coupling

The mutual coupling of two self-sustained oscillators, as depicted in Fig. 4.3, was realized using an Ag-TiO_{2-x}-Al memristive device with a binary switch.

4.2.1.1 Device Properties

The memristive device was fabricated by M. Hansen as a mesa structure with a layer sequence of Nb(5 nm)/Ag(40 nm)/TiO_{2-x}(10 nm)/Al(40

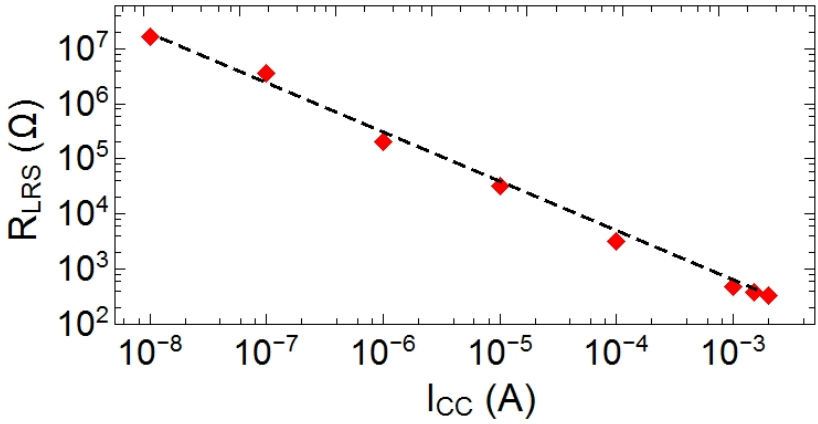

Figure 4.4 The resistance value of the Ag-doped TiO_{2-x} memristive device depends in the LRS on the set current compliance I_{CC}. The red squares are measured data [73]. [Adapted from [73].]

nm) in a three-step photolithography process [73]. Details regarding the procedure used to manufacture the device can be found in Sec. 2.1.4.1. The ECM cells (Sec. 2.1.4.1) demonstrate a switching of their resistance states due to an Ag-filament growth. This procedure is affected to various circumstances, such as pulse duration, polarity, amplitude, and pulse number, and is subject to inherent stochastic processes [52, 73]. This inherent stochasticity makes it difficult to control the switching behavior of the memristive device, even if consistent repetitive pulse trains are applied [73]. In the LRS, the memristive device requires a current compliance I_{CC} in order to avoid electrical damage. However, the resistance R_{LRS} of the device is significantly influenced by the value of the current compliance, as depicted in Fig. 4.4. A current compliance that is too low prevents the device from switching to the LRS. Therefore, the resistor-coupling network was chosen carefully. The resistance R_{K2} limits the current flow through the branch with the memristive device in the HRS and thereby ensures that the device remains intact. The resistance R_{K1} operates as a voltage divider with the memristance R_M in the LRS. Considering a resistance $R_{K2} = 47$ kΩ and a memristance of

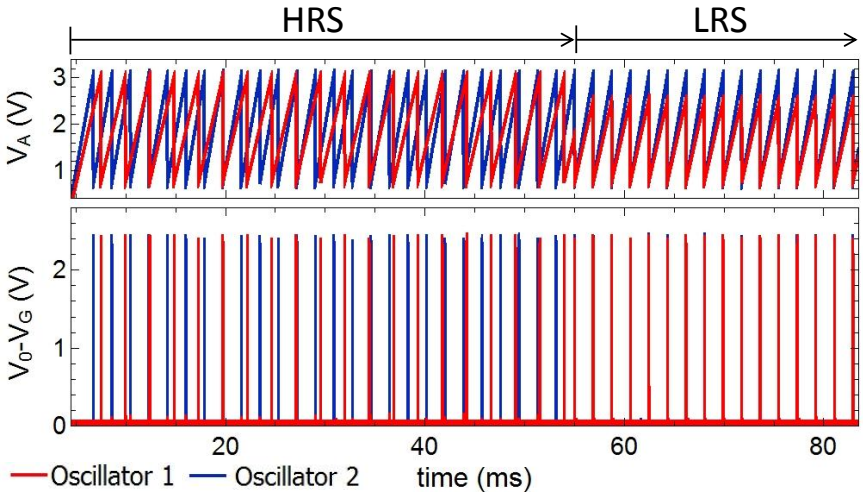

Figure 4.5 Measured voltage curves at the anodes $V_{A1,2}$ of oscillator 1 (red) and oscillator 2 (blue) shown in the upper figure. The gate voltages $V_{G1,2}$ are measured at the red and blue points in the circuit from Fig. 4.3, respectively. The frequencies and phases of both oscillators are locked autonomous after 55 ms. (cf. Ch. A). [Adapted from [73].]

$R_M = 1$ MΩ in the device's HRS, the coupling capacitors were selected as $C_{K1} = C_{K2} = 33$ nF. This resulted in a cut-off frequency $f_C = 215$ Hz according to Eq. (4.5), ignoring the resistance R_{K1} with the condition $R_{K1} \gg R_M$ due to the HRS of the memristive device [73].

4.2.1.2 Circuit Performance

In order to obtain some insight into the synchronization phenomena, the anode voltages $V_{A1,2}$ and gate voltages $V_{G1,2}$ (converted to $V_0 - V_{G1,2}$) were measured during the device switching; the results obtained are plotted in Fig. 4.5. A Tektronix TDS 7104 oscilloscope was used for measurement. A constant voltage $V_{BB} = 25$ V was applied to the circuit using the Agilent E5263A source measurement unit (SMU). The voltage offsets $V_0 = V_{01} = V_{02} = 2.74$ kΩ at the gate terminals arose from the voltages across $R_{G1,2}$, which were defined by the supply voltage applied at

the voltage divider $R_{B1,2}$ and $R_{G1,2}$. The voltage offsets were considered as being constant while charging the capacitors $C_{R1,2}$ until the threshold value of the circuit was reached [73].

At first, the two oscillators were decoupled due to an initially high-ohmic resistance state $R_M = 1$ MΩ of the Ag-TiO_{2-x}-Al memristive device. This was noticeable in the different frequencies of oscillator 1 (the red curve in Fig. 4.5) and oscillator 2 (the blue curve in Fig. 4.5), which oscillated with their natural frequencies $f_1 = 410$ Hz and $f_2 = 538$ Hz, respectively. The two capacitors $C_{R1,2}$ of the self-sustained oscillators were charged with the time constant $\tau_{1,2} = R_{1,2}C_{R1,2}$ until the threshold voltage $V_{\theta 1,2}$ of each relaxation oscillator was reached (Sec. 3.8). The threshold voltages were approximately the same, with $V_{\theta 1} = V_{\theta 2} = 3.1$ V, as well as the capacities, with $C_1 = C_2$; however, the integrator resistances R_1 and R_2 differed significantly. This leads the threshold of oscillator 1 being reached more rapidly, due to $\tau_1 \ll \tau_2$. This individual oscillation with the natural frequencies could be observed in the initial 55 ms (Fig. 4.5). After 55 ms, a synchronization of the two oscillators could be observed, accompanied by frequency synchronization and phase-locking [73].

4.2.1.3 Threshold Modification

The reason for the frequency synchronization and phase-locking lies in the pulse coupling of the two self-sustained oscillators. Each discharge phase of oscillator 1 led to a generation of a gate pulse (the red curve in the lower graph in Fig. 4.5). During the desynchronous state, these generated pulses were applied to the memristive device, which was initially in the HRS. In this phase, the pulses generated by oscillator 2 have no influence on the memristive device, as they are applied to the device as negative voltage pulses. However, the pulses of oscillator 1 had a significant influence on the memristive device, as they caused the device to changes its resistance from the HRS to the LRS at some point. This resulted in an increase of the coupling strength between the self-sustained oscillators. As a consequence, any discharge of the faster oscillator (in this case, oscillator 2) would trigger a discharge of oscillator 1 due to the modification of its threshold $V_{\theta 1}$ [73]. The threshold voltage $V_{\theta 1}$ of

oscillator 1, as modified by oscillator 2, can be determined as follows:

$$V_{\theta 1} = 0.6\ V + V_{G1} = 0.6\ V + V_{BB}\frac{R_{G1}||R_{N2}}{R_{B1} + R_{G1}||R_{N2}} \tag{4.6}$$

$$with \quad R_{N2} = (R_{K2}||(R_M + R_{K1})) + R_{G2} \tag{4.7}$$

In the case that the memristive device is in the HRS, oscillator 2 has no influence on the threshold voltage $V_{\theta 1}$ due to $R_{G1} << R_{N2}$. Thus, the threshold $V_{\theta 1} = 3.04$ V is determined solely by the circuit parameters of the self-sustained oscillator 1. The LRS of the memristive device $R_M = 1$ kΩ, together with the spiking of oscillator 2 ($R_{G2} \approx 0$ due to an electrical short of PUT 2), influences the threshold of oscillator 1, leading it to assume the value $V_{\theta 1} = 2.4$ V; this leads to phase and frequency synchronization of the two self-sustained oscillators [73].

It is worth noting that the application of coupled oscillators is of interest to the field of neuromorphic engineering, as it is energy-efficient [73, 187].

4.2.1.4 Voltage Difference

To gain deeper insight into the synchronization process involved in frequency and phase-locking, two representative pulses of the oscillators, represented as voltage difference $V_{G1} - V_{G2}$, are shown in Fig. 4.6: one for the HRS state of the device and one for the LRS. As a result, subsequent pulses can be up to 1.4 ms apart from each other, with a pulse width of 38 µs and a pulse amplitude of 2.4 V in the HRS of the device, whereas the voltage difference $V_{G2} - V_{G1}$ of the synchronized state (S) of a memristive device in the LRS is characterized by two voltage peaks with a width of 4 µs and an amplitude of 1.1 V. This can be attributed to a concurrent generation of voltage pulses at the gate terminals with contrary polarities. A complete synchronization results in a voltage difference of zero; however, the voltage peaks in the S phase, indicating a phase shift between the generated pulses due to an initial frequency mismatch. More precisely, generating a pulse from oscillator 2 triggers a pulse generation of oscillator 1, with a time delay of 4 µs. This time delay leads in the voltage difference to the indicated negative voltage peak. The simultaneous presence of the gate pulses of both oscillators with different polarities causes an overlap of the pulses;

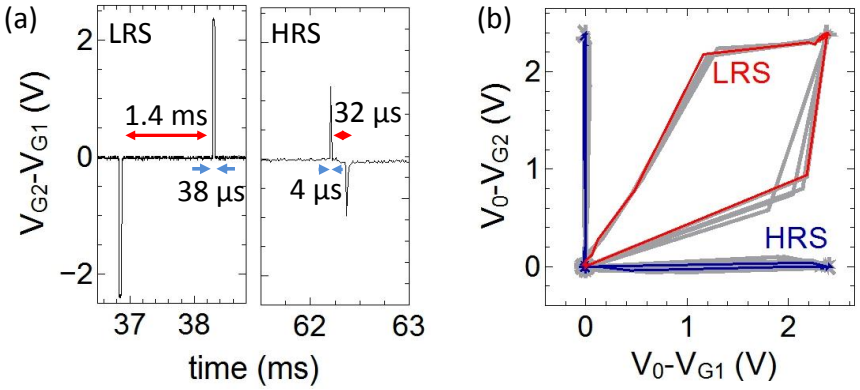

Figure 4.6 Circuit characteristic: (a) Two pulses represented as voltage difference $V_{G1} - V_{G2}$ in the desynchronous (DS) and synchronous (S) state. (b) Phase portrait of a coupled oscillator system. One pulse was marked as blue from DS state (HRS) and one pulse as red from S state (LRS) [73]. (cf. Ch. A). [Adapted from [73].]

this results in a vanishing of the voltage difference $V_{G2} - V_{G1}$ for 32 µs. The PUT of oscillator 2 becomes high-ohmic, which causes the PUT of oscillator 1 to also close, with a time delay of 4 µs. The time delay again causes a voltage peak in the voltage difference $V_{G2} - V_{G1}$, this time of the opposite polarity [73].

4.2.1.5 Phase Portrait

The phase portrait displays the mechanism of synchronization more clearly (cf. Fig. 4.6(b)). For this purpose, the gate pulses were plotted as $V_{01} - V_{G1}$ vs. $V_{02} - V_{G2}$. The gray curves represent the entirety of the synchronization process; two curves, which once indicated the desynchronous state (DS) caused by the memristive device $R_M(x,t)$ being in the HRS (the blue curve) and the S state caused by the memristive device being in the LRS (the red curve), are highlighted. The DS state is characterized by three significant points, which arise according to the digital form of the gate pulses and thus do not indicate any correlation

between the gate pulses. A relationship, in the form of a hysteresis between the gate voltages, can be seen as soon as the S phase was reached via a memristive device in the LRS. A complete synchronization of both self-sustained oscillators would result in a straight line, starting from the point of origin up to 2.2 V in the phase portrait; however, the hysteresis indicates a synchronization phase of the same frequency but a constant phase shift [73, 176]. Thus, a frequency synchronization with a constant phase shift is achieved by the memristive device shifting from the HRS to the LRS due to positive pulses being applied to the device during the DS state [73].

4.2.1.6 Simulation Results

The memristively coupled self-sustained oscillators are mathematically defined by mutually coupled van der Pol oscillators, which can be described using nonlinear equations [73]:

$$\frac{d^2x_1}{dt^2} - \alpha_1(1 - x_1^2)\frac{dx_1}{dt} - \beta_1 x_1 \frac{(x_1 + \gamma_1)^2}{\gamma_1^2} = m(x,t)(\dot{x}_2 - \dot{x}_1) \tag{4.8}$$

$$\frac{d^2x_2}{dt^2} - \alpha_2(1 - x_2^2)\frac{dx_2}{dt} - \beta_2 x_2 \frac{(x_2 + \gamma_2)^2}{\gamma_2^2} = m(x,t)(\dot{x}_1 - \dot{x}_2) \tag{4.9}$$

with the positive values $\alpha_{1,2}$, $\beta_{1,2}$, and $\gamma_{1,2}$, which modifying the frequency and the damping behavior of each individual self-sustaining oscillator system. Mutual coupling is implemented by the positive coupling strength $\mathrm{m}(x,t)$ depending on the state variable x. Two binary states are considered for the coupling strength $\mathrm{m}(x,t)$ based on the switching mechanism of the memristive device. A weak coupling m_0 represents an uncoupled oscillator system as a result of a high-ohmic memristive device $R_M(x,t)$, whereas a coupled system with a memristive device in the LRS is identified by a strong coupling m_1. This makes it possible to define the overall coupling strength using the Heaviside step function θ [73]:

$$m(t) = m_0\theta(t_S - t) + m_1\theta(t - t_S) \tag{4.10}$$

Here, the time t_S defines the point in time at which the memristive

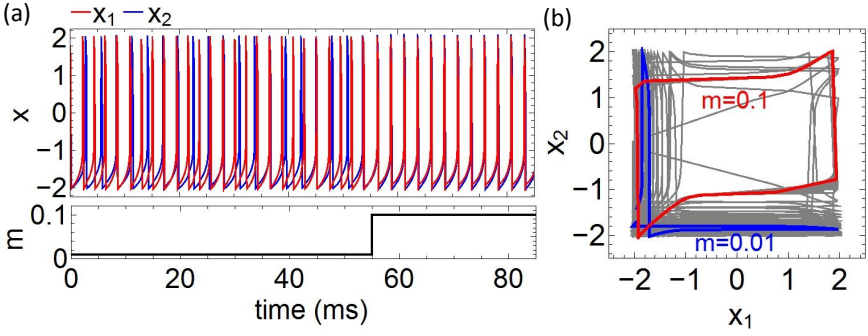

Figure 4.7 Simulation performance: (a) State variables x_1 and x_2 represent the coupled oscillators 1 and 2, respectively. According to the coupling strength m a phase and frequency synchronization is observed after 55 ms. (b) The phase portrait of the simulated oscillator network with highlighted cycles with low (red) and high (blue) coupling strength [73]. (cf. Ch. B). [Adapted from [73].]

device shifts from the HRS to the LRS. Thus, a time $t < t_S$ results in a weak coupling strength $m(t) = m_0$; whereas the condition $t \geq t_S$ leads to a strong coupling strength, which corresponds to the memristive device in the LRS. Furthermore, the well-known van der Pol equation [169,187,188] was extended by the addition of a nonlinear term $[x_{1,2}(x_{1,2}+\gamma_{1,2})^2/\gamma_{1,2})^2]$ in order to correspond with the digital character of the gate pulses of the self-sustained oscillators, as was similarly demonstrated in the publication of Postnov *et al.* [189]. Here, the variables $\gamma_{1,2}$ determine the number of generated pulses by a single van der Pol oscillator within a time interval [73].

The simulation results of the state variables x_1 and x_2 of the van der Pol oscillators are shown in Fig. 4.7(a). In the beginning, both oscillators followed their own natural frequencies, defined by $\gamma_{1,2}$ due to a low coupling strength of $m_0 = 0.01$. After reaching the switching time t_S, the coupling strength switched to $m_1 = 0.1$, which lead to phase-locking and frequency synchronization [73].

The phase plot of the simulated oscillator system is defined by x_1 as a function of x_2, with an emphasized cycle of the uncoupled system (the

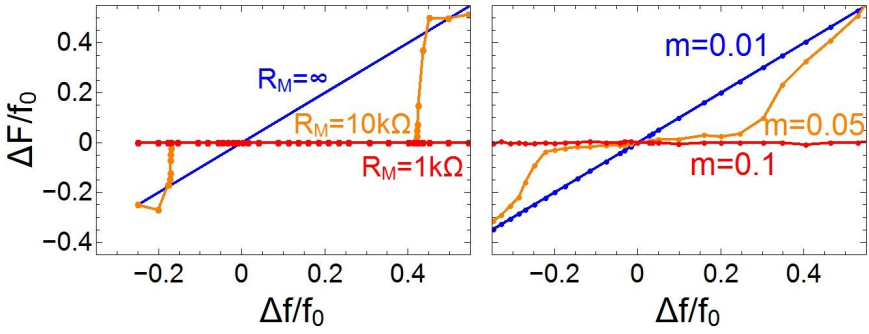

Figure 4.8 Frequency detuning: The frequency difference ΔF of the coupled oscillator system as a function of the frequency mismatch Δf for three different coupling strengths (cf. Ch. A, B). [Reproduced from [73], with the permission of AIP Publishing.]

red curve) and a cycle of the synchronized phase (the blue curve) (Fig. 4.7(b)). The theoretical data here correspond to the experimental data (Fig. 4.6), resulting in three digital points at a weak coupling strength ($m_0 = 0.01$) and a hysteresis at a strong coupling strength ($m_1 = 0.1$), which resulted in a frequency synchronization with a constant phase shift [73].

4.2.1.7 Frequency Detuning

Further information concerning the oscillator system can be obtained with reference to frequency detuning (cf. Sec. 4.1.1) [73, 176]. Therefore, the frequency mismatch $\Delta f = f_1 - f_2$ of the uncoupled system is plotted as a function of the frequency difference $\Delta F = F_1 - F_2$ of the coupled oscillator system, as shown in Fig. 4.8 [73, 176]. The frequency detuning was measured (left graph) and simulated (right graph) for the following resistance values and coupling strengths, respectively: uncoupled system $R_M = \infty$ and $m = 0.01$, $R_M = 10$ kΩ and $m = 0.05$, and $R_M = 1$ kΩ and $m = 0.1$. Measurements were obtained by maintaining the natural frequency $f_1 = 410$ Hz of oscillator 1 constant, whereas the natural frequency f_2 of oscillator 2 was swept in a range

of between 310 Hz to 640 Hz. Standardization of the measurement and the simulation on the frequency $f_1 = f_0$ allows better comparison. As a result, the orange and red curves show the characteristic behavior of weakly coupled oscillators for the defined coupling strengths, including a synchronization area. Furthermore, an increased coupling strength leads to an increased synchronization area; thus, the frequency mismatch that leads to a synchronization will be more pronounced when the coupling strength is higher, whereas the uncoupled system (the blue curves) is indicated by an independent straight line with no synchronization area. The asymmetric behavior of the frequency detuning is achieved by the adjustment of the frequencies towards the common frequency F of the mutually synchronized oscillators, which is always regulated in favor of the faster frequency (f_1) (Sec. 4.1.1) [73, 176].

4.2.2 Analogue Coupling

A self-organizing nonlinear dynamic system comprised of two mutually coupled self-sustained oscillators was realized using an analogue memristive device. Therefore, the pulse coupled circuit displayed in Fig. 4.3 was implemented.

4.2.2.1 Device Properties

The double barrier memristive device (Sec. 2.1.4.2) used has a layer sequence of $Nb/Al/Al_2O_3/Nb_xO_y/Au$; it was fabricated by M. Hansen, using a standard photolithography process. The memristive device exhibits a continuous change in resistance, rather than a digital switch. The switching of the resistance state occurs due to oxygen diffusion and variations within the Nb_xO_y layer, as indicated in Fig. 4.2(b) [104]. This procedure is affected by different circumstances, such as pulse duration, polarity, amplitude, and pulse number, and is subject to inherent nonlinear dynamical processes with a retention. The inherent nonlinearity and the retention make it difficult to completely control the switching behavior of the memristive device; even if consistent repetitive voltage pulse trains are applied [104]. Therefore, the circuit parameter of the implemented oscillator network shown in Fig. 4.3 was carefully

chosen in order to permit an autonomous transition from a desynchronous to a synchronous phase.

4.2.2.2 Circuit Design

The circuit design shown in Fig. 4.3 was used for the analogue coupling. In addition, two instrumentation amplifier were taken, as shown in Fig. 4.9, to measure the voltages across the memristive device R_M and the resistor R_{K1}. The measurement with an instrumentation amplifier with a very high input impedance of the voltage across the memristive device was only done to prevent any influence on the high-impedance of the memristive device. Whereas the measured voltage across the resistor R_{K1} was amplified by a factor of 102 using the instrumentation amplifier from Fig. 4.9.

The values of the amplitudes of the gate pulses were selected with regard to the characteristics of the double barrier memristive device. The double barrier memristive device has the advantage of not requiring an external current compliance due to the Al_2O_3 tunneling layer, as only a restricted number of oxygen ions can adhere to both interfaces [104]. However, under normal circumstances, the memristive device can tolerate voltages of up to 4 V. This was taken into account when choosing the voltage amplitude of the positive applied gate pulses V_{G1} generated by oscillator 1. In addition to the time t and the state variable x, the positive pulse amplitude determines the resistance state of the memristive device due to a device-specific electrical field ϵ dependency. An excessively high voltage amplitude of the gate pulse V_{G1} would produce an initially low resistance state due to the electrical field dependence of the device, which can lead to an absent desynchronous phase. At the same time, the amplitude of oscillator 1 must be sufficiently high to ensure that the memristive device continuously switches with intermediate states.

It is worth mentioning that, with an increased voltage amplitude, the range of resistance change decreases, as the hysteresis decreases. The gate voltage $V_{G1} = 2.26$ V of oscillator 1 was selected taking these points into account, whereas the gate pulses of oscillator 2 were applied as negative voltage pulses to the memristive device and thus effected a reset

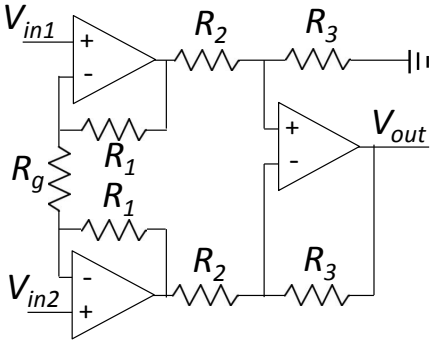

Figure 4.9 Instrumentation amplifier realized with operational amplifiers and commercial resistors. The output voltage results as follows: $V_{out} = (V_{in1}$ - $V_{in2})Gain$. The gain factor $Gain$ can be adjusted via the resistors. The memristive device from the circuit shown in Fig. 4.3 was measured with a $Gain = 1.002$ and the shunt resistor R_{K1} with a gain factor of $Gain = 100.2$ [190]. (cf. Ch. A) [A similar figure is published in [190].]

of the device. In order to avoid a pronounced active reset caused by the gate pulses V_{G2}, in addition to the intrinsic retention of the device and the asymmetrical shape of the $I - V$ characteristic, the lowest possible pulse amplitude was selected for oscillator 2. Therefore, a gate voltage $V_{G2} = 0.53$ V was selected for oscillator 2. It is also worth noting that, due to the high-resistance state at negative voltages, a unidirectional coupling of the oscillator system, which can also be observed in biology between the pre-synaptic and the post-synaptic neuron, was achieved.

Due to the extremely nonlinear and voltage-dependent $I - V$ characteristic, it is difficult to achieve a desired initial coupling strength with the resistance value of the double barrier memristive device by simply adjusting the voltage amplitude of the gate voltage V_{G1}. For this reason, the initial coupling strength was further adjusted via the resistance network (cf. Fig. 4.3), meaning that frequency synchronization and phase-locking occurred after an initially desynchronous state. The parallel resistor R_{K1} reduces the total resistance of the coupling circuit, resulting in a small time constant, together with the coupling capacitors $C_{K1} = C_{K2}$. The resistor in series R_{K2} enables a further readjustment of the total coupling

strength and operates as a shunt resistor for measuring the current I_M in the memristive branch using an instrumentation amplifier. The cut-off frequency of the RC subcircuit is given, according to Eq. (4.5), as f_C = 0.48 Hz and as $f_C = 0.51$ Hz for the device resistances $R_M = 326.5$ kΩ and $R_M = 246.5$ kΩ, respectively.

4.2.2.3 Circuit Performance

In order to further examine the functional mechanisms involved in phase and frequency synchronization, the gate voltages $V_{G1,2}$ of both oscillators and the voltage V_M across the double barrier memristive device were recorded using an interposed instrumentation amplifier, alongside a PicoScope 3000 Series mixed-signal oscilloscope. The frequencies $f_{1,2}$ and the resistance state R_M calculated based on these measurements are shown in Fig. 4.10. By considering the two aspects of the switch dynamic and retention of the memristive device, the natural frequencies of the two independent oscillators 1 and 2 are $f_{1N} = 833$ mHz and f_{2N} = 625 mHz, respectively. In this way, the time of the oscillation was around 1 s and (very) roughly comparable to the response time of the analogue device. This becomes clear considering the resistance state of the memristive device after switching off the oscillator network, which is in a synchronous state. For this purpose, the resistance value was measured immediately afterwards and once again after a time delay of 1 minute. A comparison of the two resistance measurements identified a noticeable reduction of the resistance state after 1 minute. Consequently, one might expect an interesting coupling scenario of the two oscillators, because coupling strength and oscillator frequencies mutually interact. It is worthwhile to mention that this experiment is biological justifiable. Synapses exhibits, as well as the applied analogue device, a forgetting rate and neurons in the close neighborhood actively influence the synaptic coupling strength.

Initially, both self-sustained oscillators follow their natural frequencies $f_1 = f_{1N}$ and $f_2 = f_{2N}$. The initially uncoupled desynchronous state (DS) is the result of a resistance state of $R_M = 326.5$ kΩ (see lower graph of Fig. 4.10), which can be considered in this case as the HRS of the memristive device. For the first 624.8 s, the oscillator network

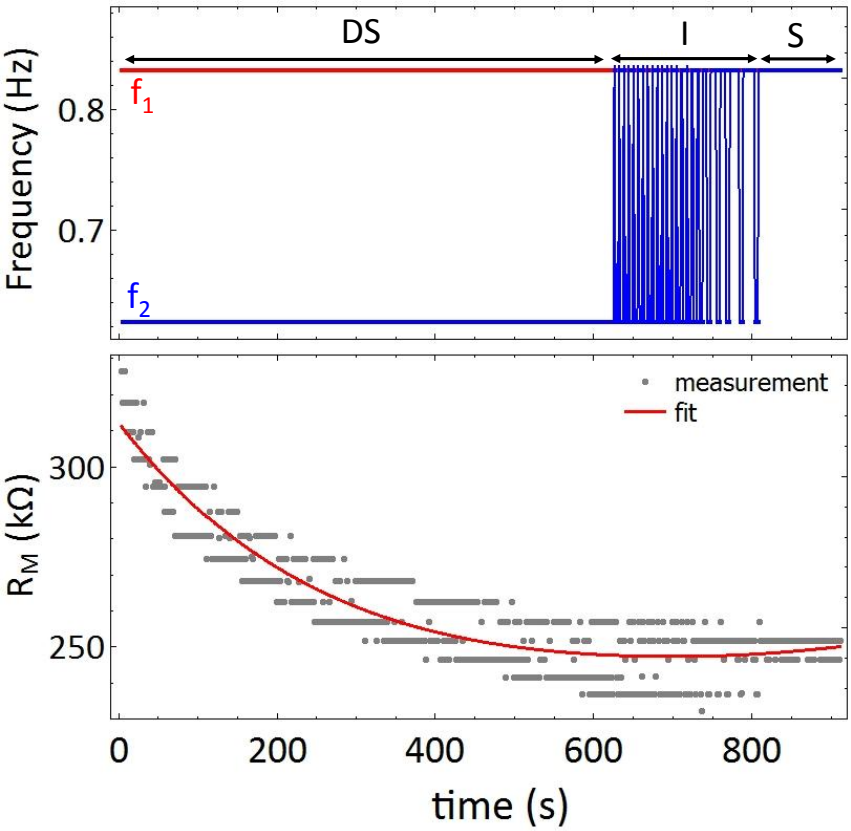

Figure 4.10 Circuit characteristic: Upper graph: The frequency course $f_{1,2}$ of both self-sustained oscillators as a function of time t. The continuous resistance change of the double barrier memristive device causes a desynchronous state (DS), an intermediate state (I), and a synchronous state (S). Lower graph: The gray dots indicate the corresponding resistance state of the double barrier memristive device. The exponential decrease of the resistance state is highlighted by a fit curve. (cf. Ch. A, B)

remained desynchronous until the intermediated state (I) was reached (see the upper graph in Fig. 4.10). This state is characterized by the fact that the individual pulses of oscillator 1 triggered oscillator 2 to generate a gate pulse (Sec. 3.8). The number of triggered pulses within a time interval t increases with the on-going measurement until phase and frequency synchronization were reached in the S phase, beginning at 808.2 s. Oscillator 1 oscillated with its natural frequency over the entire period of time measured, because the pulses of oscillator 2 are applied in the reverse direction of the diode-like characteristic of the double barrier memristive. As a result, the pulses of oscillator 2 are blocked by the memristive device. It is worth mentioning that a further double barrier memristive device connected antiparallel to the existing memristive device has no influence on the measured values; because the voltage-dependent memristive device would still have a resistance value of several megohms due to the weak voltage amplitude of $V_{G2} = 0.53$ V of oscillator 2, which has no noticeable influence on the frequency of oscillator 1. However, oscillator 1 with a voltage amplitude of $V_{G1} = 2.26$ V has a noticeable influence on the frequency of oscillator 2. Therefore, the frequency of the oscillator 2 occupied one of two digital states, either the frequency f_{2N} (corresponding to its natural frequency) or the frequency f_1 of oscillator 1.

In particular, in the desynchronous phase, the frequency of oscillator 2 is equal to its natural frequency; however, in the I phase, oscillator 2 generated pulses of either the frequency f_{2N} or f_{1N} at irregular time intervals. Finally, phase-locking and frequency synchronization of the two oscillators led to a common frequency of $f_1 = f_2 = f_{1N}$ in the S phase. The entire time to complete synchronization took 800 seconds.

4.2.2.4 Resistance Change

The resistance change of the double barrier memristive device is shown in the lower graph of Fig. 4.10. The resistance values were specified during the generation of the gate pulses of oscillator 1 (the gray dots) because the current I_M was within a measurable range. As a result, the memristive device continuously decreased its resistance state, starting from the HRS. In particular, individual discrete levels are achieved; however, there was a fluctuation in the resistance states between the levels over time. The

fluctuation of the resistance value was due to the nonlinearity of the memristive device. A superposition of the pulses with different polarities resulted in a reduction of the positive applied voltage amplitude at the device.

In the desynchronous phase, a decrease of the resistance from R_{HRS} = 326.5 kΩ to R_M = 257.1 kΩ was achieved, with several intermediate levels. While in the I phase, there was a continuous alternation between five resistance levels (R_M = 237 kΩ, 242 kΩ, 247 kΩ, 252 kΩ, 257 kΩ), which continued until the synchronous phase finally ensued, during which the resistance value of the device was either R_M = 246.5 kΩ or R_M = 251.7 kΩ. The measured data can be adjusted using an exponential decay function:

$$R_M(t) = R_{LRS} + (R_{diff} \exp(-\alpha t)) \tag{4.11}$$

Here, R_{LRS} is the final resistance state. R_{diff} indicates the overall decrease in resistance, and α is a device-specific constant. The device-specific constant should be roughly comparable to the response frequency of the analogue device to achieve an interesting coupling scenario of the two oscillators. The parameters for the adjustment from Fig. 4.10 are as follows: R_{LRS} = 249 kΩ, R_{diff} = 66 kΩ, and α = 4.7 ms^{-1}.

4.2.2.5 Intermediate Phase

In order to obtain a more detailed perspective on the intermediate phase, the frequency f_2 of oscillator 2 was considered as a function of the conductivity of the double barrier memristive device. In particular, the frequency of oscillator 2 at the natural frequency f_{1N} = 0.833 Hz of oscillator 1 was examined, as shown in Fig. 4.11. Thus, only the pulses of oscillator 2 will be considered, which are triggered by oscillator 1. As a result, the increased conductivity of the memristive device led to an increased triggering of the gate pulses of oscillator 2 by oscillator 1. It should be noted here that the conductivity was determined by the fit curve from the Fig. 4.10, rather than the measured conductivity displayed in Fig. 4.10.

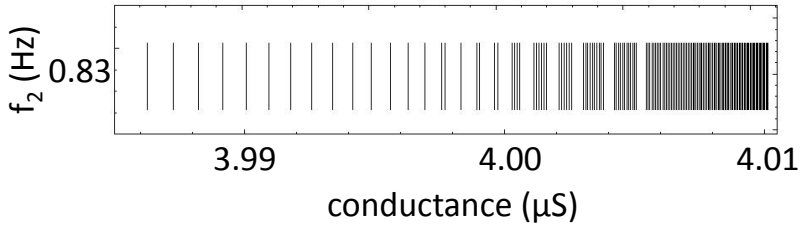

Figure 4.11 The oscillator frequency f_2 as a function of the conductivity of the double barrier memristive device. The frequency f_2 was only examined in the interval of the intermediate state from the Fig. 4.10 at the natural frequency of oscillator 1. The strokes indicate when the oscillator 2 is forced to generate a spike by oscillator 1 and thus, to oscillate with the natural frequency $f_1 = 0.833$ Hz of oscillator 1. It should be pointed out here that the conductivity is determined by the fit curve from Fig. 4.10 rather than the measured conductivity. (cf. Ch. A).

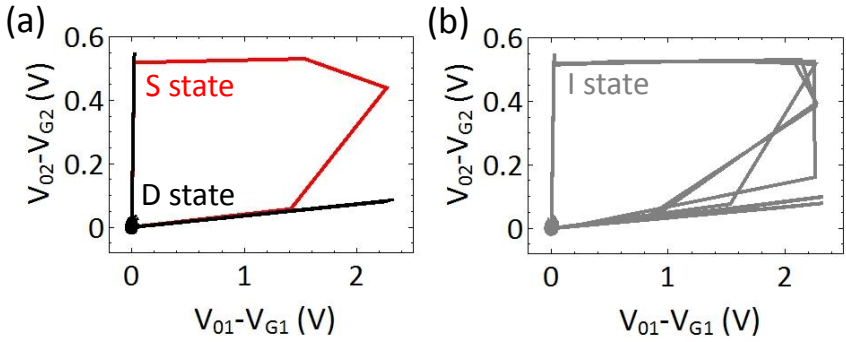

Figure 4.12 Phase portrait of (a) the desynchronous (D) and synchronous (S) state represented by one cycle in black and red, respectively, as well as (b) the intermediate (I) state. (cf. Ch. A).

4.2.2.6 Phase Portrait

The behavior of the I state can be determined in more detail by means of the phase portrait. To do so, two representative cycles of the DS and S state were first determined, as shown in Fig. 4.12(a). The cycle from the DS state displays a typical behavior, which is indicated by a shape that is parallel to both axes; this is due to the digital character of the gate pulses. The hysteresis of the cycle from the synchronous state indicates phase-locking and frequency coding of the two oscillators, while the phase portrait of the I state is shown separately in Fig. 4.12(b). The phase portrait of the I state shows both characteristic digital behavior that is comparable to the DS state and hysterical processes that are similar to the S state.

4.3 Memristive Stochastic Plasticity Enables to Cope the Binding Problem

Human consciousness and the human brain's ability to perceive are believed to be the consequences of parallel information-processing in a distributed dynamical self-organized nervous system [3, 16, 19]. The neural computational approach that many believe may allow for this information-processing challenge to be overcome is neuronal synchronization, which would make it possible to employ the inherently dynamic characteristics of a network [3, 16, 33, 191, 192]. It is widely believed that, due to the simultaneous temporal occurrence of neuronal activity patterns, a coding in the form of consistent conditions is achieved (cf. Sec. 4.1.4) [16, 32]. In this manner, the binding problem (cf. Sec. 4.1.5) can be addressed by creating a temporal dynamic connection between the various attributes of an identical object [16, 24, 33–35]. After the initial experimental measurements of the sensorimotor cortex made it possible to establish a theoretical basis [16, 193, 194], further studies were also able to apply this approach to the entire brain [16, 32, 191]. Such investigations focused on the dynamic processes of phase synchronization of neuronal activity patterns that occur in the form of neuronal communication between different areas of the brain. In recent years, the temporal synchronization approach has been discussed, often somew-

hat controversially; however, the theoretical and experimental findings prove a connection between cognitive brain functions and synchronization [16, 25, 191, 195].

In the following sections, it is argued that memristive devices have certain advantages when emulating neuronal synchronization, as they represent a local memory that enables transient, dynamic, and context-dependent bindings in a neuromorphic circuit. An oscillator network with integrated memristive devices has the ability to address two aspects of the binding problem: information storage, through stochastic plasticity, and long-lasting association of information [16]. The electrochemical metallization cells (Sec. 2.1.4.1) fabricated by M. Hansen were used for the memristively coupled relaxation van der Pol oscillators [16, 169, 187, 188]. The oscillator network is demonstrated by its application to the binding problem posed by a "bistable" object, where a slight deviation in the attention paid to the same object causes a binding of diverse attributes. Therefore, the stochastic plasticity of the memristive device enables the temporary synchronization of selected oscillators depending on the context. Based on a description of the inherent stochasticity of a memristive device that features a distribution probability, a model that enables an autonomous transition from the desynchronous to the synchronous phase is described [16].

4.3.1 Temporal Binding Problem

An illustration of neural synchronization is shown in Fig. 4.13 [16, 196, 197]. It indicates that attention determines which attributes of the same object are linked for a transient, context-depending binding [16, 33]. Various perceptions of the same bistable illustration (Fig. 4.13(a)) stem from the possibility that the individual attributes (marked 1 to 4 in Fig. 4.13) can be connected with the body of the hippo (marked A in Fig. 4.13); alternatively, a shift in attention might result in the attributes being considered as part of the background (marked B in Fig. 4.13) [16, 196, 197]. This means that the attributes are not rigidly bound to an object, but rather depend on the attention paid to the object in question. For instance, attributes 1 and 2 of the hippo are bound to the background in Fig. 4.13(b); however, in Fig. 4.13(c), there is an

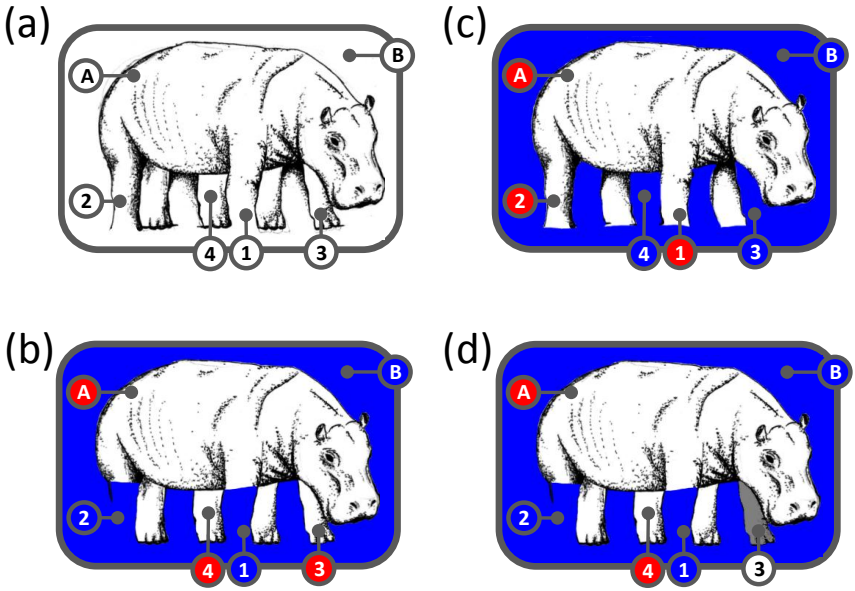

Figure 4.13 Illustration of temporal binding: (a) The ambiguously drawn representation of a hippo enables the temporal binding of the attributes marked with 1 to 4 with one of the two objects. The objects are either the body of the hippo or the background, marked with A or B, respectively. (b) The colored area represents the background, which in this case implies attributes 1 and 2. Whereas attributes 3 and 4 are associated with the hippo's body. (c) The reverse case to (b), where now the attributes 1 and 2 are associated as part of the body due to shifted attention. (d) The case of (b), however, the attribute 3 is considered to be an partial aspect of a separate object [16]. [Reproduced from [16] / CC BY-NC 4.0.] [A similar drawing is published by Shepard [196, 197].]

association of the same attributes with the body of the hippo. Another approach to interpreting the image presented in Fig. 4.13(a) is shown in Fig. 4.13(d): Here, the foot of the hippo (attribute 3) is considered to be a partial aspect of a separate object, which is neither the hippo's body nor the background. It follows from this that different perceptions of the image are possible (Fig. 4.13((b) to (d))), but all are exclusive [16].

In this context, temporal binding can be emulated using the characteristics of cortical neural dynamics [16, 24, 33]. Thus, separate (neuronal) self-sustained oscillators represent attributes 1 to 4 of the hippo's image, which can be bound to one of the object oscillators as representing either the body of the hippo (A in Fig. 4.13) or as part of the background (B in Fig. 4.13). Both object oscillators (A and B) are connected to every single attribute oscillator (1 to 4) in an oscillator network [16]. The circuit topology can be seen more clearly in Fig. 4.14: Here, individual bindings are possible by exploiting the process of synchronization. The four attribute oscillators (1 to 4) can be bound either to the body of the hippo in the red circle, to the background in the blue circle, or with nothing at all. Consequently, higher-level assemblies can vary the perception in a state-dependent manner, which makes different perceptions possible in the first place. Thus, representations of ever-changing sensory impressions are possible [16].

4.3.2 Stochastic Plasticity

Synapses make long-lasting changes to their synaptic strength due to the unique neural activity patterns of adjacent neurons. This leads to either an increase (LTP) or a weakening (LTD) of the synaptic strength, which is the basis for memory and learning processes (Sec. 3.3.1) [14, 16, 19]. A simplified mechanism of long-term potentiation is depicted in Fig. 4.15(a): The number of spikes that encounter a synapse in a certain time interval ΔT is of decisive importance. A high level of neuronal activity corresponding to a certain number of action potentials causes a long-lasting change in synaptic strength, while a limited number of action potentials (low activity) within a certain time interval has no lasting influence on the synapse [16]. It has been simplified assumed compared to biology that the level of attention is coated in the pulse number of an applied voltage train, which results in an LTP of the memristive device.

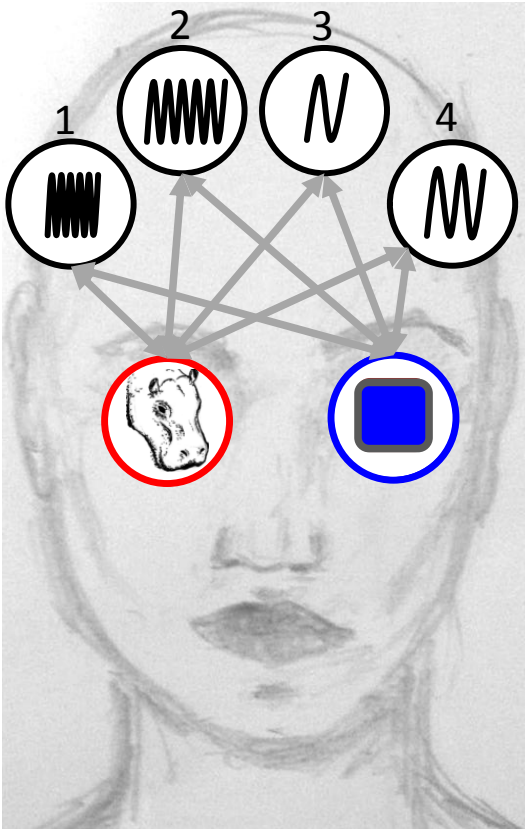

Figure 4.14 Binding process: An oscillator network allows the integration of attribute oscillators (1 - 4) either with the body of the hippo or with the background by means of synchronization. [Derivative of [16] / CC BY-NC 4.0.] [Based on Refs. [196, 197].]

However, this is a simplification to biological synapses, since a long-term potentiation in a biological synapse only occurs under a depolarization of the postsynaptic membrane together with neuronal activity in the presynaptic cell. This leads to a unidirectional potentiation from the pre- to the postsynaptic cell. Here, however, the approach to synchronization is bidirectional [16].

4.3.3 ECM Cell

Electrochemical metallization cells with the layer sequence $Al/TiO_{2-x}/Ag$ (cf. Sec. 2.1.4.1) were used to emulate synaptic functionalities. In general, the properties of this type of memristive device are associated with synapses due to their non-volatile memory and plain, capacitor-like structure [16, 53, 54]. The device demonstrates an inherent stochastic switching behavior [16, 52, 83, 198]. This can be seen more clearly when considering the distribution of the set behavior of 1700 current-voltage sweeps, as shown in the diagram of the distribution of the set voltage of Fig. 2.9 in Sec. 2.1.4.1. As a result, the device switches at different set voltages, meaning that the set distribution can likely be adjusted with a Gaussian distribution. The randomness of resistive switching is due to the large number of different chemical and physical processes involved in filament formation, which can only be approximated to a certain degree [16, 52, 83, 199].

4.3.4 Mathematical Description of Stochastic Plasticity

The randomness of the resistive switching behavior of the devices in biologically oriented circuits is based on the Refs. [52, 108, 200, 201]. The author's take advantage of the fact that the switching of the ECM cells follows a Poisson distribution at applied voltage pulses, with a defined width and amplitude. As a result, switching can be limited to a certain voltage interval, and, within this interval distribution, it can be predicted with a certain probability, which minimizes the randomness of the cells. This makes it possible to control the memristive devices to a certain degree via the number and form (i.e. the amplitude and width) of the applied pulses. The particular influence of the pulse amplitude can be seen in Fig. 4.15(b). For this purpose, the pulse width of the 30 applied

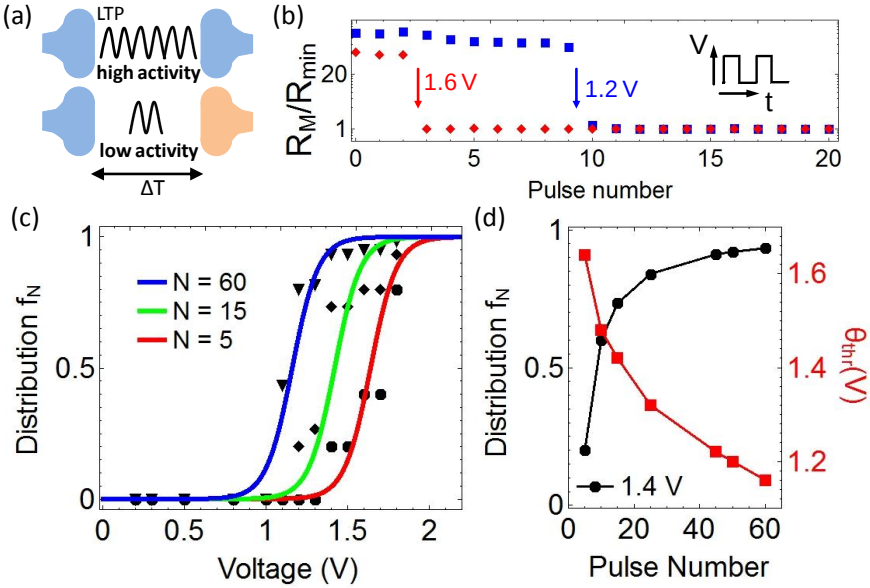

Figure 4.15 Synaptic plasticity with stochasticity: (a) Illustration of an activity-dependent LTP process, where a high neuronal activity within a certain time interval ΔT in a synapse leads to LTP, where low activity has no effect on the synapse between two neurons. (b) A voltage train with a pulse width of 1 ms was applied to the memristive device. The change in the resistance state was measured depending on the pulse amplitudes of 1.6 V and 1.2 V. (c) Probability for switching of the memristive device from the HRS to the LRS as a function of the applied voltage for a different number of voltage pulses within a pulse train, namely, 5, 15, and 60. The measured data are black patterns, while the curves were determined using the distribution function f_N. (d) The effect of the number of pulses in a pulse train for a selected voltage of 1.4 V. The probability of switching increases considerably from 20 percent to 90 percent, when the number of pulses is increased from 5 to 60. An increased pulse number causes a decrease of the threshold voltage θ_{thr} [16]. [Adapted from [16] / CC BY-NC 4.0.]

positive voltage pulses was constant kept at a duration of 1 ms, while the voltage amplitude was either 1.2 V (the blue measured points) or 1.6 V (the red measured points) [16]. As a result, the resistance state of the memristive device changed from the initial HRS to the LRS at a pulse amplitude of 1.2 V after 10 pulses, but applying pulses with a voltage amplitude of 1.6 V caused the device to switch after three pulses. However, the measured number of switches from the HRS to the LRS can vary from measurement to measurement, even with an identical pulse train. This can be perceived with the underlying stochastic nature. Therefore, the switching probability of memristive devices was examined in relation to the number N of applied voltage pulses for defined voltage amplitudes V, as shown in Fig. 4.15.

4.3.4.1 Probability of a Memristive Device Switching

For the ECM cells, binary switching behavior is expected, which results in a normally distributed probability density at a defined pulse train. A normal distribution is also referred to as Gaussian distribution. Thus, the distribution function makes it possible to describe the probability function, which can be determined, assuming no cumulative effects between the individual pulses, as follows [16]:

$$f_N(V) = \frac{1}{1 + e^{-\beta(V-\theta_{thr})}} \tag{4.12}$$

with the device-specific constant β. The variable θ_{thr} can be determined by the condition $f_N(V) = 0.5$, which implies an equal probability for each of the two binary states (HRS or LRS) of the memristive device. The distribution function $f_N(V)$ was determined for switching within a pulse train with $N = 5$, 15, and 60 applied pulses to the memristive device, which are shown as red, green, and blue curves in Fig. 4.15(c), respectively. Furthermore, the measured data are shown as black patterns in Fig. 4.15(c), which were obtained as follows: The measurement data were obtained with the aid of pulse trains composed of 70 positive voltage pulses. Therefore, a voltage train with amplitudes ranging from 200 mV to 1.8 V was applied to the memristive device in its HRS. For each applied voltage train, the pulse number was determined by $N_{SW}(V)$,

according to which the device changed from the HRS in the LRS. The distribution values of the measured data were determined using the following function [16]:

$$f_N(V) = 1 - \frac{N_{SW}(V)}{N} \tag{4.13}$$

Here, the variable N is defined as $N = 5, 15, 60$, depending on the number of pulses applied within a voltage pulse train. For the special case of a memristive device remaining in the HRS within the applied voltage pulse train (5, 15, 60), the distribution value of $f_N(V) = 0$ is valid. The other distribution values of the measured data were determined using Eq. (4.13). These measured values can be approximated with a set of curves by means of Eq. 4.12, as shown in Fig. 4.15(c). For this reason, 12.5 V^{-1} was chosen for the variable β, while the threshold voltages θ_{thr} were chosen depending on $N = 5$, 15, and 60 with 1.64 V, 1.42 V, and 1.16 V, respectively. Thus, an approximation of the stochastic switching of the memristive device can be achieved despite its inherently arbitrary chemical and physical processes [16,52,108,200–202]. The memristive device, with its intrinsic randomness, emulates a varying synaptic strength, since it depends on the number N of applied spikes. As an example, the distribution function f_N, as a function of applied pulses for a specified voltage amplitude of 1.4 V, are shown in Fig. 4.15(d). As a result, the five applied pulses had a switching probability of only 20 percent, but if 60 pulses with the same voltage amplitude of 1.4 V were applied to the memristive device, the probability for a switching would increases to 93 percent, as shown by the black curve in Fig. 4.15(d). Simultaneously, the threshold voltage θ_{thr} calculated using Eq. 4.12 is reduced from 1.64 V to 1.16 V, as shown by the red curve [16].

4.3.5 Mathematical Model of n Memristively Coupled Van der Pol Oscillators

In order to address all of the aspects of the temporal binding problem, it is necessary to develop a model that can address both synaptic plasticity and the association of information [16]. While an approach to the first aspect of the binding problem was previously described in Sec.

4.3.2, the mechanism of neuronal synchrony is used to combine the information obtained. Relaxation (van der Pol) oscillators were pulse-coupled via memristive devices to create a neuromorphic circuit, thus addressing both areas of the binding problem. This electrical circuit can be mathematically described by n nonlinear van der Pol equations [16,73]:

$$\frac{d^2x_i}{dt^2} - \mu(1 - x_i^2)\frac{dx_i}{dt} - \omega_i^2 x_i \frac{(x_i + \gamma)^2}{\gamma^2} = \sum_{i=1}^{n_0}\sum_{j=1}^{n_a} g_M^{ij}\left(\frac{dx_j}{dt} - \frac{dx_i}{dt}\right) \tag{4.14}$$

with the state variable x_i of oscillator i. The damping behavior is defined by the parameter μ, while the nonlinearity and frequency of the self-sustained oscillators are determined by γ and ω_i, respectively. The quantity of object oscillators (A and B in Fig. 4.13(a)) and the quantity of attribute oscillators (1 to 4 in Fig. 4.13(a)) are defined by n_0 and n_a, respectively. The respective coupling of the two object oscillators with each attribute oscillator (cf. Fig. 4.14) is represented by the coupling matrix g_M (n_0 x n_a). The coupling matrix is comprised of the coupling strength of every single memristive device in the network. Thus, it contains the information regarding whether a memristive device that connects two oscillators is in the HRS (low coupling strength) or in the LRS (high coupling strength). A device in the HRS has no influence on the attached self-sustained oscillators n_0, which follow their natural frequencies, while the device being in the LRS leads to frequency synchronization and phase-locking of the adjacent oscillators. An approach to addressing the temporal binding problem is thus addressed via the resistance state of each individual memristive device and the possible resulting oscillation [16].

The change in the resistance state is caused by a separate sensory input at each memristive synapse, thus fulfilling the illustration of Fig. 4.13. These sensory inputs are summarized in a sensory input matrix S that considers each memristive coupling with its switching probability, which can be described as follows [16]:

$$\frac{dg_M^{ij}}{dt} = S(\theta_j^i(N, V)), \quad i = 1, ..., n_0, \quad j = 1, ..., n_a \tag{4.15}$$

with the voltage pulse train θ_j^i induced by the sensory input to the memristive device m_{ij} that connects the object oscillator i to the attribute oscillator j. The input matrix S contains the pulse number N and the voltage amplitude V of the distribution function $f_N(V)$ of each memristive synapse, calculated according to Eq. (4.12). Thus, the matrix S contains a coding of attention in the form of voltage pulse trains [16].

4.3.6 Two Memristively Coupled Van der Pol Oscillators

Two experimentally realized memristively coupled self-sustained relaxation oscillators are depicted in Fig. 4.16(b). The simplified representation in Fig. 4.16(a) illustrates the concept behind the circuit: The resistance state of the memristive device changes as a function of attention, which is coded into a certain number of voltage pulses that are applied to the memristive device. This leads to the following procedure: In the beginning, the memristive device is in its HRS, which leads to an oscillating of the uncoupled neuronal oscillators at their natural frequencies f_1 and f_2. The amplitude of the coupling gate pulses of both oscillators was selected in such a manner that they were below the threshold value θ_{thr} of the memristive device according to Eq. 4.12, preventing undesirable switching of the device. Thus, no autonomous synchronization occurred as a result of the coupling gate pulses, as was the case in Sec. 4.2.1. According to Eq. (4.15), the signal S contains the information concerning the voltage pulse train $\theta_{(N,V)}$; thus, the level of attention is encoded in the pulse number. The information concerning the voltage pulse train has a decisive influence on the switching probability of the memristive device (Sec. 4.3.2). As a result, a high number of applied voltage pulses within a certain time interval leads to a transition of the memristive device from the HRS to the LRS. This results in frequency synchronization and phase-locking of the neuronal oscillators [16].

To realize two memristively coupled self-sustained oscillators capable of stochastic plasticity, relaxation (van der Pol) oscillators based on a PUT (Sec. 3.8) were employed, as shown in the blue and red frames in Fig. 4.16(b). Memristive coupling according to Eq. (4.12) was realized via an Ag-doped TiO_{2-x} memristive device (the red frame in Fig. 4.16(b)) that

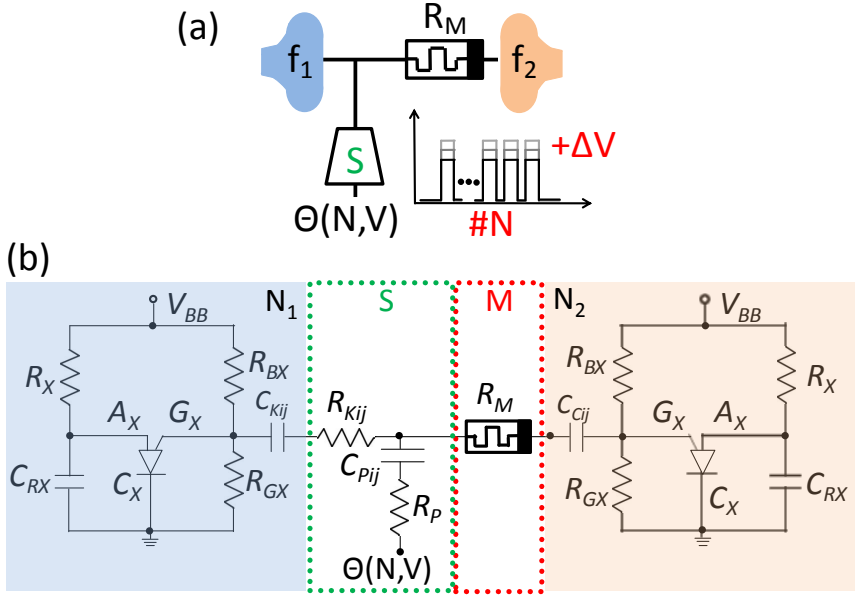

Figure 4.16 Two memristively coupled self-sustained relaxation oscillators: (a) Sketch of two neuronal oscillators connected by a memristive synapse. A local sensory input S influences the resistance state of the device R_M depending on the information $\theta(N, V)$. (b) Set-up of the electrical implementation of two memristively coupled relaxation oscillators based on a PUT. The sensory input was realized by a pulse generator V_P with a series resistor R_P containing the information $\theta(N, V)$ of the voltage pulse train (number, amplitude, and width) [16]. [Adapted from [16] / CC BY-NC 4.0.]

connected the gate terminals G_X of both oscillators. The two capacitors $C_K = C_C$ ensured a DC potential decoupling. While the integration of stochastic plasticity in the circuit was realized by the voltage pulse train $\theta(N, V)$ of the input signal S being applied directly to the memristive device R_M. The subcircuit of the input signal S (the green frame in Fig. 4.16) consisted of two linear resistors R_P and R_K, ensuring that the required voltage amplitude of the pulse train θ was generated by the pulse generator. Furthermore, capacitor C_P compensated for the offset voltage of the pulse generator during the generation of the voltage pulse train. This subcircuit enabled a switching of the memristive device from HRS to LRS, meaning that the learning rule discussed in Sec. 4.3.2 is accomplished [16].

4.3.7 Synchronization of Two Van der Pol Oscillators

In order to study the phase and frequency dynamics of the two memristively coupled oscillators, the gate voltages of the pre-oscillator $V_{G,pre}$ (N_1) and the post-oscillator $V_{G,post}$ (N_2) were simultaneously recorded with a Tektronix TDS 7104 oscilloscope and plotted as $V_{01} - V_{G1}$ and $V_{02} - V_{G2}$ in the upper graph of Fig. 4.17(a). The offset voltages $V_{01,2}$ are 0.25 V; the voltage drop across the memristive device is shown in the lower graph of Fig. 4.17(a). The resulting voltage V_M across the memristive device is defined by the voltage divider R_M and R_{G2}. Initially, both self-sustained oscillators oscillated at their natural frequencies (f_1 = 190 Hz and f_2 = 267 Hz). During this initial phase, the positive gate pulses applied to the memristive device by oscillator 1 were so weak ($V_{G,pre}$ = 0.25 V) that they were below the threshold value of the device and therefore had no influence on it. Thereafter, the learning phase begins, which is coded in seven pulses that were generated by the pulse generator and applied to the memristive with an amplitude of V_M = 2.2 V. This led to a switching of the memristive device from the HRS to the LRS after the fifth pulse, which can be clearly seen in the reduction of the voltage pulses V_M across the device due to the voltage divider. The switching effected a phase and frequency synchronization of the oscillators due to an adjustment of the frequency of oscillator 1 to the frequency of oscillator 2 (cf. Sec. 3.8) [16]. The synchronization phenomenon can be seen more clearly when considering the phase portrait in Fig. 4.17(b).

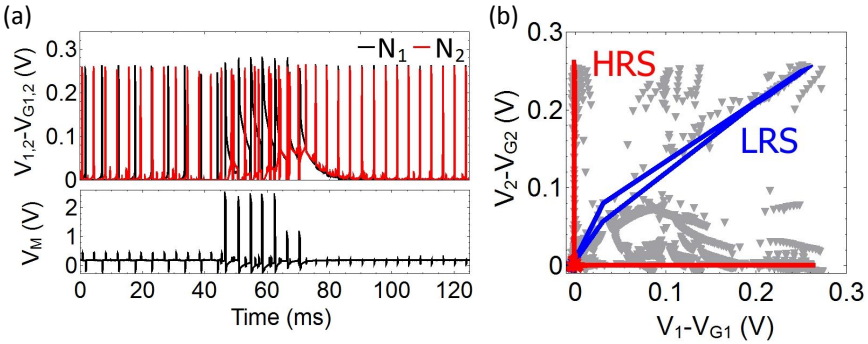

Figure 4.17 Synchronization of two coupled oscillators: (a) The voltage courses taken at the gate terminals show a desynchronous, a learning, and a synchronous phase. The voltage across the memristive device indicates a learning phase with seven successive pulses. (b) The phase plot of the synchronization process demonstrates a digital course of the gate pulses in the HRS of the device, and a hysteresis progression of almost a straight line in the LRS of the device. The independent states in between, marked with gray dots, mostly indicate the learning phase [16]. (cf. Ch. A) [Adapted from [16] / CC BY-NC 4.0.]

Therein, $V_{01} - V_{G1}$ is shown as a function of $V_{02} - V_{G2}$. The red and blue lines illustrate the dependency on the two oscillators when the memristive device is in the HRS or the LRS, respectively. Three different points illustrate the digital character of the gate pulses while the device was in its HRS. Whereas the line-like hysteresis reinterprets a typical behavior for frequency synchronization and phase-locking, which indicates that the memristive device was in its LRS. The independent states in between, marked with gray dots, largely indicate the learning phase [16].

4.3.8 Desynchronization of Two Van der Pol Oscillators

In order to be able to switch between the different states illustrated in Fig. 4.13, a desynchronization phase is essential. Thus, the synchronized state must be transferred back to an uncoupled network by transferring the memristive device from the LRS to the initial HRS. In order to obtain a

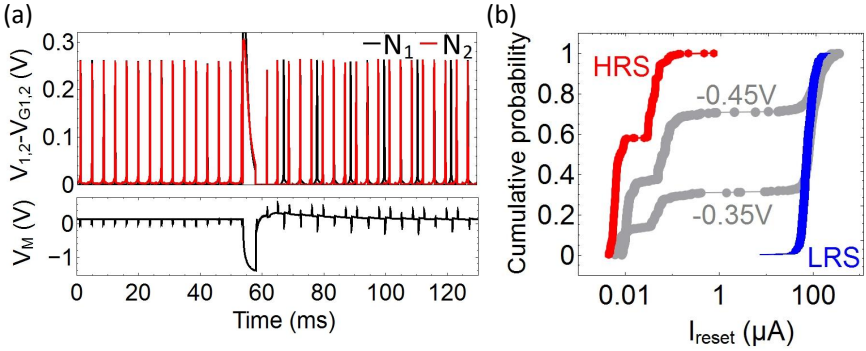

Figure 4.18 Desynchronization of two coupled oscillators: (a) The voltage courses taken at the gate terminals show a synchronous, a learning, and a desynchronous phase. The voltage across the memristive device indicates a reset phase with a single negative voltage pulse. (b) The cumulative probability as a function of the reset current for 795 negative voltage sweeps [16]. (cf. Ch. A) [Adapted from [16] / CC BY-NC 4.0.]

more precise picture of the reset process, 795 voltage sweeps were applied to the memristive device and the reset behavior was examined more closely, as shown in Fig. 4.18(b). The cumulative distribution of the reset current I_{reset} of the memristive device is shown as a function of the sweep voltage. The distribution is given for the LRS and HRS of the device, as well as for the sweep voltages -0.35 V and -0.45 V. As a result, the device resistance in the LRS was found between 1 kΩ - 13 kΩ, while the resistance state for 99.75 percent of all of the measured sweeps was greater than 1 MΩ.

Both states (HRS and LRS) represent already known resistance values for an Ag-doped TiO_{2-x} memristive device. However, in the case of negative voltage sweep values (cf. gray curves in Fig. 4.18(b)) between the HRS and LRS, multilevel intermediate states were found to exist during the reset process. The HRS of the device is reached with a higher probability with increasingly negative voltages. However, small negative reverse voltages are sufficient to reset the device from LRS to HRS. This approach was used via the circuit design depicted in Fig. 4.18(a), wherein

a single negative input signal $\theta(N, V)$ was applied by the subcircuit S to reset memristive device. The procedure is shown in Fig. 4.18(a) for two memristively coupled van der Pol oscillators. Here, during the first 53 ms, the memristive device was in the LRS, which led to a frequency synchronization and phase-locking of both oscillators. A negative voltage pulse with an amplitude of -1.6 V and a pulse width of 5 ms was applied via the pulse generator at the subcircuit S to the oscillator network. This led to a resetting of the device from LRS to the HRS. Therefore, the decreased coupling strength resulted in a desynchronous system, with the two self-sustained oscillators once again following their natural frequencies [16].

4.3.9 Memristively Coupled Network

The bistable illustration in Fig. 4.13 is emulated by a system of six van der Pol oscillators coupled via eight memristive devices, which is an extension to the network depicted in Fig. 4.16. This system was realized as a neuromorphic electrical circuit, as shown in Fig. 4.19. The circuit was comprised of two object oscillators n_0 (either the body of the hippo $\mathrm{vdP_A}$ or the background $\mathrm{vdP_B}$) and four attribute oscillators n_a (either the legs of the hippo $\mathrm{vdP_{1,2}}$ or the hippos feet $\mathrm{vdP_{3,4}}$). The object oscillators were coupled to every attribute oscillator via an Ag-doped $\mathrm{TiO_{2\text{-}x}}$ memristive device, denoted as m_{n_0,n_a}. The initial position of the network is represented in the form of a diagram in Fig. 4.19(a), in which the memristive devices are all in the HRS and thus allow all of the oscillators to follow their natural frequencies. During the learning phase, depending on where the attention is drawn - which is coded into a voltage pulse train $\theta(N, V)$ at the respective input subcircuit S - a transition of the respective memristive device to the LRS takes place, as indicated in green in Fig. 4.19(b).

To elaborate, the gate voltages of the self-sustained oscillators are shown in Fig. 4.20 for the particular case of Fig. 4.13(b). In the beginning, the six oscillators followed their natural frequencies, which resulted in a desynchronous system. The learning phase effected an association of the object oscillator A with the attribute oscillators 1 and 2, whereas the attribute oscillators 3 and 4 were linked to the object

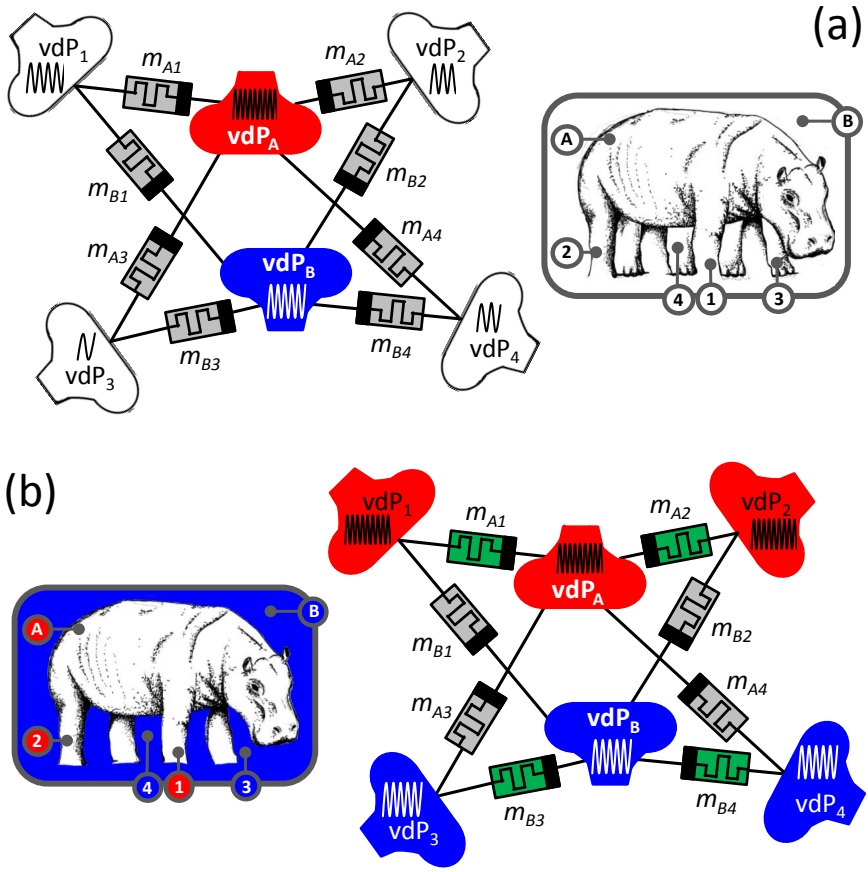

Figure 4.19 Sketch of the implemented oscillator circuit to deal with the binding problem: (a) Illustration of the system of six coupled van der Pol oscillators via eight memristive devices. All oscillators follow their natural frequency due to the HRS of all memristive devices, indicated by the gray color. The corresponding illustration from Fig. 4.13 is shown next to it. (b) The same circuit sketch as (a), but after the learning phase, which leads to a switching of four memristive devices, indicated by green color, and to the synchronization of the respectively oscillators. The picture of the hippo shows the corresponding perception [16]. [Adapted from [16] / CC BY-NC 4.0.] [A similar drawing is published by Shepard [196, 197].]

oscillator B. The increased attention is realized by a voltage pulse train $\theta(N, V)$ of eight pulses with an amplitude of 1.8 V, calculated according to Eq. (4.15), at the subcircuits S of the following memristive devices: m_{A1}, m_{A2}, m_{B3}, and m_{B4} (cf. Fig. 4.19(b)). According to Eq. (4.15), this number of applied pulses corresponds to a high level of activity, meaning that partial synchronization of the network oscillators due to memristive resistance changes could be observed. As shown in Fig. 4.20, a frequency synchronization and phase-locking of vdP_A were achieved with oscillators 1 and 2, and a frequency synchronization and phase-locking of vdP_B were obtained with oscillators 3 and 4 after the learning phase [16].

4.3.10 Context-Dependent Oscillator Network

An oscillator network can account for a context-dependent and transient behavior, which becomes clear when considering the different illustrations in Fig. 4.21. The different illustrations demonstrate the significant property selectivity of the binding problem since perception of the image varies the moment that the attention paid to the picture varies in favor of other aspects. The memristive device meets this challenge when emulating a shift in attention with respect to Eq. (4.12). Here, the number of voltage pulses within a pulse train θ applied to the device is used as a means to code the attention paid to the particular attributes identified in Eq. (4.15). An attention shift corresponds to a shift in the switching probability in favor of the corresponding memristive device by applying the voltage pulse activity to that device. This leads to a synchronization of other oscillators in the network depicted in Fig. 4.19, meaning that different self-organized sub-networks can be realized depending on the context of perception, as shown in Fig. 4.21.

The angular frequency curves of the three possible perceptions of the illustration from Fig. 4.13 are shown. At the beginning, all three oscillator networks are in a desynchronous state due to the memristive devices being in a high-ohmic state. Thus, each of the six oscillators follows its natural angular frequency until the learning phase. However, the learning phase leads to a differentiation of the three perceptions as a function of attention. This is achieved by means of pulse trains

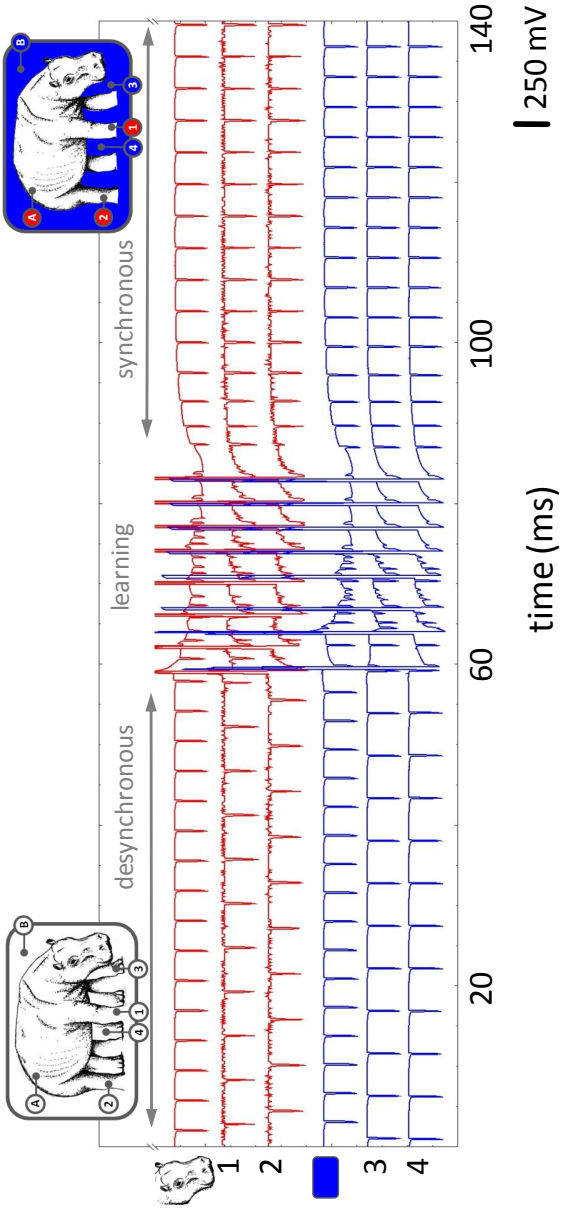

Figure 4.20 Memristively coupled oscillators emulate the binding problem: The voltage courses taken at the gate terminals of the six van der Pol oscillators show a desynchronous, a learning, and a synchronous phase due to eight voltage pulses [16]. (cf. Ch. A). [Reproduced from [16] / CC BY-NC 4.0.] [A similar drawing is published by Shepard [196, 197].]

$\theta(N, V)$ with eight positive voltage pulses with an amplitude of 1.85 V being applied to the corresponding memristive device, which thus has a switching probability of 0.8 due to $\theta(N, V)$ (cf. Fig. 4.15(c)). After the learning phase, different sub-networks are formed, representing the mutually exclusive cases from Fig. 4.13. In Fig. 4.21(a), the object $\mathrm{vdP_A}$ (the body of the hippo) synchronizes in phase and frequency with both attribute oscillators 1 and 2 (the red curves), while the background, represented by $\mathrm{vdP_B}$ is bound to the attribute oscillators 3 and 4 (the blue curves). The reverse case is shown in Fig. 4.21(b), in which the attribute oscillators 1 and 2 are bound to the background (oscillator B), whereas the attribute oscillators 3 and 4 are associated with the body (oscillator A). It may be possible that attributes are neither associated with the background nor with the body, as it is the case in Fig. 4.21(c). In this case, the attribute oscillator 3 (foot) will continue to follow its natural frequency even though a learning phase took place. Thus, the attention was not fixed, which can be very well represented with a memristive device due to its stochasticity. The switching probability is 0.8, due to a pulse train of eight pulses [16].

4.3.10.1 Discussion

Memristively coupled van der Pol oscillators demonstrate the ability to integrate plasticity in a model of learning-induced synchronization in a neuronal network. For this purpose, the ability of non-volatile memristive devices was used to establish a long-lasting connection between objects and attributes in order to form a unified perception. In order to switch between individual states of perception, it is necessary to have an equivalent to the partial parts of the temporal sensory input, which is accomplished by the inclusion of higher-level assemblies. The allocation among assembly is necessary since the brain is an active and dynamic system that produces a modified uniform perception by combining different sensory modalities from a complex environment. The brain's computing process has three levels of description: selective attention, segregation, and integration [16, 20, 22, 203].

Selective attention is a fundamental property of the brain that is intended to cope with the enormous amount of data taken from the

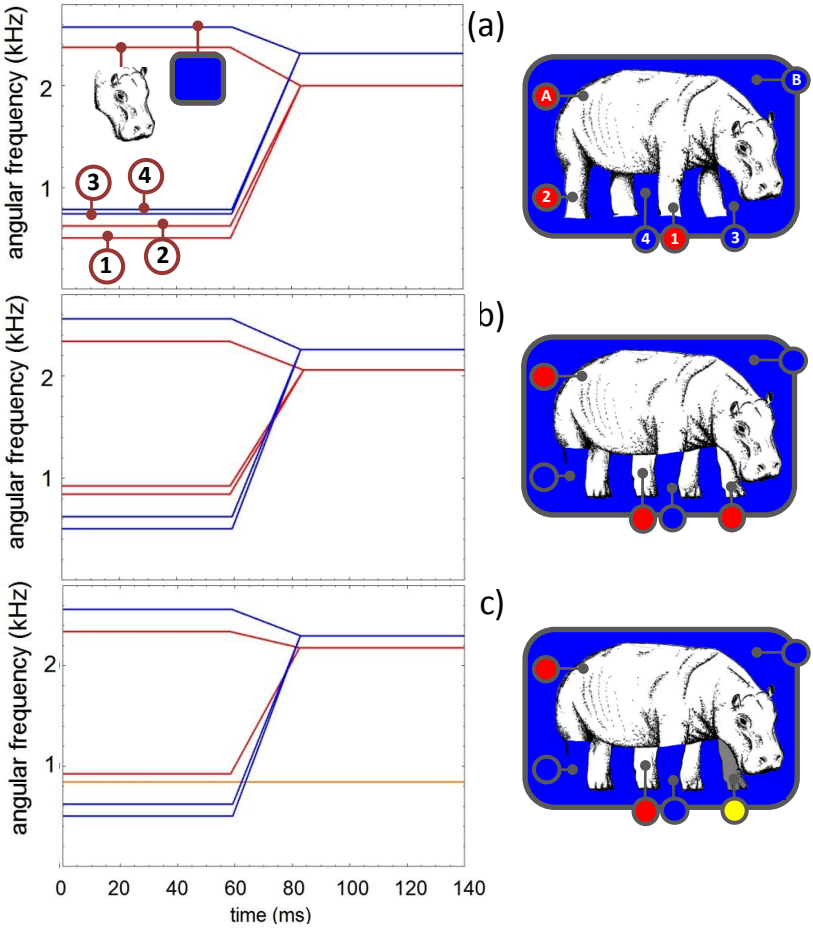

Figure 4.21 Context-dependent and transient oscillator network: A shift by attention was achieved by shifting the input information $\theta(N, V)$ of the respective input signal S at the memristive device. (a) Frequency synchronization takes place between vdP_A and $vdP_{1,2}$ as well as between vdP_B and $vdP_{3,4}$. (b) Frequency synchronization takes place between vdP_B and $vdP_{1,2}$ as well as between vdP_A and $vdP_{3,4}$. (c) Oscillator 3 follows its natural frequency even after the learning phase [16]. (cf. Ch. A). [Adapted from [16] / CC BY-NC 4.0.] [A similar drawing is published in [196, 197].]

environment via the receptive fields. Thus, attention is paid only to those items that are accepted as essential for the current task at hand. This approach, at the neuronal level, assumes that sensory neurons construe attention as an input signal encoded in neuronal activity patterns. Therefore, in this work, the model of the number of voltage pulses within a pulse train was used to code attention. By varying the number of voltage pulses, the probability of switching of the memristive device is also changed, as shown in Fig. 4.15(c). Thus, the first step is to perceive relevant information from the environment, as opposed to copying it [16].

In the second phase, segregation of selective information received from the environment proceeds by means of dividing partial aspects of perception into assemblies (motifs), such as color or shape. For this propose, neural oscillators are used. The strategy involves using relaxation oscillators with diverse natural frequencies, which can be described by a van der Pol equation, to emulate the oscillators. The differences in the natural frequencies are crucial in distinguishing between desynchronous and synchronous phases. A desynchronous phase in the oscillator network can always been attained by resetting the memristive device, which can occur in two different ways: Either every single memristive device can be reset globally or a locally generated pulse at the subcircuit S can cause a change from the LRS to the HRS, as shown in Fig. 4.18(a). Furthermore, the continuous intermediate reset process, including stochasticity, can be exploited. It is worth mentioning that it is not sufficient to have different phases of the oscillators; the natural frequencies must also differ, as, otherwise, the oscillator system will remain in phase and frequency synchronization [16, 191]

Finally, the integration of assemblies occurs over a temporal binding. This is realized with a memristively coupled oscillator network, which uses the stochasticity of memristive devices to implement the frequency and phase synchronization of the relaxation oscillators [16].

In the following section, a fundamental discussion of the perception of the informative environment can be found. The most widely accepted model involves defining perception in the brain as an interplay of the separate functions involved in processing motion, depth/form, and

color [16, 203]. Knowledge of this topic is based on the measured increased neuronal activity of different assemblies in the visual cortex that occurs in reaction to the different attributes of an object. Based on the example shown in Fig. 4.13, a uniform perception is determined from a biological point of view through coherent states using different visual areas. However, the model used may not meet these requirements: The information transfer from the sensory input to the local level of the oscillator synchronization was achieved by means of the local input S. A separate control of each coupling takes place, in which the sensor input is directly encoded into the number of voltage pulses. However, the model represents a great simplification of the brain, which is able to select relevant information from a multitude of information [16].

The extraordinary ability of the brain to handle complex processing would have to be technically realized by means of a global selection mechanism that filters out using specific processes at the higher-level in order to obtain the desired information (i.e. down-streaming of information). However, it should be noted that there are clear advantages in the technical implementation of the memristive model, by which a basis was laid for more complex neuromorphic circuits with cognitive features, including the reductionist strategy. Reduction remains an important point since the brain must process several actions simultaneously during the visual perception of diverse objects. This naturally results in a large number of binding problems for each object and the interactions between them [16, 18, 203]. The challenge of a communication strategy can be addressed with neuronal synchronization and a local memory, in which one differentiates between neural communication and plasticity in the context of synchronization [16, 191]. This makes it clear that the memory process cannot be considered separately but is instead a part of the binding problem, as is reflected in the memristive model. An extension of the circuit presented here to include devices from the field of memristive systems (Sec. 2), such as a memcapacitor or meminductors (Sec. 2.2) [127], would allow for a more precise representation of biology. Thus, this memristive model may only represents the beginning of the development of much larger neuromorphic circuits [16].

Conclusion

Research into the brain's cortex have led to the finding that different areas of the brain are responsible for diverse visual stimuli, such as motion, depth, form, and color. It is assumed that neural oscillation related to synchronization mechanisms within a topology of the neural network is the key to bind these areas together into a single unit in the brain, which is referred to as the "binding problem". In this thesis, dynamic electronic neuromorphic circuits with memristive devices were investigated in a bio-inspired manner in order to finally address the binding problem.

Initially, the basic electrophysiological properties of a neuron were emulated with the use of a memristive spiking neuron circuit. A VO_2-based NDR (i.e. an electronic element exhibiting a "negative device resistance") and an Ag-doped TiO_{2-x} memristive device are the key components of the circuit and enable the emulation of the following neural properties: spike coding, frequency adaptation in real time, and an action-potential-like shape that included a refractory period. The implemented subcircuit, comprising a memristive device and a capacitive divider, demonstrates the characteristic behaviors of a memcapacitance.

Abstraction from the cellular behavior of a spiking neuron to the more general form of oscillation was achieved by means of a PUT-based relaxation (van der Pol) oscillator. The coupling of two of these self-sustained van der Pol oscillators via a single memristive device demonstrates the biological properties of synchronization in conjunction with memory. For the coupling, either an Ag-doped TiO_{2-x} memristive device or a double barrier memristive device were selected, which respectively demonstrated digital or analogue continuous resistive switching. Both oscillator circuits revealed phase-locking and frequency synchronization after a resistive switching of the device. The transition from the desynchronous state (over an intermediated state in the case of the double barrier memristive device) to a synchronous state occurred autonomous due to the pulse-

coupling. An extension of two coupled oscillators to a network of six coupled oscillators with an integrated local plasticity model was realized to address the binding problem. The transient, context-dependent, and self-organized network that exploits eight Ag-doped TiO_{2-x} memristive devices demonstrates a model of neural synchrony by using local memories to store and to integrate transient neural activity simultaneously. For this purpose, partial phase-locking and frequency synchronization took place in the oscillator network in order to emulate different perceptions of a bistable image.

A Circuit Parameter

Figure 2.12:

C_2 = 0.068 µF, ω = 3141.6 Hz

Figures 3.8(b), 3.10(a):

V_B = -3.5 V, C_0 = 68 nF, R_1 = 47 kΩ, R_2 = 10 kΩ

Figure 3.10(b):

V_B = -3.5 V, C_0 = 68 nF

Figures 3.11, 3.12, 3.13:

V_B = -5.5 V, R_1 = 1 MΩ, R_2 = 47 kΩ, C_1 = 0.165 µF, C_2 = 0.68 µF

Figure 3.14(b):

V_{BB} = 25 V, R_1 = 100 kΩ, R_B = 10 kΩ, R_G = 1 kΩ, C_{R1} = 0.15 µF

Figure 3.15:

R_G = 1 kΩ, R_C = 100 Ω

Figure 3.16:

V_K = 5.5 V, R_1 = 22 kΩ, R_B = 470 Ω, R_G = 22 kΩ, C_{R1} = 0.047 µF

Figure 3.17:

V_K = 2.4 V, R_1 = 200 kΩ, R_B = 33 kΩ, R_G = 33 kΩ, R_J = 22 kΩ, R_P = 1 MΩ, C_{R1} = 0.047 µF

Figures 4.3, 4.5, 4.6, 4.8:
Parameters for the digital coupling (Sec. 4.2.1):

$V_{BB} = 25$ V, $R_1 = 119.5$ kΩ, $R_2 = 164.2$ kΩ, $R_{B1} = 20.8$ kΩ, $R_{B2} = 39.5$ kΩ, $R_{G1} = 2.37$ kΩ, $R_{G2} = 4.71$ kΩ, $R_{K1} = 10$ kΩ, $R_{K2} = 47$ kΩ, $C_1 = C_2 = 0.15$ µF, $C_{K1} = C_{K2} = 33$ nF

Figures 4.3, 4.10, 4.11, 4.12:
Parameters for the analogue coupling (Sec. 4.2.2):

$V_{BB} = 14.48$ V, $R_1 = 714$ kΩ, $R_2 = 5$ MΩ, $R_{B1} = 22$ kΩ, $R_{B2} = 47$ kΩ, $R_{G1} = 4.45$ kΩ, $R_{G2} = 2.26$ kΩ, $R_{K1} = 1$ kΩ, $R_{K2} = 83.2$ kΩ, $C_1 = 10$ µF, $C_2 = 11$ µF, $C_{K1} = C_{K2} = 10$ µF

Figure 4.9:
Parameters for the measurement of the memristive device R_M:

$R_1 = 1$ kΩ, $R_2 = 10$ kΩ, $R_3 = 10$ kΩ, $R_g = 1$ MΩ
Parameters for the measurement of the resistor R_{K1}:

$R_1 = 10$ kΩ, $R_2 = 1$ kΩ, $R_3 = 100$ kΩ, $R_g = 1$ MΩ

Figure 4.17:

$V_{BB} = 9.25$ V, $V_P = 20$ V, $R_P = 10$ kΩ, $R_{Kij} = 470$ Ω, $C_{Pij} = 1$ µF, $C_{Kij} = C_{Cij} = 0.47$ µF, $R_{BX} = 22$ kΩ, $R_{GX} = 1$ kΩ, $C_{RX} = 0.68$ µF, $R_1 = 460$ kΩ, $R_2 = 325$ kΩ

Figure 4.18:

$V_{BB} = 9.25$ V, $V_P = -4$ V, $R_P = 2.2$ kΩ, $R_{Kij} = 470$ Ω, $C_{Pij} = 1$ µF, $C_{Kij} = C_{Cij} = 0.47$ µF, $R_{BX} = 22$ kΩ, $R_{GX} = 1$ kΩ, $C_{RX} = 0.68$ µF, $R_1 = 460$ kΩ, $R_2 = 325$ kΩ

Figures 4.20, 4.21:

$V_{BB} = 9.25$ V, $V_P = 20$ V, $R_P = 10$ kΩ, $R_{Kij} = 470$ Ω, $C_{Pij} = 1$ µF, $C_{Kij} = C_{Cij} = 0.47$ µF, $R_{BX} = 22$ kΩ, $R_{GX} = 1$ kΩ, $C_{RX} = 0.68$ µF, $R_1 = 472$ kΩ, $R_2 = 472$ kΩ, $R_3 = 470$ kΩ, $R_4 = 460$ kΩ, $R_A = 325$ kΩ, $R_B = 320$ kΩ

B Simulation Parameter

Figures 4.7, 4.8:

$\alpha_1 = 3.5$, $\alpha_2 = 4.8$, $\beta_{1,2} = 0.1$, $\gamma_{1,2} = 3.0$, $m_0 = 0.01$, $m_1 = 0.1$

Figure 4.10:

$R_{LRS} = 249$ kΩ, $R_{diff} = 66$ kΩ, and $\alpha = 4.7$ ms^{-1}

C Scientific Vita

Marina Ignatov

Date of birth:	08.06.1987
Place of birth:	Alma-Ata (Kasachstan)
Nationality:	German

Education:

07/2007	Abitur, Dahlmannschule, Bad Segeberg

Course of study:

10/2007 – 06/2011	Industrial Engineering at the Christian-Albrechts-Universität zu Kiel (Bachelor of Science, 8 Semester)
10/2011 – 10/2013	Industrial Engineering at the Christian-Albrechts-Universität zu Kiel (Master of Science, 4 Semester)
09/2012 – 01/2013	Visiting student at University of Nottingham (UK) (1 Semester)

Work experience:

Since 11/2013	Scientific staff member of the chair of Nanoelectronics (Prof. Kohlstedt) at Christian-Albrechts-Universität zu Kiel

List of Publications during this Thesis

1. Publication

M. Ziegler, M. Hansen, M. Ignatov, and H. Kohlstedt,
Building memristive neurons and synapses,
In Circuits and Systems (ISCAS), 2014 IEEE International Symposium on, 1066-1069, (1-5 June 2014).
doi: 10.1109/ISCAS.2014.6865323

2. Publication

M. Ignatov, M. Ziegler, M. Hansen, A. Petraru, and H. Kohlstedt,
A memristive spiking neuron with firing rate coding,
Frontiers in Neuroscience **9**, 376 (20 October 2015).
doi: 10.3389/fnins.2015.00376

3. Publication

M. Ignatov, M. Hansen, M. Ziegler, and H. Kohlstedt,
Synchronization of two memristively coupled van der Pol oscillators,
Applied Physics Letters **108**(8), 084105 (25 February 2016).
doi: 10.1063/1.4942832

4. Publication

K. Ochs, M. Ziegler, E. Hernandez-Guevara, E. Solan, M. Ignatov,
M. Hansen, M. S. Gill, and H. Kohlstedt,
Anticipation of digital patterns,
Int. Journal of Circuit Theory and Applications, 0098988 (30 June 2017).
doi: 10.1002/cta.2381

5. Publication

M. Ignatov, M. Ziegler, M. Hansen, and H. Kohlstedt,
Memristive stochastic plasticity enables mimicking of neural synchrony: Memristive circuit emulates an optical illusion,
Science Advances **3**(10), e1700849 (25 October 2017).
doi: 10.1126/sciadv.1700849

Bibliography

[1] E. Bullmore and O. Sporns, *Complex brain networks: graph theoretical analysis of structural and functional systems*, Nature Reviews Neuroscience **10**, 186–198 (2009).

[2] M. F. Bear and R. C. Malenka, *Synaptic plasticity: LTP and LTD*, Current Opinion in Neurobiology **4**, 389–399 (1994).

[3] G. Buzsaki, *Rhythms of the Brain*, Oxford University Press, 2006.

[4] E. D. Adrian, *The impulses produced by sensory nerve endings*, The Journal of Physiology **61**, 49–72 (1926).

[5] E. D. Adrian, *The basis of sensation*, Christophers; London, 22 Berners Steeet, W. 1, 1928.

[6] W. Maass and C. M. Bishop, *Pulsed Neural Networks*, MIT Press, 2001.

[7] H. B. Barlow, *Possible principles underlying the transformations of sensory messages*, MIT Press, 1961.

[8] S. B. Laughlin, *The role of sensory adaptation in the retina*, Journal of Experimental Biology **146**, 39–62 (1989).

[9] W. Gerstner and W. M. Kistler, *Spiking Neuron Models: Single Neurons, Populations, Plasticity*, Copyright Cambridge University Press 2002, 2002.

[10] M. Ignatov, M. Ziegler, M. Hansen, A. Petraru, and H. Kohlstedt, *A memristive spiking neuron with firing rate coding*, Frontiers in Neuroscience **9** (2015).

[11] D. Natelson, *Condensed-matter physics: A solid triple point*, Nature **500**, 408–409 (2013).

[12] C. Zamarreño-Ramos, L. A. Camuñas-Mesa, J. A. Pérez-Carrasco, T. Masquelier, T. Serrano-Gotarredona, and B. Linares-Barranco, *On Spike-Timing-Dependent-Plasticity, Memristive Devices, and Building a Self-Learning Visual Cortex*, Frontiers in Neuroscience **5** (2011).

[13] G.-q. Bi and M.-m. Poo, *Synaptic Modifications in Cultured Hippocampal Neurons: Dependence on Spike Timing, Synaptic Strength, and Postsynaptic Cell Type*, Journal of Neuroscience **18**, 10464–10472 (1998).

[14] T. V. P. Bliss and T. Lømo, *Long-lasting potentiation of synaptic transmission in the dentate area of the anaesthetized rabbit following stimulation of the perforant path*, The Journal of Physiology **232**, 331–356 (1973).

[15] M. Ziegler, *Memristive Devices For Neuronal Systems*, postdoctoral thesis, Christian-Albrechts-Universität zu Kiel, Faculty of Engineering, 2015.

[16] M. Ignatov, M. Ziegler, M. Hansen, and H. Kohlstedt, *Memristive stochastic plasticity enables mimicking of neural synchrony: Memristive circuit emulates an optical illusion*, Science Advances **3**, e1700849 (2017).

[17] D. O. Hebb, *The organization of behavior: A neuropsychological approach*, John Wiley & Sons, 1949.

[18] W. Singer and C. M. Gray, *Visual feature integration and the temporal correlation hypothesis*, Annual review of neuroscience **18**, 555–586 (1995).

[19] P. Andersen, *The Hippocampus Book*, Oxford University Press, USA, 2007.

[20] O. Sporns, *Networks of the Brain*, MIT Press, 2010.

[21] E. R. Kandel et al., *Principles of neural science*, volume 4, McGraw-hill New York, 2000.

[22] E. R. Kandel, *In Search of Memory: The Emergence of a New Science of Mind*, W. W. Norton & Company, 2007.

[23] C. von der Malsburg, *The What and Why of Binding*, Neuron **24**, 95–104 (1999).

[24] C. von der Malsburg, The Correlation Theory of Brain Function, in *Models of Neural Networks*, pp 95–119, Springer New York, New York, NY, 1994.

[25] H. Eichenbaum, *Thinking about brain cell assemblies*, Science **261**, 993–995 (1993).

[26] P. J. Uhlhaas, G. Pipa, B. Lima, L. Melloni, S. Neuenschwander, D. Nikolić, and W. Singer, *Neural synchrony in cortical networks: history, concept and current status*, Frontiers in Integrative Neuroscience **3** (2009).

[27] G. Buzsáki and W. Freeman, *Editorial overview: Brain rhythms and dynamic coordination*, Current Opinion in Neurobiology **31**, v–ix (2015).

[28] J. Fell, *Identifying neural correlates of consciousness: The state space approach*, Consciousness and Cognition **13**, 709–729 (2004).

[29] A. K. Engel, P. Fries, P. König, M. Brecht, and W. Singer, *Temporal Binding, Binocular Rivalry, and Consciousness*, Consciousness and Cognition **8**, 128–151 (1999).

[30] B. J. He, *Scale-free brain activity: past, present, and future*, Trends in Cognitive Sciences **18**, 480–487 (2014).

[31] L. M. Ward, *Synchronous neural oscillations and cognitive processes*, Trends in cognitive sciences **7**, 553–559 (2003).

[32] P. Fries, *A mechanism for cognitive dynamics: neuronal communication through neuronal coherence*, Trends in Cognitive Sciences **9**, 474–480 (2005).

[33] A. K. Engel, P. Fries, and W. Singer, *Dynamic predictions: Oscillations and synchrony in top–down processing*, Nature Reviews Neuroscience **2**, 704–716 (2001).

[34] W. Singer, *Neuronal Synchrony: A Versatile Code for the Definition of Relations?*, Neuron **24**, 49–65 (1999).

[35] A. Engel, *Role of the temporal domain for response selection and perceptual binding*, Cerebral Cortex **7**, 571–582 (1997).

[36] X.-J. Wang, *Neurophysiological and Computational Principles of Cortical Rhythms in Cognition*, Physiological Reviews **90**, 1195–1268 (2010).

[37] P. Dayan and L. F. Abbott, *Theoretical neuroscience*, volume 806, Cambridge, MA: MIT Press, 2001.

[38] F. C. Hoppensteadt and E. M. Izhikevich, *Weakly Connected Neural Networks*, Springer Science & Business Media, 2012.

[39] G. V. Osipov, J. Kurths, and C. Zhou, *Synchronization in Oscillatory Networks*, Springer Science & Business Media, 2007.

[40] N. W. Schultheiss, A. A. Prinz, and R. J. Butera, *Phase Response Curves in Neuroscience: Theory, Experiment, and Analysis*, Springer Science & Business Media, 2011.

[41] U. Ernst, K. Pawelzik, and T. Geisel, *Synchronization Induced by Temporal Delays in Pulse-Coupled Oscillators*, Physical Review Letters **74**, 1570–1573 (1995).

[42] R. C. Hinz, P. Hövel, and E. Schöll, *Transient behavior in systems with time-delayed feedback*, Chaos: An Interdisciplinary Journal of Nonlinear Science **21**, 023114 (2011).

[43] M. Kantner, E. Schöll, and S. Yanchuk, *Delay-induced patterns in a two-dimensional lattice of coupled oscillators*, Scientific Reports **5** (2015).

[44] M. Zeitler, A. Daffertshofer, and C. C. A. M. Gielen, *Asymmetry in pulse-coupled oscillators with delay*, Physical Review E **79** (2009).

[45] G. Indiveri and T. K. Horiuchi, *Frontiers in Neuromorphic Engineering*, Frontiers in Neuroscience **5** (2011).

[46] R. Douglas, M. Mahowald, and a. C. Mead, *Neuromorphic Analogue VLSI*, Annual Review of Neuroscience **18**, 255–281 (1995).

[47] C. Mead, *Analog VLSI and Neural Systems*, Addison-Wesley, 1989.

[48] C. Mead and M. Ismail, *Analog VLSI Implementation of Neural Systems*, Springer Science & Business Media, 2012.

[49] L. Chua, *Memristor-The missing circuit element*, IEEE Transactions on Circuit Theory **18**, 507–519 (1971).

[50] D. B. Strukov, G. S. Snider, D. R. Stewart, and R. S. Williams, *The missing memristor found*, Nature **453**, 80–83 (2008).

[51] R. Tetzlaff, *Memristors and Memristive Systems*, Springer New York, New York, NY, 2014.

[52] S. Gaba, P. Sheridan, J. Zhou, S. Choi, and W. Lu, *Stochastic memristive devices for computing and neuromorphic applications*, Nanoscale **5**, 5872 (2013).

[53] S. H. Jo, T. Chang, I. Ebong, B. B. Bhadviya, P. Mazumder, and W. Lu, *Nanoscale Memristor Device as Synapse in Neuromorphic Systems*, Nano Letters **10**, 1297–1301 (2010).

[54] D. S. Jeong, I. Kim, M. Ziegler, and H. Kohlstedt, *Towards artificial neurons and synapses: a materials point of view*, RSC Advances **3**, 3169 (2013).

[55] M. Ziegler, C. Riggert, M. HanWeaklysen, T. Bartsch, and H. Kohlstedt, *Memristive Hebbian Plasticity Model: Device Requirements for the Emulation of Hebbian Plasticity Based on Memristive Devices*, IEEE Transactions on Biomedical Circuits and Systems **9**, 197–206 (2015).

[56] J. J. Yang, D. B. Strukov, and D. R. Stewart, *Memristive devices for computing*, Nature Nanotechnology **8**, 13–24 (2012).

[57] T. Hasegawa, T. Ohno, K. Terabe, T. Tsuruoka, T. Nakayama, J. K. Gimzewski, and M. Aono, *Learning Abilities Achieved by a Single Solid-State Atomic Switch*, Advanced Materials **22**, 1831–1834 (2010).

[58] T. Ohno, T. Hasegawa, T. Tsuruoka, K. Terabe, J. K. Gimzewski, and M. Aono, *Short-term plasticity and long-term potentiation mimicked in single inorganic synapses*, Nature Materials **10**, 591–595 (2011).

[59] Z. Wang et al., *Memristors with diffusive dynamics as synaptic emulators for neuromorphic computing*, Nature Materials **16**, 101–108 (2016).

[60] R. Berdan, E. Vasilaki, A. Khiat, G. Indiveri, A. Serb, and T. Prodromakis, *Emulating short-term synaptic dynamics with memristive devices*, Scientific Reports **6** (2016).

[61] T. Serrano-Gotarredona, T. Masquelier, T. Prodromakis, G. Indiveri, and B. Linares-Barranco, *STDP and STDP variations with memristors for spiking neuromorphic learning systems*, Frontiers in Neuroscience **7** (2013).

[62] S. Saïghi et al., *Plasticity in memristive devices for spiking neural networks*, Frontiers in Neuroscience **9** (2015).

[63] T. Hasegawa, K. Terabe, T. Tsuruoka, and M. Aono, *Atomic Switch: Atom/Ion Movement Controlled Devices for Beyond Von-Neumann Computers*, Advanced Materials **24**, 252–267 (2012).

[64] D. S. Jeong, K. M. Kim, S. Kim, B. J. Choi, and C. S. Hwang, *Memristors for Energy-Efficient New Computing Paradigms*, Advanced Electronic Materials **2**, 1600090 (2016).

[65] G. W. Burr et al., *Neuromorphic computing using non-volatile memory*, Advances in Physics: X **2**, 89–124 (2017).

[66] T. Aoki, K. Yawata, and T. Aoyagi, *Self-organization of complex networks as a dynamical system*, Physical Review E **91**, 012908 (2015).

[67] T. Aoki and T. Aoyagi, *Co-evolution of phases and connection strengths in a network of phase oscillators*, Physical review letters **102**, 034101 (2009).

[68] A. Arenas, A. Díaz-Guilera, J. Kurths, Y. Moreno, and C. Zhou, *Synchronization in complex networks*, Physics reports **469**, 93–153 (2008).

[69] S. Boccaletti, V. Latora, Y. Moreno, M. Chavez, and D.-U. Hwang, *Complex networks: Structure and dynamics*, Physics reports **424**, 175–308 (2006).

[70] Y. Nishio and A. Ushida, *Spatio-temporal chaos in simple coupled chaotic circuits*, IEEE Transactions on Circuits and Systems I: Fundamental Theory and Applications **42**, 678–686 (1995).

[71] C. Petrarca, S. Yaghouti, and M. de Magistris, *Experimental dynamics observed in a configurable complex network of chaotic oscillators*, Nonlinear Dynamics of Electronic Systems , 203–210 (2014).

[72] C. Posadas-Castillo, C. Cruz-Hernández, and R. López-Gutiérrez, *Experimental realization of synchronization in complex networks with Chua's circuits like nodes*, Chaos, Solitons & Fractals **40**, 1963–1975 (2009).

[73] M. Ignatov, M. Hansen, M. Ziegler, and H. Kohlstedt, *Synchronization of two memristively coupled van der Pol oscillators*, Applied Physics Letters **108**, 084105 (2016).

[74] A. Adamatzky, *Advances in Unconventional Computing, Volume 2*, Springer, 2017.

[75] D. Vodenicarevic, N. Locatelli, F. Abreu Araujo, J. Grollier, and D. Querlioz, *A Nanotechnology-Ready Computing Scheme based on a Weakly Coupled Oscillator Network*, Scientific Reports **7**, 44772 (2017).

[76] L. Glass, *Synchronization and rhythmic processes in physiology*, Nature **410**, 277–284 (2001).

[77] M. Valencia, M. A. Pastor, M. A. Fernández-Seara, J. Artieda, J. Martinerie, and M. Chavez, *Complex modular structure of large-scale brain networks*, Chaos: An Interdisciplinary Journal of Nonlinear Science **19**, 023119 (2009).

[78] M. de Magistris, M. di Bernardo, and C. Petrarca, *Experiments on synchronization in networks of nonlinear oscillators with dynamic links*, Nonlinear Theory and Its Applications, IEICE **4**, 462–472 (2013).

[79] L. Glass and M. C. Mackey, *From Clocks to Chaos: The Rhythms of Life*, Princeton University Press, 1988.

[80] D. J. Watts and S. H. Strogatz, *Collective dynamics of 'small-world' networks*, Nature **393**, 440–442 (1998).

[81] A. T. Winfree, *Biological rhythms and the behavior of populations of coupled oscillators*, Journal of Theoretical Biology **16**, 15–42 (1967).

[82] L. O. Chua and S. M. Kang, *Memristive devices and systems*, Proceedings of the IEEE **64**, 209–223 (1976).

[83] R. Waser, R. Dittmann, G. Staikov, and K. Szot, *Redox-Based Resistive Switching Memories - Nanoionic Mechanisms, Prospects, and Challenges*, Advanced Materials. **21**, 2632–2663 (2009), (Copyright Wiley-VCH Verlag GmbH & Co. KGaA).

[84] D. Strukov and H. Kohlstedt, *Resistive switching phenomena in thin films: Materials, devices, and applications*, MRS Bulletin **37**, 108–114 (2012).

[85] J. Borghetti, G. S. Snider, P. J. Kuekes, J. J. Yang, D. R. Stewart, and R. S. Williams, *'Memristive' switches enable 'stateful' logic operations via material implication*, Nature **464**, 873–876 (2010).

[86] B. Brandenstein-Köth, *Nichtlinearer Magnetotransport und memristive Funktionen von nanoelektronischen Bauteilen*, PhD thesis, Würzburg University, 2010.

[87] L. Chua, *Resistance switching memories are memristors*, Applied Physics A **102**, 765–783 (2011).

[88] I. Valov, E. Linn, S. Tappertzhofen, S. Schmelzer, J. van den Hurk, F. Lentz, and R. Waser, *Nanobatteries in redox-based resistive switches require extension of memristor theory*, Nature Communications **4**, 1771 (2013).

[89] T. Prodromakis, C. Toumazou, and L. Chua, *Two centuries of memristors*, Nature Materials **11**, 478–481 (2012).

[90] E. C. Linn, *Complementary Resistive Switches*, PhD thesis, Aachen, Techn. Hochsch., 2012.

[91] M. Di Ventra, Y. V. Pershin, and L. O. Chua, *Circuit elements*

with memory: memristors, memcapacitors, and meminductors, Proceedings of the IEEE **97**, 1717–1724 (2009).

[92] M. Ignatov, *Anwendung von „Metall-Isolator-Übergangs“-Kontakten für memristive Bauelemente*, master thesis, Christian-Albrechts-Universität zu Kiel, Faculty of Engineering, Chair of Nanoelectronics, 2013.

[93] R. Williams, *How We Found The Missing Memristor*, IEEE Spectrum **45**, 28–35 (2008).

[94] T. D. Dongale, *An Overview of Fourth Fundamental Circuit Element-\'The Memristor\'*, (2013).

[95] S. Vongehr and X. Meng, *The Missing Memristor has Not been Found*, Scientific Reports **5** (2015).

[96] N. D. Mathur, *The fourth circuit element*, Nature **455**, E13–E13 (2008).

[97] P. Meuffels and R. Soni, *Fundamental issues and problems in the realization of memristors*, arXiv preprint arXiv:1207.7319 (2012).

[98] W. R. Hiatt and T. W. Hickmott, *BISTABLE SWITCHING IN NIOBIUM OXIDE DIODES*, Applied Physics Letters **6**, 106–108 (1965).

[99] Forschungszentrum Jülich - News - 47th IFF Spring School - Memristive Phenomena: From Fundamental Physics to Neuromorphic Computing-lecture notes, 2016.

[100] T. Kever, *Resistive switching in Cu: TCNQ thin films*, PhD thesis, Aachen, Techn. Hochsch., 2009.

[101] S. Menzel, *Modeling and simulation of resistive switching devices*, PhD thesis, Aachen, Techn. Hochsch., 2013.

[102] C. Schindler, *Resistive switching in electrochemical metallization memory cells*, PhD thesis, Aachen, Techn. Hochsch., 2009.

[103] R. Waser and M. Aono, *Nanoionics-based resistive switching memories*, Nature materials **6**, 833–840 (2007).

[104] M. Hansen, M. Ziegler, L. Kolberg, R. Soni, S. Dirkmann, T. Mussenbrock, and H. Kohlstedt, *A double barrier memristive device*, Scientific reports **5**, 13753 (2015).

[105] Y. Hirose and H. Hirose, *Polarity-dependent memory switching and behavior of Ag dendrite in Ag-photodoped amorphous As_2S_3 films*, Journal of Applied Physics **47**, 2767–2772 (1976).

[106] D. Ielmini and R. Waser, *Resistive Switching: From Fundamentals of Nanoionic Redox Processes to Memristive Device Applications*, John Wiley & Sons, 2015.

[107] S. Menzel, S. Tappertzhofen, R. Waser, and I. Valov, *Switching kinetics of electrochemical metallization memory cells*, Physical Chemistry Chemical Physics **15**, 6945–6952 (2013).

[108] Y. Yang and W. Lu, *Nanoscale resistive switching devices: mechanisms and modeling*, Nanoscale **5**, 10076 (2013).

[109] N. Himmel geb. Ruppelt, *Josephson Junctions with Ferromagnetic Alloy Interlayer*, PhD thesis, Christian-Albrechts-Universität Kiel, 2015.

[110] K. K. Schuegraf, *Handbook of thin-film deposition processes and techniques: principles, methods, equipment, and applications*, Noyes Data Corporation/Noyes Publications, 1988.

[111] H.-J. Bullinger, *Technology Guide: Principles - Applications - Trends*, Springer Science & Business Media, 2009.

[112] Chattopadhyay, C. K. K, and b. A. N, *Introduction To Nanoscience And Nenotechnology*, PHI Learning Pvt. Ltd., 2009.

[113] T. Pluym, Q. Powell, A. Gurav, T. Ward, T. Kodas, L. Wang, and H. Glicksman, *Solid silver particle production by spray pyrolysis*, Journal of Aerosol Science **24**, 383–392 (1993).

[114] U. Hilleringmann, *Silizium-Halbleitertechnologie*, Vieweg+Teubner Verlag, Wiesbaden, 2004.

[115] M. Quirk and J. Serda, *Semiconductor manufacturing technology*, volume 1, Prentice Hall Upper Saddle River, NJ, 2001.

[116] X. Hiao, *Introduction to semiconductor manufacturing technology*, Prentice Hall, 2000.

[117] E. Larrañeta, R. E. Lutton, A. D. Woolfson, and R. F. Donnelly, *Microneedle arrays as transdermal and intradermal drug delivery systems: Materials science, manufacture and commercial development*, Materials Science and Engineering: R: Reports **104**, 1–32 (2016).

[118] L. Chi, *Nanotechnology: Volume 8: Nanostructured Surfaces*, John Wiley & Sons, 2010.

[119] See https://www.for2093.uni-kiel.de/de for FOR2093.

[120] Y. Aoki, C. Wiemann, V. Feyer, H.-S. Kim, C. M. Schneider, H. Ill-Yoo, and M. Martin, *Bulk mixed ion electron conduction in amorphous gallium oxide causes memristive behaviour*, Nature communications **5** (2014).

[121] D. S. Jeong, B.-k. Cheong, and H. Kohlstedt, *$Pt/Ti/Al_2O_3/Al$ tunnel junctions exhibiting electroforming-free bipolar resistive switching behavior*, Solid-State Electronics **63**, 1–4 (2011).

[122] E. Mikheev, B. D. Hoskins, D. B. Strukov, and S. Stemmer, *Resistive switching and its suppression in Pt/Nb: $SrTiO_3$ junctions*, Nature communications **5** (2014).

[123] A. Sawa, *Resistive switching in transition metal oxides*, Materials today **11**, 28–36 (2008).

[124] M. Fouda, M. Khatib, and A. Radwan, On the mathematical modeling of series and parallel memcapacitors, in *Microelectronics (ICM), 2013 25th International Conference on*, pp 1–4, IEEE, 2013.

[125] F. L. Traversa, Y. V. Pershin, and M. Di Ventra, *Memory models of adaptive behavior*, IEEE transactions on neural networks and learning systems **24**, 1437–1448 (2013).

[126] Y. V. Pershin and M. Di Ventra, *Memristive circuits simulate memcapacitors and meminductors*, Electronics Letters **46**, 517 (2010).

[127] Y. V. Pershin and M. Di Ventra, *Memory effects in complex materials and nanoscale systems*, Advances in Physics **60**, 145–227 (2011).

[128] M. Mahowald and R. Douglas, *A silicon neuron*, Nature **354**, 515–518 (1991).

[129] M. D. Pickett, G. Medeiros-Ribeiro, and R. S. Williams, *A scalable neuristor built with Mott memristors*, Nature Materials **12**, 114–117 (2013).

[130] M. Wahde, *Biologically Inspired Optimization Methods: An Introduction*, WIT Press, 2008.

[131] C. H. Dagli, *Intelligent Engineering Systems Through Artificial Neural Networks*, ASME Press, 2005.

[132] A. Born, A. B. Neuwied, B. Engelhardt, S. Esders, A. Gnoyke, G. Gräbe, W. Kleesattel, and R. Kleinert, *Biologie Oberstufe: Gesamtband, 2. Auflage*, Cornelsen, 2009.

[133] F. Rieke, *Spikes: exploring the neural code*, MIT press, 1999.

[134] E. M. Izhikevich, *Dynamical systems in neuroscience*, MIT press, 2007.

[135] A. L. Hodgkin and A. F. Huxley, *A quantitative description of membrane current and its application to conduction and excitation in nerve*, The Journal of Physiology **117**, 500–544 (1952), (Copyright Wiley-VCH Verlag GmbH & Co. KGaA).

[136] T.-W. Lee, *Network Balance and Its Relevance to Affective Disorders: Dialectic Neuroscience*, Pronoun, 2016.

[137] F. Theunissen and J. P. Miller, *Temporal encoding in nervous systems: a rigorous definition*, Journal of computational neuroscience **2**, 149–162 (1995).

[138] W. Gerstner, W. M. Kistler, R. Naud, and L. Paninski, *Neuronal Dynamics: From Single Neurons to Networks and Models of Cognition*, Copyright Cambridge University Press 2014, 2014.

[139] J. Benda and A. V. Herz, *A universal model for spike-frequency adaptation*, Neural computation **15**, 2523–2564 (2003).

[140] J. Benda and J. Tabak, Spike-Frequency Adaptation, in *Encyclopedia of Computational Neuroscience*, edited by D. Jaeger and R. Jung, pp 2814–2824, Springer New York, New York, NY, 2015.

[141] R. Mausfeld, The Biological Function of Sensory Systems, in *Neurosciences - From Molecule to Behavior: a university textbook*, pp 239–252, Springer Berlin Heidelberg, Berlin, Heidelberg, 2013.

[142] G. Fuhrmann, H. Markram, and M. Tsodyks, *Spike frequency adaptation and neocortical rhythms*, Journal of neurophysiology **88**, 761–770 (2002).

[143] D. Madison and R. Nicoll, *Control of the repetitive discharge of rat CA 1 pyramidal neurones in vitro.*, The Journal of Physiology **354**, 319–331 (1984).

[144] Å. Edman, S. Gestrelius, and W. Grampp, *Analysis of gated membrane currents and mechanisms of firing control in the rapidly adapting lobster stretch receptor neurone.*, The Journal of physiology **384**, 649–669 (1987).

[145] R. Klein, *Donald Olding Hebb*, Scholarpedia **6**, 3719 (2011).

[146] T. Zaehle, S. Rach, and C. S. Herrmann, *Transcranial Alternating Current Stimulation Enhances Individual Alpha Activity in Human EEG*, PLoS ONE **5**, e13766 (2010).

[147] T. Ohno, T. Hasegawa, T. Tsuruoka, K. Terabe, J. K. Gimzewski, and M. Aono, *Short-term plasticity and long-term potentiation mimicked in single inorganic synapses*, Nature Materials **10**, 591–595 (2011).

[148] D. Kuzum, S. Yu, and H.-S. Philip Wong, *Synaptic electronics: materials, devices and applications*, Nanotechnology **24**, 382001 (2013).

[149] A. L. Hodgkin and A. F. Huxley, *Action Potentials Recorded from Inside a Nerve Fibre*, Nature **144**, 710–711 (1939).

[150] R. FitzHugh, *Mathematical models of threshold phenomena in the nerve membrane*, Bulletin of Mathematical Biology **17**, 257–278 (1955).

[151] J. L. Hindmarsh and R. Rose, *A model of neuronal bursting using three coupled first order differential equations*, Proceedings of the royal society of London B: biological sciences **221**, 87–102 (1984).

[152] C. Mead and L. Conway, *Introduction to VLSI systems*, volume 1080, Addison-Wesley Reading, MA, 1980.

[153] E. M. Izhikevich, *Simple model of spiking neurons*, IEEE Transactions on neural networks **14**, 1569–1572 (2003).

[154] W. Gerstner and R. Brette, *Adaptive exponential integrate-and-fire model*, Scholarpedia **4**, 8427 (2009).

[155] Priv.-Doz. Martin Ziegler (Christian-Albrechts-Universität zu Kiel), Vorlesung: Neuromorphic engineering 2 - neural computation, etit 524, 2017.

[156] A. Haras, M. Witko, D. R. Salahub, K. Hermann, and R. Tokarz, *Electronic properties of the VO_2 (011) surface: density functional cluster calculations*, Surface science **491**, 77–87 (2001).

[157] F. J. Morin, *Oxides Which Show a Metal-to-Insulator Transition at the Neel Temperature*, Physical Review Letters **3**, 34–36 (1959).

[158] A. V. Salker, K. Seshan, and H. V. Keer, *Phase transition behaviour of VO_2*, Physica Status Solidi (a) **75**, K37–K40 (1983).

[159] A. Petraru, R. Soni, and H. Kohlstedt, *Voltage controlled biaxial strain in crystals and its effect on the transition temperature*, Applied Physics Letters **105**, 092902 (2014).

[160] T. Driscoll, J. Quinn, M. Di Ventra, D. N. Basov, G. Seo, Y.-W. Lee, H.-T. Kim, and D. R. Smith, *Current oscillations in vanadium dioxide: Evidence for electrically triggered percolation avalanches*, Physical Review B **86** (2012).

[161] S. Guénon, S. Scharinger, S. Wang, J. G. Ramírez, D. Koelle, R. Kleiner, and I. K. Schuller, *Electrical breakdown in a V_2O_3*

device at the insulator-to-metal transition, EPL (Europhysics Letters) **101**, 57003 (2013).

[162] B. Naundorf, F. Wolf, and M. Volgushev, *Unique features of action potential initiation in cortical neurons*, Nature **440**, 1060–1063 (2006).

[163] J. Benda and J. Tabak, *Spike-Frequency Adaptation*, Encyclopedia of Computational Neuroscience , 2814–2824 (2015).

[164] M. D. McDonnell and L. M. Ward, *The benefits of noise in neural systems: bridging theory and experiment*, Nature Reviews Neuroscience **12**, 415–426 (2011).

[165] R. FitzHugh, *Impulses and Physiological States in Theoretical Models of Nerve Membrane*, Biophysical Journal **1**, 445–466 (1961).

[166] J. Nagumo, S. Arimoto, and S. Yoshizawa, *An Active Pulse Transmission Line Simulating Nerve Axon*, Proceedings of the IRE **50**, 2061–2070 (1962).

[167] E. Izhikevich and R. FitzHugh, *FitzHugh-Nagumo model*, Scholarpedia **1**, 1349 (2006).

[168] J.-M. Ginoux and C. Letellier, *Van der Pol and the history of relaxation oscillations: Toward the emergence of a concept*, Chaos: An Interdisciplinary Journal of Nonlinear Science **22**, 023120 (2012).

[169] B. Van der Pol, *LXXXVIII. On "relaxation-oscillations"*, The London, Edinburgh, and Dublin Philosophical Magazine and Journal of Science **2**, 978–992 (1926).

[170] T. Kanamaru, *Van der Pol oscillator*, Scholarpedia **2**, 2202 (2007).

[171] T. L. Floyd, *Electronic devices: conventional current version*, Pearson Prentice Hall, 2008.

[172] J. Ebers, *Four-terminal pnpn transistors*, Proceedings of the IRE **40**, 1361–1364 (1952).

[173] *See https://www.onsemi.com/pub/Collateral/2N6027-D.PDF for ON Semiconductor.*

[174] S. Siegmund, *Adaption in einer neuronalen Schaltung mit einem programmierbaren Unijunction Transistor*, bachelor thesis, Christian-Albrechts-Universität zu Kiel, Faculty of Engineering, Chair of Nanoelectronics, 2016.

[175] S. H. Strogatz, *Sync: How Order Emerges from Chaos In the Universe, Nature, and Daily Life*, Hachette Books, 2012.

[176] A. Pikovsky, M. Rosenblum, and J. Kurths, *Synchronization: A Universal Concept in Nonlinear Sciences*, Cambridge University Press, 2001), (Copyright A. Pikovsky, M. Rosenblum and J. Kurths 2001, published by Cambridge University Press.

[177] S. H. Strogatz, *Exploring complex networks*, Nature **410**, 268–276 (2001).

[178] A. Adamatzky and L. Chua, *Memristor Networks*, Springer Science & Business Media, 2013.

[179] C. Du, W. Ma, T. Chang, P. Sheridan, and W. D. Lu, *Biorealistic Implementation of Synaptic Functions with Oxide Memristors through Internal Ionic Dynamics*, Advanced Functional Materials **25**, 4290–4299 (2015).

[180] A. Gushchin, E. Mallada, and A. Tang, Synchronization of phase-coupled oscillators with plastic coupling strength, in *Information Theory and Applications Workshop (ITA), 2015*, pp 291–300, IEEE, 2015.

[181] Q. Hu, W. Liu, H. Yang, J. Xiao, and X. Qian, *Experimental study on synchronization of three coupled mechanical metronomes*, European Journal of Physics **34**, 291–302 (2013).

[182] G. Buzsáki, *Neural Syntax: Cell Assemblies, Synapsembles, and Readers*, Neuron **68**, 362–385 (2010).

[183] E. Tognoli and J. A. S. Kelso, *The Metastable Brain*, Neuron **81**, 35–48 (2014).

[184] J. Cannon, M. M. McCarthy, S. Lee, J. Lee, C. Börgers, M. A. Whittington, and N. Kopell, *Neurosystems: brain rhythms and*

cognitive processing, European Journal of Neuroscience **39**, 705–719 (2014).

[185] A. Treisman, *The binding problem*, Current Opinion in Neurobiology **6**, 171–178 (1996).

[186] S. H. Strogatz et al., *Coupled oscillators and biological synchronization*, Scientific American **269**, 102–109 (1993).

[187] B. Van Der Pol and J. Van Der Mark, *Frequency Demultiplication*, Nature **120**, 363–364 (1927).

[188] B. Van Der Pol, *Vii. forced oscillations in a circuit with non-linear resistance.(reception with reactive triode)*, The London, Edinburgh, and Dublin Philosophical Magazine and Journal of Science **3**, 65–80 (1927).

[189] D. Postnov, S. K. Han, and H. Kook, *Synchronization of diffusively coupled oscillators near the homoclinic bifurcation*, Physical Review E **60**, 2799–2807 (1999).

[190] U. Tietze and C. Schenk, *Halbleiter-Schaltungstechnik:[neuer Teil: Nachrichtentechnische Schaltungen]*, Springer, 2002.

[191] J. Fell and N. Axmacher, *The role of phase synchronization in memory processes*, Nature reviews neuroscience **12**, 105–118 (2011).

[192] G. Buzsáki and A. Draguhn, *Neuronal oscillations in cortical networks*, Science **304**, 1926–1929 (2004).

[193] C. M. Gray, P. König, A. K. Engel, and W. Singer, *Oscillatory responses in cat visual cortex exhibit inter-columnar synchronization which reflects global stimulus properties*, Nature **338**, 334–337 (1989).

[194] R. Eckhorn, R. Bauer, W. Jordan, M. Brosch, W. Kruse, M. Munk, and H. J. Reitboeck, *Coherent oscillations: A mechanism of feature linking in the visual cortex?: Multiple electrode and correlation analyses in the cat*, Biological Cybernetics **60**, 121–130 (1988).

[195] F. J. Varela, *Resonant cell assemblies: a new approach to cognitive*

functions and neuronal synchrony., Biological research **28**, 81–95 (1995).

[196] R. N. Shepard, *Mind sights: Original visual illusions, ambiguities, and other anomalies, with a commentary on the play of mind in perception and art*, volume x, W H Freeman/Times Books/ Henry Holt & Co, New York, NY, US, 1990.

[197] B. Hasz and P. Miller, *Storing Autoassociative Memories through Gamma-Frequency Binding between Cell Assemblies of Neural Oscillators*, PhD thesis, Brandeis University, The Faculty of the School of Arts and Sciences.

[198] S. Dirkmann and T. Mussenbrock, *Resistive switching in memristive electrochemical metallization devices*, AIP Advances **7**, 065006 (2017).

[199] S. Dirkmann, M. Ziegler, M. Hansen, H. Kohlstedt, J. Trieschmann, and T. Mussenbrock, *Kinetic simulation of filament growth dynamics in memristive electrochemical metallization devices*, Journal of Applied Physics **118**, 214501 (2015).

[200] M. Hu, Y. Wang, Q. Qiu, Y. Chen, and H. Li, The stochastic modeling of TiO2 memristor and its usage in neuromorphic system design, pp 831–836, IEEE, 2014.

[201] R. Naous, M. Al-Shedivat, and K. N. Salama, *Stochasticity Modeling in Memristors*, IEEE Transactions on Nanotechnology **15**, 15–28 (2016).

[202] P. Knag, W. Lu, and Z. Zhang, *A Native Stochastic Computing Architecture Enabled by Memristors*, IEEE Transactions on Nanotechnology **13**, 283–293 (2014).

[203] E. R. Kandel et al., *Principles of neural science*, volume 4, McGraw-hill New York, 2000.